

Biophysical and Pharmaceutical Applications of CW EPR Spectroscopy under Ultraviolet and Visible Light Irradiation

DISSERTATION

Zur Erlangung des Doktorgrades der Naturwissenschaften
(Dr. rer. nat.)

der

Naturwissenschaftlichen Fakultät II
Chemie, Physik und Mathematik

der Martin-Luther-Universität
Halle-Wittenberg

vorgelegt von

Herrn Florian Lehmann

Gutachter:

Prof. Dr. D. Hinderberger

Prof. Dr. J. Eisermann

Prof. Dr. D. Kurzbach

Tag der Verteidigung: 24. Oktober 2024

"The Inner Machinations Of My Mind Are An Enigma."
- Patrick Star

Contents

Acronyms and abbreviations	I
Symbols	IV
1 Introduction	1
2 The Synergy of Electrons and Radiation	5
2.1 The electron spin and magnetic moment	5
2.2 Electron paramagnetic resonance (EPR) spectroscopy	5
2.3 Photophysical processes of excited molecules	8
2.4 Intermolecular energy transfer	10
3 The LED-coupled EPR Spectrometer Setup	13
3.1 General setup of a continuous wave EPR spectrometer	13
3.2 Fiber-coupled LED irradiation within a MS5000 benchtop EPR spectrometer	14
3.3 Data processing and EPR spectra simulation	17
3.3.1 Baseline correction and calculation of the double integral	17
3.3.2 EPR spectra simulations with <i>EasySpin</i>	20
4 The Photodegradation in Monoclonal Antibody Solutions	21
4.1 Introduction	21
4.2 Basics	22
4.2.1 Structure and function of monoclonal antibodies	22
4.2.2 The photodegradation mechanism	23
4.3 Materials and methods	24
4.3.1 Chemicals	24
4.3.2 EPR spectroscopy	24
4.3.3 Polychromatic irradiation setup	25
4.3.4 UV/Vis absorption spectroscopy	25
4.3.5 Emission spectroscopy	25
4.4 Results and discussion	26
4.4.1 Absorption and fluorescence spectra of mAb solutions	26
4.4.2 Wavelength-dependent decay of TEMPOL in mAb solutions	27
4.4.3 Concentration-dependent decay of TEMPOL in mAb solutions	28
4.4.4 Buffer- and pH-dependent decay of TEMPOL in mAb solutions	31

4.5	Conclusion	32
5	The Photodegradation of Polysorbate	33
5.1	Introduction	33
5.2	Basics	33
5.2.1	Structure of polysorbates and its effect on therapeutic proteins . . .	33
5.2.2	Different grades of polysorbate purity	34
5.3	Materials and methods	35
5.3.1	Chemicals	35
5.3.2	EPR spectroscopy	35
5.4	Results and discussion	35
5.4.1	TEMPOL decay in irradiated polysorbate solutions	35
5.4.2	Selective $^1\text{O}_2$ quenching in irradiated polysorbate solutions	37
5.5	Conclusion	38
6	Bergman Cyclisation of Main-Chain Eneidyne Polymers	41
6.1	Introduction	41
6.2	Basics	42
6.2.1	Bergman cyclisation mechanism	42
6.2.2	Main-chain enediyne polymers	42
6.3	Materials and methods	44
6.3.1	Chemicals	44
6.3.2	EPR spectroscopy	45
6.3.3	Mechanical stress	46
6.4	Results and discussion	46
6.4.1	Radical generation and stability in main-chain enediyne polymers . .	46
6.4.2	Scavenging of TEMPOL radicals in solution	49
6.4.3	Influence of mechanical stress on the Bergman cyclisation	50
6.5	Conclusion	52
7	Investigation of Photoresponsive LCST-Polymers	53
7.1	Introduction	53
7.2	Basics	54
7.2.1	Light-induced <i>E</i> – <i>Z</i> isomerisation of aryl azopyrazole	54
7.2.2	Synthesis of DMAm-AAPEAm _x polymers	54
7.3	Materials and methods	55
7.3.1	Chemicals	55
7.3.2	EPR spectroscopy	56
7.3.3	UV/Vis absorption spectroscopy	57

7.4	Results and discussion	57
7.4.1	Spin probe selection for investigation of hydrophobic interactions . .	57
7.4.2	Light-induced <i>E-Z</i> isomerisation at room temperature	58
7.4.3	Temperature-dependent light-induced <i>E-Z</i> isomerisation	63
7.4.4	Temperature-dependent relaxation after <i>E-Z</i> photoisomerisation . .	67
7.5	Conclusion	68
8	Conclusion	69
9	References	73
10	Appendix	85
10.1	The LED-coupled EPR spectrometer setup	85
10.2	The photodegradation in monoclonal antibody solutions	87
10.3	The photodegradation of polysorbate	102
10.4	Bergman cyclisation of main-chain enediyne polymers	109
10.5	Investigation of photoresponsive LCST-polymers	117
11	Acknowledgements	149
12	Scientific Contributions	151
13	Curriculum Vitae	153
14	Declaration of Authorship	155

Acronyms and abbreviations

16-DSA	16-DOXYL stearic acid
20HP	polysorbate 20 in the 'High Purity' grade
20SR	polysorbate 20 in the 'Super Refined TM ' grade
3-OH-Kyn	3-hydroxykynurenine
5-DSA	5-DOXYL stearic acid
80HP	polysorbate 80 in the 'High Purity' grade
80SR	polysorbate 80 in the 'Super Refined TM ' grade
$^x A$	an akzeptor molecule in the ground state with multiplicity x
$^x A^*$	an akzeptor molecule in the excited state with multiplicity x
a.u.	arbitrary unit
AA	amino acids
AAP	aryl azopyrazole
AAPEAm	ethyl-azopyrazole-acrylamide
AIBN	azobisisobutyronitrile
API	active pharmaceutical ingredient
Asp	aspartic acid
C	circulator
C _H	constant domain of a heavy chain
C _L	constant domain of a light chain
CW	continuous wave
cat	catalyzed
D	detector
$^x D$	a donor molecule in the ground state with multiplicity x
$^x D^*$	a donor molecule in the excited state with multiplicity x
DCM	dichloromethane
DI	double integral
DMAm	dimethyl-acrylamide
DMAm-AAPEAm _x	copolymers of DMAm and AAPEAm with an AAP content of x
DMSO	dimethyl sulfoxide
DNA	deoxyribonucleic acid
DP	degree of polymerization
DSC	differential scanning calorimetry
EA	ethyl acetate
EDY	enediyne
EDY-I	di-tert-butyl octa-4-en-2,6-diyne-1,8-diyl(<i>Z</i>)-dicarbamate
EDY-II	(<i>Z</i>)-octa-4-en-2,6-diyne-1,8-diamine

EDTA	ethylenediaminetetraacetic acid
EPR	electron paramagnetic resonance
Eq.	equation
EZ	electron Zeeman interaction
Fab	antigen binding fragment
Fc	crystallizable fragment
Fig.	figure
FRET	Förster resonance energy transfer
FWHM	full width at half maximum
Glu	glutamic acid
HAT	hydrogen atom transfer
HF	hyperfine interaction
HIC	hydrophobic interaction chromatography
His	histidine
HP	'High Purity' (purity grade of polysorbate)
HPLC	high-performance liquid chromatography
IgG	Immunoglobulin G
IgG1	first subclass of Immunoglobulin G
isc	intersystem crossing
JP	Japanese Pharmacopoeia
Kyn	kynurenine
LED	light-emitting diode
LCST	lower critical solution temperature
LMCT	ligand to metal charge transfer
LA	lock-in amplifier
mAb	monoclonal antibody
Mn-standard	manganese standard
M	modulation source
MW	microwave source
NFK	<i>N</i> -formylkynurenine
NIR	near-infrared
NZ	nuclear Zeeman interaction
PC	computer
PEG	polyethylene glycol
Phr. Eu.	European Pharmacopoeia
ppm	parts per million
PS	power supply
RT	room temperature
S ₀	singlet ground state

S _n	excited singlet state with energy level n>0
SEC	size exclusion chromatography
SOC	spin-orbit coupling
SR	'Super Refined TM ' (purity grade of polysorbate)
T ₀	triplet ground state
T _n	excited triplet state with energy level n>0
Tab.	table
TE	Tris-EDTA (buffer solution)
TEMPO	2,2,6,6-tetramethylpiperidyl-1-oxyl
TEMPOL	4-hydroxy-2,2,6,6-tetramethylpiperidyl-1-oxyl
TEMPOL-benzoate	4-hydroxy-TEMPO-benzoate
THF	tetrahydrofuran
Thr	threonine
TMP	2,2,6,6-tetramethylpiperidine
Trp	tryptophane
USP	United States Pharmacopeia
UV	ultraviolet
UV/Vis	ultraviolet and visible light
V _H	variable domain of a heavy chain
V _L	variable domain of a light chain

Symbols

a	hyperfine splitting constant
A_{iso}	isotropic hyperfine coupling constant
$A(\lambda)$	absorbance (wavelength dependent)
B	magnetic field
B_0	magnetic field, which is swept around with a given sweep width
c	concentration
c_0	speed of light
\mathbf{D}	rotational diffusion tensor
D_{ii}	tensor components of the rotational diffusion tensor \mathbf{D} ($i \in x, y, z$)
e	charge of an electron
E	energy
E_0	redox potential
ΔE	energy gap
g_e	free-electron g-factor
g_{iso}	isotropic g-factor
g_N	nuclear g-factor
h	Planck constant
\hbar	reduced Planck constant
ΔH	enthalpy change
I	intensity
k_{FRET}	rate constant of the Förster resonance energy transfer
k_i	rate constant of a process $i \neq p$
$k_{i \rightarrow f}$	rate constant of a radiationless transition from an initial state (i)
k_p	rate constant of a process p to a final state (f)
K	stability constant
l	pathlength
m_e	mass of an electron
m_N	nuclear spin magnetic quantum number
m_S	spin magnetic quantum number
n_{abs}	number of absorbed photons
n_p	number of photons used for a process p
n_{points}	number of data points
$p_o(x)$	polynomial p of different degree or order o
R	distance
R_0	critical transfer distance
S	spin quantum number
\mathbf{S}	spin angular momentum

t	time
T	temperature
V_{if}	vibronic coupling term between the initial and final state
w_o	coefficients of polynomial with order o
x	azopyrazole content
<hr/>	
γ	gyromagnetic ratio
δ	uncertainty
$\epsilon(\lambda)$	molar absorption coefficient (wavelength dependent)
λ	wavelength
$\lambda_{centroid}$	centroid emission wavelength
λ_{peak}	peak emission wavelength
μ_B	Bohr magneton
μ_N	magnetic dipole moment of a nucleus
μ_S	magnetic dipole moment of an electron
μ_z	z-component of the magnetic dipole moment
ν	frequency
π	circle number 'pi'
π^*	antisymmetric combination of two p-orbitals
ρ_f	density of excited vibrational levels in the final state
τ	time scale
$^1\tau$	lifetime of an excited singlet state
$^3\tau$	lifetime of an excited triplet state
τ_c	rotation correlation time
τ_D^0	lifetime of an excited donor molecule without an acceptor
τ_c	rotation correlation time
Φ	quantum yield
$X(5\text{-DSA}_{\text{bound}})$	proportion of polymer-bound 5-DSA
<hr/>	

1 Introduction

Electron paramagnetic resonance (EPR) spectroscopy, a powerful technique for studying paramagnetic species, relies on the interaction between unpaired electrons and electromagnetic radiation^[1]. By subjecting samples to a magnetic field and irradiating them with microwave radiation, EPR spectroscopy enables the characterization of electron spin states and their environments. This methodology has found applications in diverse fields, including biochemistry^[2,3], catalysis^[4,5] and materials science^[6,7], facilitating the elucidation of molecular structures, reaction mechanisms and electronic properties.

Many reactions, which involve the generation of radicals, can be triggered photochemically^[8–10] like the photo-Fenton reaction^[11,12] or Bergman cyclisation^[13,14]. An efficient investigation of photochemical processes can be performed by extending an EPR spectrometer with a light source. This allows for a simultaneous absorption of UV/vis light and microwave radiation for electronic excitation and utilization of the energy gap between spin states of a paramagnetic species in a magnetic field, respectively.

It is noteworthy, that the systems of interest may not necessarily combine both absorptions within one molecule. Spin probing can be used to investigate a system with no or shortlived paramagnetic species^[16]. Also spin trapping may be utilized to scavenge a photochemically generated radical for EPR spectroscopic observation^[17,18].

The integration of LED irradiation capabilities within the MS5000 Benchtop EPR spectrometer expands the horizons of traditional EPR spectroscopy by offering precise control over the excitation wavelength and intensity. Fiber-coupled LEDs provide a versatile platform for targeted irradiation of samples, allowing to selectively excite specific electronic transitions or induce photochemical reactions. This enhanced functionality opens new avenues for studying photo-induced processes and light-matter interactions in paramagnetic systems with unprecedented precision and flexibility.

The MS5000 Benchtop EPR spectrometer was designed and built by Magnettech (Magnettech GmbH, Berlin, and Freiberg Instruments, Freiberg, Germany). In 2019, Bruker announced the acquisition of the Magnettech EPR business from Freiberg Instruments GmbH^[19]. The device is now labeled as Magnettech ESR5000^[20]. The EPR spectrometer has an opening for the manganese standard (Mn-standard), which is used to determine exact B-field shifts or g-values in an EPR spectrum. This hole can be used to send light into the resonator and irradiate the sample while measuring.

In this thesis, the practical implementation and experimental applications of fiber-

coupled LED irradiation within the MS5000 Benchtop EPR spectrometer are explored. By combining the principles of electron paramagnetic resonance spectroscopy with advanced LED technology, photochemical processes can be triggered inside the device and observed immediately. Chapter 2 gives an introduction to the theory of EPR spectroscopy, photophysical processes and energy transfer of excited molecules. The experimental setup and the procedure for processing EPR spectra are described in chapter 3. This method is applied onto issues in the realm of macromolecular and pharmaceutical photochemistry.

Monoclonal antibodies (mAbs), a very important drug class in human therapeutics^[21–23], suffer from photodegradation under ambient light conditions^[24–26]. Although proteinogenic amino acids are not able to absorb light in the visible region (>400 nm), such photons trigger the degradation process, which indicates the presence of a photosensitizer and energy transfer mechanisms^[23–25,27]. In chapter 4, 4-hydroxy-2,2,6,6-tetramethylpiperidine-1-oxyl (TEMPO) is used as a water-soluble spin probe for quantification of photodegradation in mAb solutions. The advantages of irradiation within the spectrometer and possible photosensitizers are discussed.

In chapter 5, the photodegradation of polysorbate is elaborated on. Surfactants such as polysorbate 20 and polysorbate 80 play a crucial role as excipients in stabilizing an active pharmaceutical ingredient like proteins^[28,29], safeguarding against the development of protein particles and physical damage^[30,31]. Despite the advantages, photodegradation of proteins induced by UV and visible light can be observed in polysorbate containing solutions^[32,33]. Differences between polysorbate 20 and 80 as well as different grades of purity may influence the visible light photodegradation process, which is investigated in this chapter.

Natural antibiotics, such as neocarzinostatin chromophore, calicheamicins, esperamicins and dynemicins, are capable of inducing DNA strand cleavage by the generation of diradicals^[34–37]. The structure of interest is called enediyne (EDY), which is known to undergo a heat- or light-induced Bergman cyclisation. The implementation of EDY groups in a polymer main chain enhances the stability of generated radicals^[38]. Chapter 6 covers main-chain EDY polymers with different backbone structures. The radical generation mechanism and stability is examined and the influence of mechanical stress is discussed.

Azo dyes offer the possibility of *E–Z* photoisomerization, which increases their dipole moment, consequently enhancing their solubility in water. This process is reversible and virtually devoid of side reactions^[39]. Within a polymer matrix^[40,41], such light-responsive systems allow for the manipulation of the phase transition temperature of thermo-responsive polymers. Isothermal switching through irradiation can be applied as an alternative to temperature-induced switching^[39,42]. The light-induced change of the dipole moment within groups attached to a polymer chain may also impact their binding affinity to amphiphilic or hydrophobic molecules. This can be utilized for target-specific and controlled drug delivery, which got increasing attention in recent years^[43–45]. In or-

1 Introduction

der to observe binding behavior of any model compound to a makromolecule via EPR spectroscopy, a paramagnetic group has to be introduced to the system of interest. In chapter 7, the spin-labeled fatty acid 5-DOXYL stearic acid (5-DSA) is utilized to characterize the binding behavior of *cis*- and *trans*-aryl azopyrazole (AAP)-containing polymers. Furthermore, the influence of temperature is investigated.

Overall, this thesis describes a cost-efficient way of combining the MS5000 EPR spectrometer with a fiber-coupled light source and gives examples of its biophysical and pharmaceutical applications. By harnessing the power of light inside the EPR spectrometer, photochemical reactions can be triggered and investigated in an instant.

2 The Synergy of Electrons and Radiation

2.1 The electron spin and magnetic moment

The electron spin is an intrinsic property of the electron. It is often described as clockwise and counterclockwise rotation of the particle around the z-axis. However, the spin rather is of quantum mechanical nature^[46]. An electron has the spin quantum number of $S = 1/2$ and therefore two possible spin states ('spin-up' or α -spin with the symbol \uparrow and 'spin-down' or β -spin with the symbol \downarrow)^[1]. The spin angular momentum \mathbf{S} is a vector in units of \hbar ^[47] and defined as shown in Eq. 2.1.

$$|\mathbf{S}| = \sqrt{S(S+1)} \quad (2.1)$$

Without a magnetic field, two electron spins are degenerate. An applied magnetic field along an arbitrary axis ('z-axis') leads to a precessing of \mathbf{S} around the z-axis in a parallel (α -spin) and antiparallel manner (β -spin). Under these conditions a second (magnetic) quantum number m_S becomes effective (Eq. 2.2)^[46].

$$m_S = -S, -S+1, \dots, S-1, S \quad (2.2)$$

Hence, m_S of an electron can be $+1/2$ and $-1/2$.

The electron as a classical particle possesses a mass m_e and the charge e . The rotation about the z-axis with \mathbf{S} induces a current, which generates a magnetic dipole moment μ_S (Eq. 2.3)^[1].

$$\mu_S = -\gamma \hbar \mathbf{S} = -g_e \frac{e\hbar}{2m_e} \mathbf{S} = -g_e \mu_B \mathbf{S} \quad (2.3)$$

The gyromagnetic ratio (γ) is the ratio of its magnetic moment to its angular momentum. The free-electron g-factor g_e adjusts the classical result of μ_S to the quantum mechanical results^[1]. The constants can be combined into the Bohr magneton μ_B ^[48].

2.2 Electron paramagnetic resonance (EPR) spectroscopy

The energy of interaction between the magnetic dipole moment μ_S and an applied magnetic field B is defined in Eq. 2.4. Since B is aligned along the z-axis, it interacts solely with the

2 The Synergy of Electrons and Radiation

z-component of the magnetic dipole moment μ_z (Eq. 2.5), which relates to the magnetic quantum number m_S (Eq. 2.6). This is referred to as electron Zeeman (EZ) interaction^[49].

$$E = -\mu_S B \quad (2.4)$$

$$E = -\mu_z B \quad (2.5)$$

$$E = g_e \mu_B m_s B \quad (2.6)$$

$$\Delta E = h\nu = E_{m_s=+1/2} - E_{m_s=-1/2} = g_e \mu_B B \quad (2.7)$$

Electron paramagnetic resonance (EPR) spectroscopy utilizes this energy gap, also labeled as 'resonance condition', to investigate molecules with unpaired electrons via absorption of microwave radiation.

Nuclei (index N) also exhibit their own g-factor (g_N), magnetic dipole moment (μ_N) and spin quantum number (m_N), which lead to an expansion of Eq. 2.6 in the presence of the observed electron (Eq. 2.8). The two additional terms are called nuclear Zeeman (NZ)^[50] and hyperfine (HF)^[51,52] interactions (Eq. 2.9).

$$E = g_e \mu_B m_s B \quad - g_N \mu_N m_N B \quad + a m_s m_N \quad (2.8)$$

$$E = \text{EZ} \quad - \text{NZ} \quad + \text{HF} \quad (2.9)$$

HF interactions are the interactions between the electron spin and nuclear spin, which lead to fluctuations of the NZ energy levels. The hyperfine splitting constant a defines the magnitude of these perturbations, which is directly extractable from the distance between peaks in an EPR spectrum (not to be confused with the peak-to-peak linewidth). EZ, NZ and HF interactions are displayed in the energy level diagram shown in Fig. 2.1^[1].

The linewidth and shape of an EPR spectrum can vary significantly and contain structural and dynamic information about the spin system. Stable organic radicals like nitroxides may be used as spin probes to investigate complex systems through the lens of EPR spectroscopy. a is sensitive to the polarity of the environment around the spin probe. Furthermore, the rotational motion, characterized by the rotational correlation time τ_c , highly influences the lineshape of the EPR spectrum. This allows for characterization of the interactions between a spin probe and a makromolecule^[53,54] or elaborate on viscosity of a system of interest^[55,56]. A few nanometers distance between spin probe molecules causes detectable dipole-dipole interactions^[57]. Moreover, high concentrations of other paramagnetic species like oxygen in solution also induce line-broadening^[1].

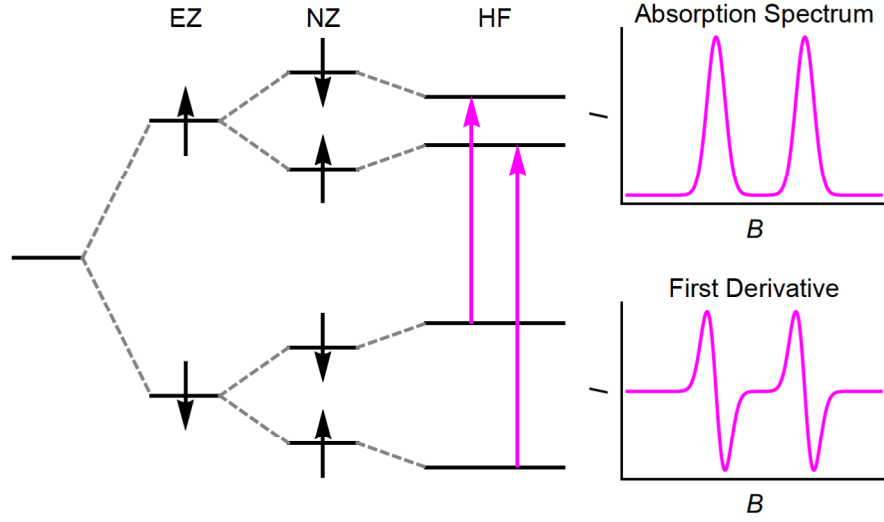


Figure 2.1: Energy level diagram of a spin system with $m_S = m_I = \pm\frac{1}{2}$, $g_N > 0$, $a > 0$ and $g\mu_B B \gg a < g_N\mu_N B$ in a homogeneous magnetic field. The interactions are labeled as EZ (Electron Zeeman), NZ (Nuclear Zeeman) and HF (Hyperfine). The magenta coloured arrows exhibit the two EPR transitions, experimentally observed as microwave absorption (Absorption Spectrum) which is usually shown as the first derivative in an EPR spectrum (First Derivative).

2.3 Photophysical processes of excited molecules

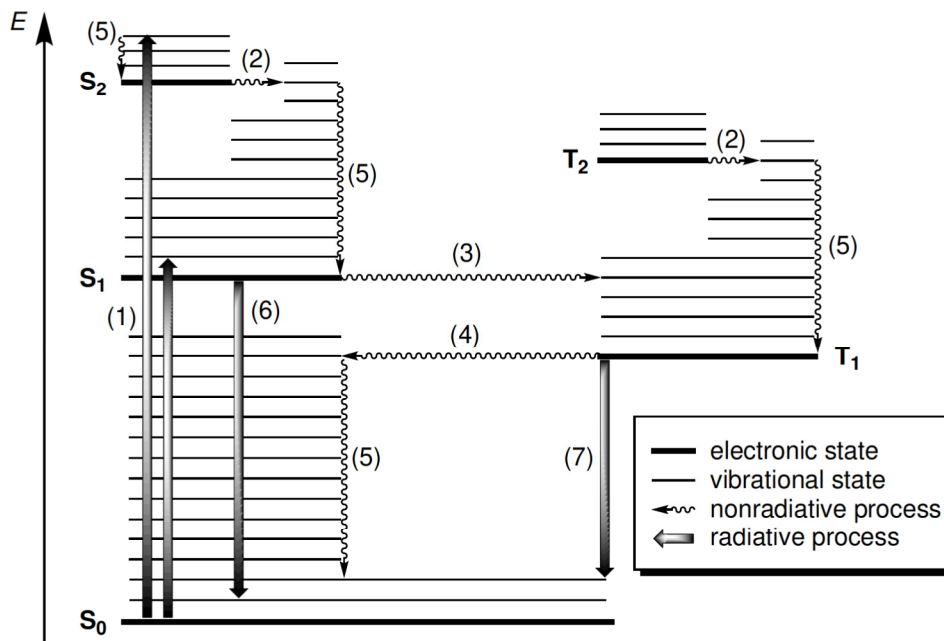


Figure 2.2: The Jablonski diagram displaying singlet states (S_n) and triplet states (T_n) as well as photophysical processes. Thick lines, thin lines, wavy arrows and thick arrows represent electronic states, vibrational states, nonradiative processes and radiative processes, respectively. The numbers in brackets describe the underlying photophysical processes, which are absorption (1), internal conversion (2), intersystem crossing (3 & 4), vibrational relaxation (5), fluorescence (6) and phosphorescence (7)^[15]. The time scale of these processes are listed in Tab. 2.1.

Various electronic energy levels of a molecule and the transition between these levels can be illustrated in a Jablonski diagram (Fig. 2.2), which was developed in the 1930s by the polish physicist Aleksander Jablonski^[58].

Molecular electronic states are depicted by bold horizontal lines aligned vertically to visualize their relative energies, labeled as singlet ground state (S_0), excited singlet states (S_1 , S_2 etc.) or excited triplet states (T_1 , T_2 , etc.). States of the same multiplicity are grouped into distinct columns. Vibrational states are represented by thin lines.

Photophysical processes encompass radiative or non-radiative transitions wherein molecules transition from one electronic state to another without inducing structural alterations, although bond lengths and angles typically exhibit slight variations across different electronic states^[59]. Radiative transitions involve the absorption or emission of photons and are represented by straight thick arrows, while non-radiative transitions, not linked to photon absorption or emission, are depicted by wavy arrows.

The excitation of a molecule is initiated by absorption of radiation (1). A photon can be absorbed when its energy ($E = h\nu$) matches the energy gap (ΔE) between the ground

2 The Synergy of Electrons and Radiation

state and the excited state of the absorbing molecule (Eq. 2.10)

$$\Delta E = h\nu \quad (2.10)$$

The Lambert-Beer law describes the absorbance $A(\lambda)$ of a molecule (Eq. 2.11) with molar absorption coefficient $\epsilon(\lambda)$ of the molecule at a given concentration c and the pathlength l , which is the distance the light has to travel through the sample^[60].

$$A(\lambda) = \epsilon(\lambda)cl \quad (2.11)$$

The time scale of the interaction between a photon and a molecule defined by the Heisenberg uncertainty principle (Eq. 2.12)^[61]. It is dependent on the energy of the photon or else the wavelength of light λ with the speed of light c_0 (Eq. 2.13). Therefore, the time scale of absorption can be estimated to approx. 10^{-15} s.

$$\delta E \delta t \geq \frac{\hbar}{2} = \frac{h}{4\pi} \quad (2.12)$$

$$\delta t \geq \frac{\lambda}{4\pi c_0} \quad (2.13)$$

Absorption in the UV/vis range of light always leads to an electronic excitation (+ vibrational excitation). The transitions between vibrational states within the same electronic states is usually observed upon absorption of near-infrared (NIR) light^[62].

In consequence of an electronic and vibrational excitation, radiationless transitions come into play. Internal conversion (2) and intersystem crossing (isc, 3&4) are the designation of irreversible isoenergetic radiationless transitions between two electronic states of the same multiplicity and different multiplicity, respectively^[15]. Within one electronic state, vibrational relaxation (5) can occur, which describes the loss of vibrational energy through collision with molecules of the surrounding medium. The rate constant governing a radiationless transition from an initial state to a final state, denoted as $k_{i \rightarrow f}$, is defined by Fermi's golden rule (Eq. 2.14)^[15].

$$k_{i \rightarrow f} = \frac{2\pi}{\hbar} V_{if}^2 \rho_f \quad (2.14)$$

The density of excited vibrational levels in the final state ρ_f has to match the energy of the initial state and the square of the vibronic coupling term V_{if} between the initial and final state. Within that term lies the coupling of nuclear and electronic motion, to promote internal conversion, as well as the coupling of the electron spin with the orbital angular momentum (spin-orbit coupling, SOC) to facilitate intersystem crossing regardless of its spin-forbiddenness^[63]. According to El Sayed's rule, isc has to involve a change in orbital type like $^1n, \pi^* \rightarrow ^3\pi, \pi^*$ or $^1\pi, \pi^* \rightarrow ^3n, \pi^*$ transitions^[64].

Spontaneous emission of radiation by an excited molecule is called fluorescence (6) or

phosphorescence (7) when the spin multiplicity is maintained or changed, respectively. Similar to the radiationless transitions, phosphorescence is spin-forbidden and therefore slower than fluorescence. An overview over the discussed photophysical processes and the corresponding time scale is given in Tab. 2.1.

Table 2.1: The time scale ($\tau=1/k_p$) of the photophysical processes depicted in the Jablonski diagram (Fig. 2.2)^[15].

process	name	τ/s
(1)	absorption	10^{-15}
(2)	internal conversion	10^{-12} - 10^{-6}
(3)	intersystem crossing (S→T)	10^{-12} - 10^{-6}
(4)	intersystem crossing (T→S)	10^{-9} - 10^1
(5)	vibrational relaxation	10^{-13} - 10^{-12}
(6)	fluorescence	10^{-9} - 10^{-7}
(7)	phosphorescence	10^{-6} - 10^{-3}

The rate coefficients of these processes are necessary to quantify the quantum yield Φ of a photophysical or photochemical process p (Eq. 2.15).

$$\Phi_p = \frac{n_p}{n_{abs}} = \frac{k_p}{\sum k_i} \quad (2.15)$$

The amount of an observed process n_p is divided by the number of absorbed photons n_{abs} . This ratio is defined by the rate constant of the process of interest k_p divided by the sum of rate constants of all competing processes k_i . These include photophysical and photochemical processes as well as quenching. Primary photochemical processes are those triggered from an electronically excited state, resulting in the formation of a primary photoproduct distinct from the initial reactant^[15].

2.4 Intermolecular energy transfer

Besides intramolecular photophysical deactivation, an excited molecule may serve as a Donor (D^*) in an isoenergetic energy transfer. In doing so, energy of D^* will be transferred to a nearby acceptor molecule (A). Consequently, A is being excited (A^*) without direct absorption of light (Eq. 2.16).



A condition for such an energy transfer is the spectral overlap between the emission spectrum of D^* and the absorption spectrum of A .

From a quantum mechanical viewpoint, Fermi's golden rule (Eq. 2.14) also lays the foundation for a nonradiative energy transfer. Here, V_{if} has to include another dipole.

2 The Synergy of Electrons and Radiation

The interaction of two point-dipoles decreases with the third power of distance and is proportional to V_{if}^2 , therefore the rate constant is impacted by the distance R between D^* and A to the power of six as depicted in Eq. 2.17^[65]. This process is known as Förster resonance energy transfer (FRET)^[66].

$$k_{FRET} = \frac{R_0^6}{(R^6 \tau_D^0)} \quad (2.17)$$

τ_D^0 and R_0 are the lifetime of D^* without A and the critical transfer distance, respectively. Due to the relatively long lifetime of the excited triplet state T_1 , the spin-forbidden triplet-singlet transition is possible (Eq. 2.18)^[15].



During a triplet-triplet energy transfer (Eq. 2.19), the total spin within the transfer system is maintained, therefore it is spin-allowed. However, the oscillator strength for the absorption $^1A \rightarrow ^3A^*$ is very small. Therefore, this transition is unlikely within the FRET mechanism. The oscillatory strength is directly related to the magnitude of the transition dipole moment between the initial and final electronic states involved in the transition^[67]. The transition dipole moment describes the extent to which the electronic charge distribution changes during the transition^[64]. The larger the transition dipole moment, the greater the oscillatory strength, indicating a higher probability of the transition occurring. The triplet-triplet energy transfer operates via a Dexter mechanism^[68], which involves an molecular orbital and wavefunction overlap of D^* and A to exhibit an electron exchange^[64,67,68]. This defines the critical transfer distance to be the sum of van der Waals radii of D and A ^[15].

The radiationless deactivation of an excited molecule is usually referred to as 'quenching'^[67]. One example for an ubiquitous quencher is molecular oxygen (3O_2). It exists as triplet state in its ground state and has two energetically low-lying excited singlet states. An excited singlet donor $^1D^*$ can produce two singlet oxygen molecules (Eq. 2.20 & 2.21)^[15].



2 The Synergy of Electrons and Radiation

3 The LED-coupled EPR Spectrometer Setup

3.1 General setup of a continuous wave EPR spectrometer

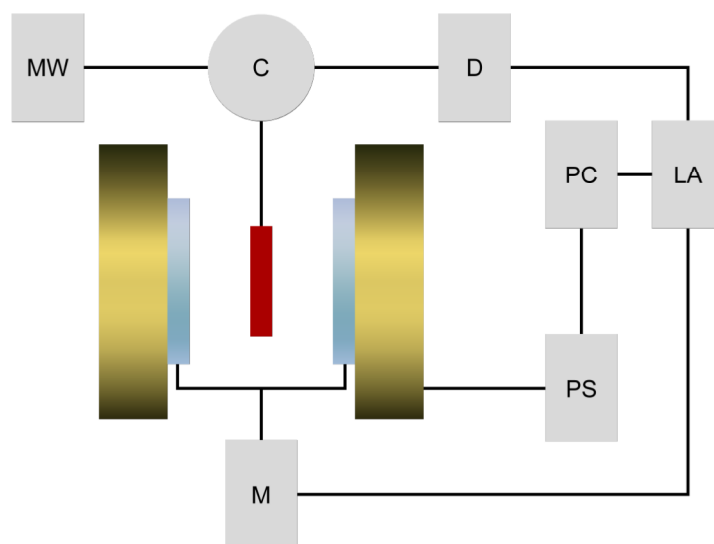


Figure 3.1: Schematic construction of a typical continuous wave (CW) EPR spectrometer. The sample cavity/resonator (red) is placed inside the magnet (brass tones) with modulation coils (aquamarine). The microwave source (MW), circulator (C) and detector (D) are part of the microwave bridge and connected to a lock-in amplifier (LA). The computer (PC) controls the magnet power supply (PS) as well as LA, which is also attached to the modulation source (M).

A general setup of an continuous wave (CW) EPR spectrometer is displayed in Fig. 3.1. The centerpiece of an EPR spectrometer is the electromagnet or superconducting magnet (Fig. 3.1, brass tones). The type and strength of the magnet define the necessary microwave frequency needed to fulfill the resonance condition (Eq. 2.7). A so called X-band or Q-band spectrometer operates at around 9.5 GHz or 34 GHz, respectively^[1,69]. They are able to utilize electromagnets with up to 1.5 T of magnetic flux density^[1]. Higher microwave frequencies require a stronger magnetic field, which can be achieved by superconducting magnets.

The microwave source (MW) may be a magnetron, klystron, Gunn diode or many more^[70]. Its selection depends on the desired power and frequency limit^[71]. MW sends

3 The LED-coupled EPR Spectrometer Setup

the radiation towards the circulator (C), which transmits it to the resonator (Fig. 3.1, red) creating a standing microwave. At the position of the sample, the magnetic field part of the electromagnetic radiation is attempted to be maximized, while the proportion of the electric field should be minimal. The reasons for that are twofold. The electrons absorb the magnetic field part of the electromagnetic radiation and the electric dipole of water in aqueous samples may interact with the electric field part of the microwave, which adversely affects the performance and tuning of the device^[1]. After absorption by the sample, C channels the reflected microwave power to the phase-sensitive detector (D). MW, C and D are implemented in the so called microwave bridge^[1,69].

In addition to the homogeneous magnetic field, a fast oscillating magnetic field modulation (100 kHz) is applied to increase the signal intensity and signal-to-noise (S/N) ratio. This modulation is produced by the modulation coils (Fig. 3.1, aquamarine) and modulation source (M). The detector output also oscillates, which leads to a noise suppression via phase-sensitive detection. This is conducted by the lock-in amplifier (LA)^[72]. The amplitude of the modulation is a parameter, that has to be carefully set by the experimenter. It increases the signal intensity as well as the line-width of an EPR spectrum. These two things have to be balanced carefully for optimal resolution of narrow signal features and their intensity^[1].

For quantitative analysis and comparability between measurements, experimental settings should be identical or the addition of a defined standard may be utilized^[73,74].

3.2 Fiber-coupled LED irradiation within a MS5000 benchtop EPR spectrometer

All CW EPR spectra shown in this work were measured using the Miniscope MS5000 benchtop EPR spectrometer (Magnettech GmbH, Berlin, and Freiberg Instruments, Freiberg, Germany), the MS5000 temperature controller (Magnettech GmbH, Berlin, Germany) and Freiberg Instruments software. The magnetic field shift of an EPR signal depends on the microwave frequency as discussed in the previous chapter on theory of EPR, therefore a manganese standard (Mn-standard) is usually used for calibration. The simultaneous measurement of a sample and the standard is realised by a hole perpendicular to the sample input for insertion of such an Mn-standard into the resonator.

This hole for the insertion of the Mn-standard is utilized as an entrance for light, so EPR spectra can be collected during irradiation of the sample inside the spectrometer. FC5 Multi channel fiber coupled LED light source (Prizmatix Ltd., Cholon, Israel) and a 1 m polymer optical fiber with a diameter of 1.5 mm and a NA of 0.5 was used to send the light through the hole for the Mn-standard into the resonator. The emission spectra of the LEDs used in this work are shown in Fig. 3.3 and technical details of the LEDs are provided in Tab. 3.1.

3 The LED-coupled EPR Spectrometer Setup

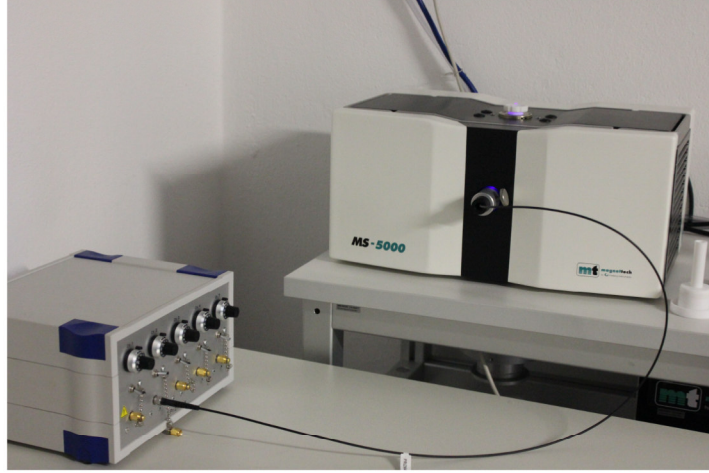


Figure 3.2: Picture of the FC5 Multi channel fiber coupled LED source (left) by Prizmatix and the MS5000 benchtop EPR spectrometer (right) by Freiberg Instruments. On the front of the FC5 Multi channel fiber coupled LED source, there are five LEDs covered with brass caps. Above each LED there is a power switch and a knob to set the desired output power. The polymer fiber cable is mounted on the second LED and leads the light through the hole for the Mn-standard into the resonator of the MS5000 benchtop EPR spectrometer. Three of five LEDs were used in this work. Technical details are shown in Tab. 3.1. The cross section of the MS5000 benchtop EPR spectrometer with the inset for the fiber-coupled irradiation is depicted in Fig. 3.5.

Table 3.1: Technical details of LEDs used in this work. λ_{peak} is the peak emission wavelength of the LED. $\lambda_{centroid}$ is the centroid emission wavelength of the LED. The emission spectra are shown in Fig. 3.3. Further details can be found in the final product test report (Fig. 10.1-10.2).

LED name	output power	λ_{peak}	$\lambda_{centroid}$	FWHM
365A (UV LED)	185 mW	367.92 nm	370.74 nm	12.23 nm
420Z (blue LED)	215 mW	419.80 nm	421.11 nm	14.74 nm
535TR (green LED)	220 mW	540.06 nm	538.70 nm	92.04 nm

The technical workshop of the Martin-Luther-University Halle-Wittenberg produced a cylindrical inset in the shape of the Mn-standard-holder. A photograph of the original Mn-standard-holder and the similar inset for the optical cable is depicted in Fig. 3.4. This inset keeps the polymer fiber as near as possible and tight at the resonator as shown in Fig. 3.5. The distance between the center of the sample within the resonator (Fig. 3.5, red ellipsis) and the light output of the polymer fiber measures 36.8 mm.

The sample tube of liquid samples is placed in a bigger sample holder tube within the MS5000. This is surrounded by another glass tube of the temperature unit, which is drawn in Fig. 3.5 (big vertical cylinder surrounding the red ellipsis). So there are three layers of glass between the light source and the sample. According to Fresnel's equation^[75], the intensity of light will be reduced by approximately four percent per glass layer due to reflections (refractive index of 1.5). Consequently, the intensity of light is reduced by

3 The LED-coupled EPR Spectrometer Setup

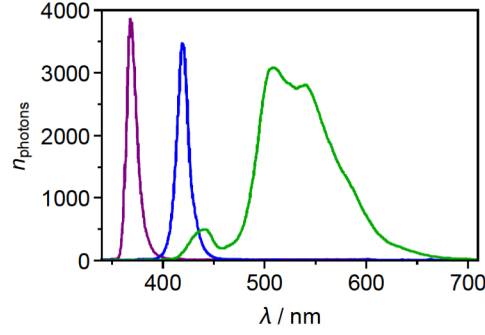


Figure 3.3: Emission spectra of the UV (purple), blue (blue) and green (green) LED used in this work. Data was extracted from the final product test report (Fig. 10.1-10.2). Further technical details are displayed in table 3.1.

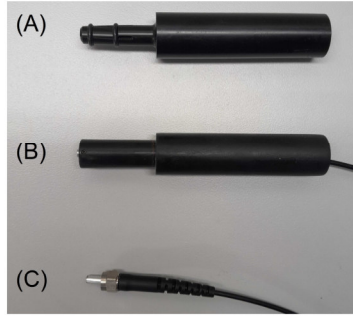


Figure 3.4: (A): The inset for the manganese standard (Magnettech GmbH, Berlin, and Freiberg Instruments, Freiberg, Germany). (B): The inset for irradiation, made at Martin-Luther-University Halle-Wittenberg, connected to the light-conducting polymer fiber cable (Prizmatix Ltd., Cholon, Israel). (C) The light-conducting polymer fiber cable (Prizmatix Ltd., Cholon, Israel).

approximately 12.5 % when it reaches the liquid sample. Solid samples are stored in a bigger sample tube, which is inserted in the resonator without the sample holder tube. This reduces the air-glass surfaces from three to two. Therefore, the total loss of intensity because of reflection is limited to approximately 7.9 %.

Different tube sizes and reflections inside the resonator make it impossible to determine the exact photon flux density inside the sample volume, hence the application is limited to relative comparisons between series of measurements inside this device. The following chapters provide a broad overview of application examples and their interpretations.

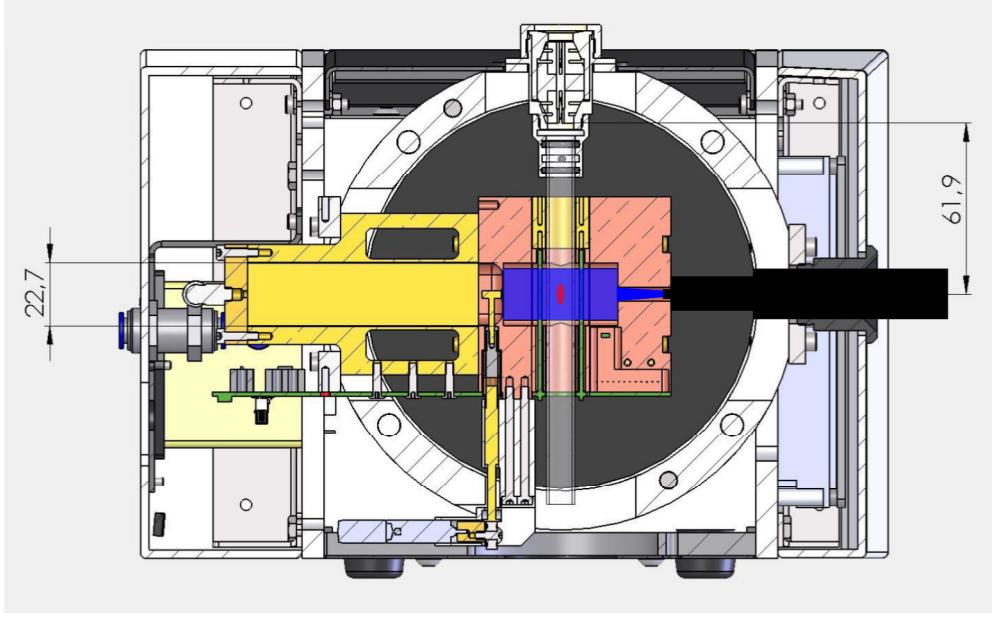


Figure 3.5: Schematic cross section of the MS5000 benchtop EPR spectrometer with the inset for the fiber-coupled irradiation (black). The blue light irradiates the resonator through the hole for the manganese standard. The sample will be placed inside the resonator (indicated by the red ellipsis) with a distance of 36.8 mm from the light source. The original picture was taken from the MS5000 handbook (chapter 4.3.3. 'Height Adjustment').

3.3 Data processing and EPR spectra simulation

3.3.1 Baseline correction and calculation of the double integral

The double integral (DI) is a measure of spin concentration inside the sample solution^[1,74]. In the following chapters, the decay of nitroxide radicals like TEMPOL are discussed. Therefore, the calculation of the DI and the importance of baseline correction is explained in this section.

The gray dashed lines in Fig. 3.6 encompass the signal of TEMPOL. Within this area the signal can be integrated (once from microwave absorption spectrum, twice from EPR spectrum) to calculate the DI after the data points around were used to generate a polynomial regression for baseline correction. Polynomials p of different degree or order o with coefficients w can be suitable for this purpose (eq. 3.1).

$$p_o(x) = w_o x^o + w_{o-1} x^{o-1} + \dots + w_2 x^2 + w_1 x + w_0 \quad (3.1)$$

3 The LED-coupled EPR Spectrometer Setup

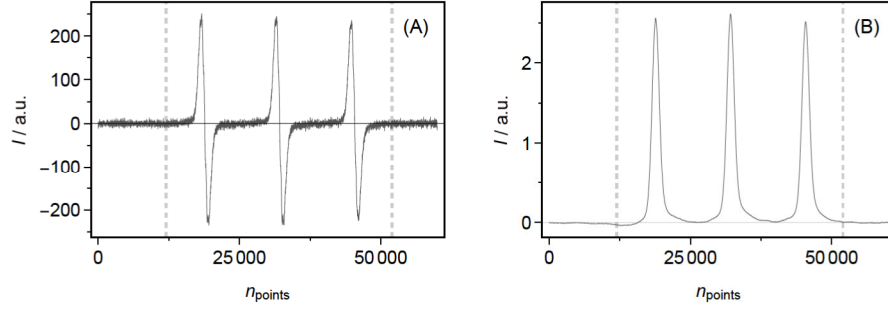


Figure 3.6: EPR signal (A) and microwave absorption signal/integrated EPR signal (B) of 50 μM TEMPOL plotted as list of data points. The signal is located between 12000 and 52000 (gray dashed lines). The data points outside of the signal area are used for polynomial regression and baseline correction.

The challenge with calculation of the DI derives from small offsets within the baseline of the EPR spectrum. Therefore, a highly accurate baseline correction is necessary. Slight deviations may induce a huge error upon integration as shown in Fig. 3.7.

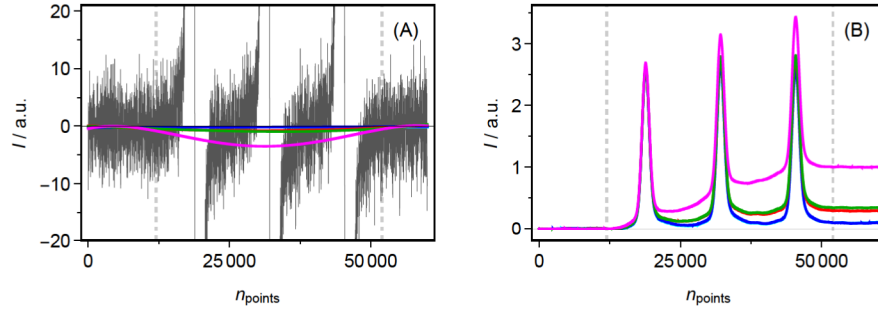


Figure 3.7: (A): EPR signal of 50 μM TEMPOL plotted as list of data points and zoomed onto the baseline. polynomial fits of zero (cyan), first (blue), second (red), third (green) and fourth (magenta) order are calculated with data points from zero to 12000 and from 52000 to 60000 (gray dashed lines). (B): Microwave absorption spectra calculated by integrating the EPR signal (A) after subtracting the polynomial fits of zero (cyan), first (blue), second (red), third (green) and fourth (magenta) order.

Another approach is the baseline correction after the first integration as depicted in Fig. 3.8, but this also is not accurate enough for comparing very small changes in DI during a slow photodegradation process.

3 The LED-coupled EPR Spectrometer Setup

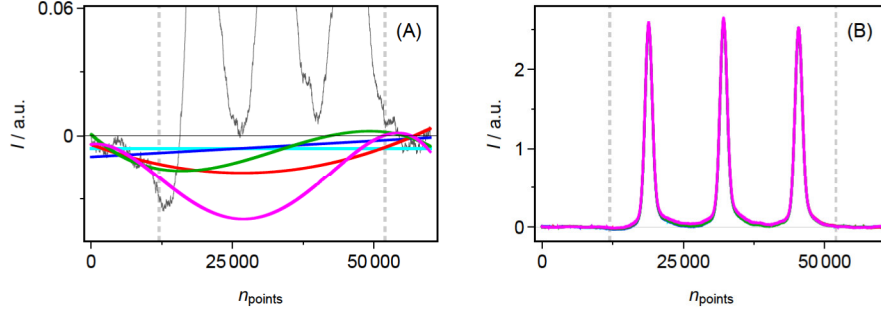


Figure 3.8: (A): Microwave absorption signal of 50 μM TEMPOL calculated by integration of the EPR signal (Fig. 3.6 (A)), plotted as list of data points and zoomed onto the baseline. Polynomial fits of zero (cyan), first (blue), second (red), third (green) and fourth (magenta) order are calculated with data points from zero to 12000 and from 52000 to 60000 (gray dashed lines). (B): Microwave absorption after subtracting the polynomial fits of zero (cyan), first (blue), second (red), third (green) and fourth (magenta) order shown in (A).

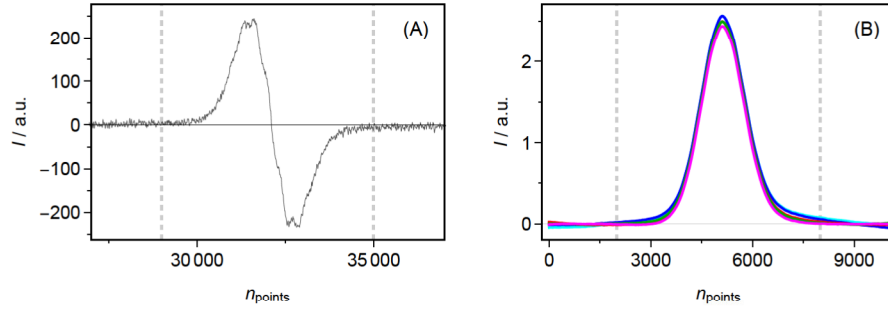


Figure 3.9: EPR signal of 50 μM TEMPOL plotted as list of data points and zoomed onto the center field peak. These 10000 data points are extracted and baseline correction is performed by subtracting the polynomial fits of zero (cyan), first (blue), second (red), third (green) and fourth (magenta) order after integration to get the resulting microwave absorption center field peak.

The real DI is distributed across all three peaks of the EPR signal and also depends on the microwave power^[1,74]. In this thesis, relative DI decays are created by using the same experimental parameters for all spectra within one series of measurement and normalizing on the starting DI. This enables the calculation of the DI by zooming onto the center field peak of the nitroxide signal, since the relative decay of area under the center field peak is equal to the relative decay of the DI of the full spectrum. The great advantage of this method is the minimisation of the baseline influence upon double integration as displayed in Fig. 3.9. The integrated area of the spectrum solely consists of the EPR signal. It is noteworthy, that this approach is only applicable when the motion of the spin probe does not change during a series of measurement. A change in viscosity or binding of the spin probe would induce a change in the shape of the spectrum and subsequently redistribute the DI between the low, center and high field peak.

3.3.2 EPR spectra simulations with *EasySpin*

EasySpin is a Matlab toolbox for advanced simulation of EPR spectra^[76,77]. Slow motion EPR spectra can be simulated with the *EasySpin* function *chili*^[78]. By matching the simulation to the measured spectra it is possible to extract information about binding of a spin probe to a protein or a polymer due to its restricted rotation which strongly influences the shape of the EPR spectrum^[1].

For each *EasySpin* function, it is necessary to define the spin system. Therefore, the electron and nuclear spins need to be specified. Additionally, the isotropic g-factor g_{iso} and the isotropic hyperfine coupling constant A_{iso} as well as the linewidth will be applied to the program. One of the most important parameters for slow motion EPR spectra is the rotational correlation time τ_c usually calculated from the rotational diffusion tensor \mathbf{D} (Eq. 3.2)^[76,78]. The decadal logarithm of the rotational correlation time *logtcorr* is used input for the simulation.

$$\tau_c = \frac{1}{6}(D_{xx} \cdot D_{yy} \cdot D_{zz})^{-\frac{1}{3}} \quad (3.2)$$

As mentioned in the previous section, the experimental settings also have a significant impact on the shape of an EPR spectrum. Consequently, the simulation requires information about the experimental settings like the spectrometer frequency, B_0 -field, the sweep width, number of points and the harmonic of detection^[76].

With this kind of simulation it is possible to determine the percentage of slowly rotating spin probes, which are bound to a macromolecule, and the fast rotating unbound ones^[79,80].

4 The Photodegradation in Monoclonal Antibody Solutions

4.1 Introduction

Monoclonal antibodies (mAbs) are one of the most important drug classes in human therapeutics today^[21–23]. For decades, new mAbs were developed including optimization of formulation and purification processes. After years of extensive research, the issue of photodegradation under ambient light conditions still persists in monoclonal antibody solutions.^[24–26] As visualized in Fig. 4.1, proteinogenic amino acids should not be able to absorb visible light, hence, the literature assumes a photosensitizer absorbing in the visible region >400 nm^[23–25,27].

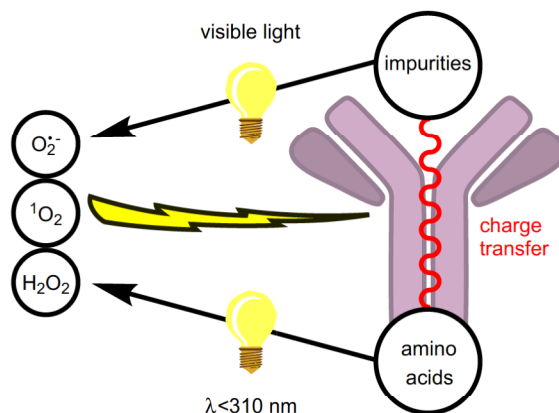


Figure 4.1: Schematic representation of photophysical and photochemical nexuses involved in the photodegradation process of mAbs. The mAb is depicted in purple. Amino acids inside the protein may absorb UV light and form reactive oxygen species, which might cause oxidation and subsequent degradation in mAbs. Furthermore, a photosensitizer (impurities) could absorb light in the visible range and may be bound to the antibody. The excited photosensitizer might also generate reactive oxygen species or modify the protein via charge transfer mechanisms.

In this chapter, three different mAbs (I, II and III) are compared in their absorption and fluorescence properties. Furthermore, 4-hydroxy-2,2,6,6-tetramethylpiperidin-1-oxyl (TEMPO) is used as a water-soluble spin probe for indirect quantification of photodegradation in these mAb solutions via EPR spectroscopy, since reactive oxygen species, alkyl-, peroxy- and hydroperoxy radicals may induce a decrease in EPR activity of TEMPO^[81].

Moreover, the effect of different buffer solutions on the photodegradation of mAb-III was investigated and possible photosensitizers are discussed.

4.2 Basics

4.2.1 Structure and function of monoclonal antibodies

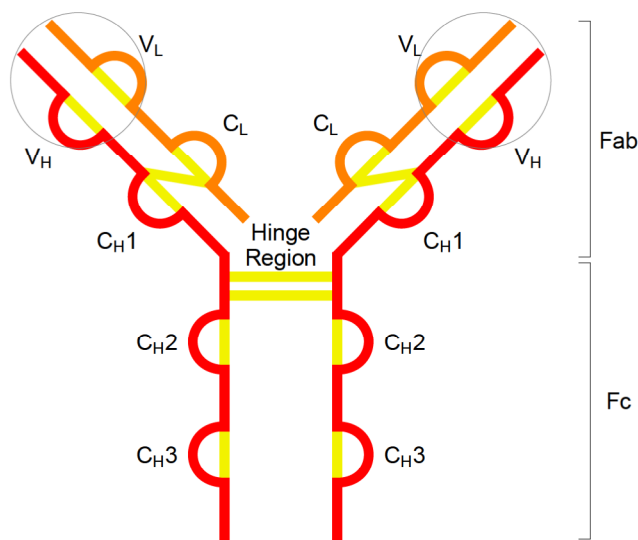


Figure 4.2: Schematic depiction of the general structure of a mAb with heavy chains (red, index 'H') light chains (orange, index 'L'), disulfide bonds (yellow) constant regions ('C'), variable regions ('V'), the hinge region, the crystallizable fragment ('Fc'), the antigen-binding fragment ('Fab') and its antigen-binding sites (gray circles).

A monoclonal antibody (mAb) is a type of antibody that is derived from a single clone of immune cells and is therefore composed of identical immune cells, all of which target the same antigen. The general structure of a mAb is shown in fig. 4.2^[82].

Monoclonal antibodies typically consist of two identical heavy chains (index 'H'). Each heavy chain is a large polypeptide chain that contains several functional domains. There are also two identical smaller polypeptide chains, called light chains (index 'L'). At the N-terminus of both heavy and light chains, there are regions known as the variable regions, denoted as V_H (variable heavy) and V_L. These regions are highly variable in amino acid sequence and are responsible for antigen recognition. The Fab region is the antigen-binding fragment, and it consists of both the V_H and V_L domains. The C-terminus of the heavy chains contains the constant regions, denoted as C_H (constant heavy) domains. The constant regions determine the antibody's effector functions, such as binding to immune cells or complement proteins. The Fc region is the crystallizable fragment, which interacts with immune system components and plays a crucial role in antibody effector functions.

Disulfide bonds connect the heavy and light chains to stabilize the antibody's overall structure. The center of the antibody, located between the Fab and Fc regions, is called hinge region. It allows flexibility and movement, which is important for the antibody to bind to different epitopes on an antigen^[83].

Monoclonal antibodies are designed to be highly specific for a particular antigen, making them valuable tools for diagnostics and therapeutics. The combination of variable and constant regions, along with their effector functions, gives them a diverse range of applications, from targeted cancer therapy to the treatment of autoimmune diseases and infectious diseases^[84,85].

4.2.2 The photodegradation mechanism

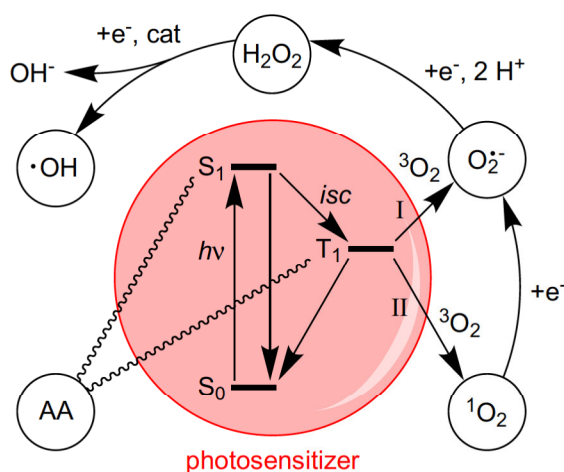


Figure 4.3: Schematic depiction of the physicochemical photodegradation mechanism in proteins: A photosensitizer (red) can be excited via light ($h\nu$), switching from its ground state (S_0) to the excited singlet state (S_1), which can transform to an excited triplet state (T_1) via intersystem crossing (isc). Protein degrading charge-transfers reactions (curvy lines) between excited states (T_1 and S_1) and amino acids (AA) in the antibodies are possible. Moreover, oxygen in the air exists in its triplet ground state (3O_2) and can be converted to a reactive oxygen species like singlet oxygen (1O_2) (type II mechanism) or the superoxide anion radical ($O_2^{\bullet-}$) (type I mechanism), which may be transmuted to hydrogen peroxide (H_2O_2) and consecutively disproportionate into pairs of a hydroxy radical ($\bullet OH$) and a hydroxy ion (OH^-) in a Fenton-reaction-like catalyzed (cat) process^[86].

Proteinogenic amino acids in antibodies do not absorb visible light $>400\text{ nm}$ ^[23–25,27], hence its absorption can only induce the mechanisms of photodegradation when it is based on energy or electron transfer processes from a photosensitizer to amino acids or oxygen molecules in solution (Fig. 4.3). The photosensitizer is excited from the singlet ground state (S_0) to the singlet excited state (S_1) by absorption of a photon. From the S_1 , it may either undergo a radiationless deactivation or a conversion to the triplet state (T_1) via intersystem crossing^[87], which can initiate further reactions.

From T_1 , an energy transfer to molecular triplet oxygen 3O_2 is possible, resulting in the formation of singlet oxygen 1O_2 . In literature, this is referred to as the 'type II' reaction pathway^[23,88]. In aqueous solution, the energy difference between singlet and triplet oxygen amounts to 7918.1 cm^{-1} ^[89]. 1O_2 has a lifetime of approx. 10^{-6} - 10^{-5} s ^[25], which is influenced by the amount of possible quenchers inside the solution. In aqueous media and at room temperature 1O_2 might be able to diffuse distances up to 125 nm ^[90] while $14.5 \times 8.5 \times 4.0 \text{ nm}^3$ being the typical dimensions of an IgG mAb^[91]. The hydrodynamic radius of a mAb is reported to be $5\text{-}6 \text{ nm}$ ^[92]. The distance between mAbs at commercially established concentrations of $50\text{-}150 \text{ mg/ml}$ can be estimated to just a few nanometers, which makes intermolecular diffusion of 1O_2 possible^[92].

In the so called 'type I' reaction pathway, superoxide anion radicals ($O_2^{\bullet-}$) are generated via electron transfer processes from an excited photosensitizer to 3O_2 ^[23,88]. By uptake of an additional electron, such radical anions may be transmuted to highly reactive hydrogen peroxide molecules (redox potential $E_0(O_2^{\bullet-}/H_2O_2) = 0.89 \text{ V}$ and $E_0(H_2O/H_2O_2) = 1.78 \text{ V}$, $\text{pH} = 7$)^[93,94] which could subsequently disproportionate into pairs of a hydroxy radical (redox potential $E_0(H_2O_2/\bullet OH) = 0.38 \text{ V}$ and $E_0(H_2O/\bullet OH) = 2.32 \text{ V}$, $\text{pH} = 7$)^[93] and a hydroxy ion in a Fenton-reaction-like catalyzed process^[86].

The photodegradation process induced by visible light might also be possible in the absence of oxygen^[95]. Energy could also be transferred from a photosensitizer directly to the mAbs' amino acids^[96]. A Förster resonance energy transfer (FRET) may be possible over a distance of up to 10 nm via dipolar coupling of a photosensitizer (donor) with an acceptor^[97]. Theoretically, energy transfer from S_1 is possible but less likely than triplet-triplet energy transfer because the lifetime of T_1 (e.g. riboflavin in water: $^3\tau \approx 13 - 120 \mu\text{s}$)^[98] is usually much higher than the lifetime of S_1 (e.g. riboflavin in water: $^1\tau \approx 5 \text{ ns}$)^[99,100]. This is due to the spin-forbidden transition from T_1 to S_0 ^[87].

4.3 Materials and methods

4.3.1 Chemicals

The mAbs (I, II and III) were provided by Boehringer Ingelheim GmbH & Co.KG (Biberach an der Riß, Germany) as 200 mg/ml stock solution and in the desired buffer solution. 4-Hydroxy-2,2,6,6-tetramethyl-piperidin-1-oxyl (TEMPOL, 97 % purity) was purchased from Sigma-Aldrich Chemie GmbH (Taufkirchen, Germany).

4.3.2 EPR spectroscopy

The monochromatic irradiation setup within the MS5000 EPR spectrometer (Magnettech GmbH, Berlin, and Freiberg Instruments, Freiberg, Germany) is described in section

3.2. Micropipettes (BLAUBRAND® intraMARK, Wertheim, Germany) were filled with about 12 μ L of sample solution containing 50 μ M TEMPOL. The capillary tube sealant (CRITOSEAL® Leica) was used to close the sample tubes. The temperature was set to 25 °C (\pm 0.2 °C). A magnetic field sweep of 8 mT centered around 337.6 mT with a scan time of 60 s, a modulation amplitude of 0.05 mT (100 kHz) and a microwave power of 5 mW were used. Each spectrum is an accumulation of 5 scans. To calculate the double integrals (DI), the EPR spectra were integrated twice after a baseline correction.

4.3.3 Polychromatic irradiation setup

The samples were placed in a self-made LED chamber. This irradiation was performed by Elena Hipper according to Hipper *et al.*^[24]. Measuring EPR spectroscopy and polychromatic irradiation are not coupled as with the monochromatic irradiation setup described in section 3.2. Samples had to be taken separately for each individual measurement.

4.3.4 UV/Vis absorption spectroscopy

The absorption spectra of 50 mg/ml mAb solutions were recorded on a HP/Agilent 8453 UV/Vis Spectrophotometer (Agilent Technologies, Santa Clara, USA). The samples were filled inside a 500 μ l quartz glass cuvette with an optical path length of 10 mm.

4.3.5 Emission spectroscopy

The fluorescence/phosphorescence spectra were recorded with the F'S5 spectrofluorometer (Edinburgh Instruments, Livingston, UK). The measured mAb solutions were put in a 10 mm quartz glass cuvette with a filling volume of 500 μ l. The samples were irradiated at room temperature with a 150 W CW ozone-free xenon lamp. Emitted photons were counted for 1 second in steps of 1 nm. The slit width of the excitation and emission pathway is 2.5 nm and 3 nm respectively.

4.4 Results and discussion

4.4.1 Absorption and fluorescence spectra of mAb solutions

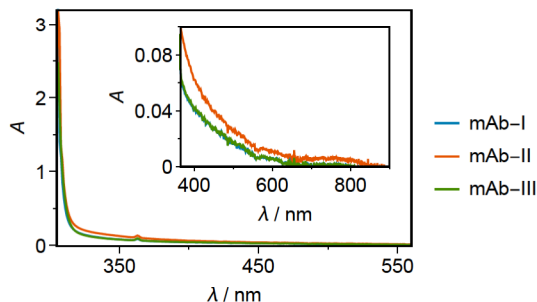


Figure 4.4: UV/Vis spectra of 50 mg/ml mAb-I (blue)/mAb-II (orange)/mAb-III (green). The inset shows the absorption in the visible and NIR range of light.

According to the first law of photochemistry, a photochemical reaction can only be triggered by absorbed photons^[101]. As shown in Fig. 4.4, each of the investigated 50 mg/ml mAb solutions show a small but measurable absorption in the visible range of light from 400 nm to at least 600 nm.

As discussed in chapter 2, a molecule in its excited state may have fluorescent or phosphorescent properties. Therefore, an emission spectrum was recorded for each mAb with an excitation wavelength of 420 nm shown in Fig. 4.5 (A). The maximum fluorescence intensity of all three mAbs is slightly below 500 nm. The excitation experiment can be used to lock the detector onto one emission wavelength and scan through the excitation wavelengths. It is shown in Fig. 4.5 (B). This reveals the wavelengths, which trigger the emission observed at 500 nm.

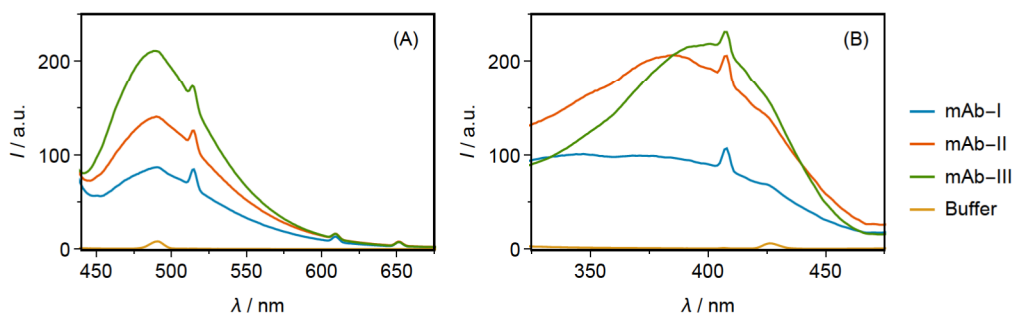


Figure 4.5: Spectra of 50 mg/ml mAb-I (blue)/mAb-II (orange)/mAb-III (green) in phosphate buffer. (A): Emission spectra with an excitation wavelength of 420 nm. (B) Excitation spectra with an emission wavelength of 500 nm.

If this observed emission signal is caused by a photosensitizer, blue light (420 nm) is well suitable for further investigation of photodegradation triggered by visible light. An

excitation wavelength above approx. 450 nm (Fig. 4.5 (B)) triggers almost no emission. Therefore, the photodegradation is expected to be virtually non-existent at higher wavelengths, which is discussed in the following section.

4.4.2 Wavelength-dependent decay of TEMPOL in mAb solutions

EPR spectra of 50 μM TEMPOL in 100 mg/ml mAb-II were irradiated with UV-A (365 nm), blue (420 nm) and green (535 nm) light over a time period of twelve hours. The double integral (DI) of each spectrum was calculated and plotted against the time, as shown in Fig. 4.6. The DI is a measure of the amount of radicals inside the sample. The higher the energy of absorbed photons, the faster is the decay of TEMPOL's nitroxide radical. Therefore, the lower the wavelength of the light source, the more photodegradation occurs inside the mAb solution.

Even during irradiation with light at 535 nm a slow decay of TEMPOL could be observed, although this was not expected at such a high wavelength. However, with a view on the emission spectrum of the green LED, which was used in this experiment (Fig. 3.3), a fraction of blue light is also emitted by this light source, causing the slow photodegradation.

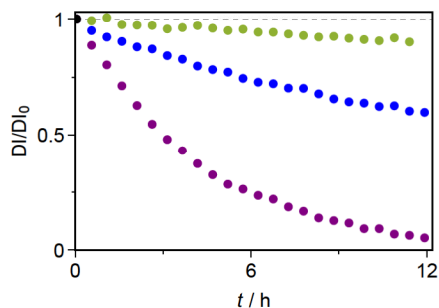


Figure 4.6: The wavelength-dependent decay of TEMPOL in mAb solutions. The normalized DI calculated from EPR spectra of irradiated (365 nm: purple, 420 nm: blue, 535 nm: green) samples containing 50 μM TEMPOL and 100 mg/ml mAb-II are depicted as function of time. Raw spectra are shown in fig. 10.5 - 10.3.

4.4.3 Concentration-dependent decay of TEMPOL in mAb solutions

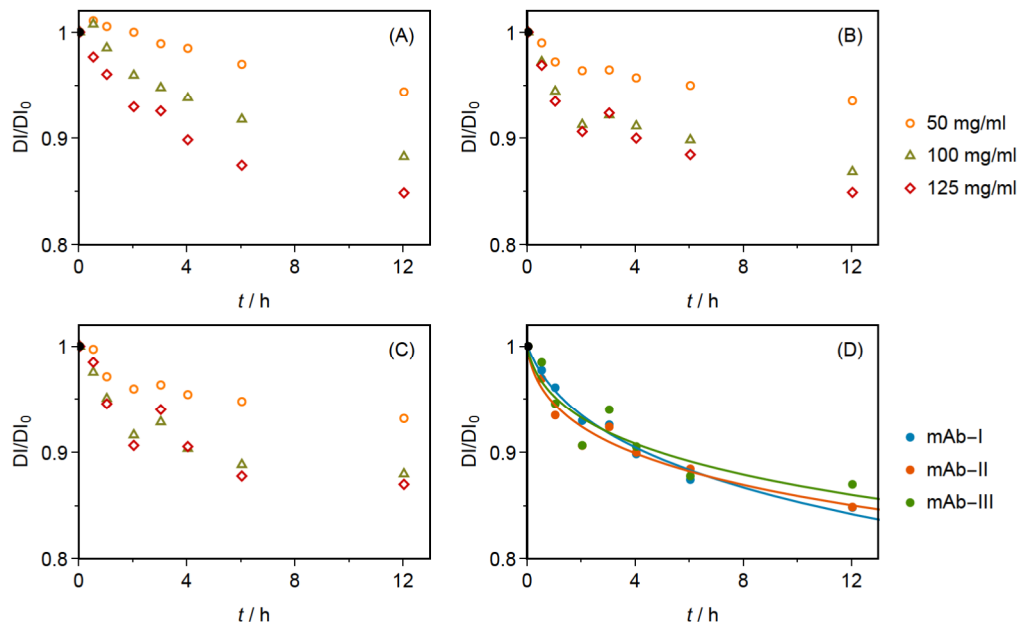


Figure 4.7: The concentration-dependent decay of TEMPOL in mAb solutions. The normalized DI calculated from EPR spectra of polychromatically irradiated samples containing 50 μ M TEMPOL and mAb-I (A)/mAb-II (B)/mAb-III (C) are depicted as function of time. (D): The comparison of the DI decay of 50 μ M TEMPOL with 125 mg/ml of each mAb taken from subfigures (A), (B) and (C). The lines show the best fit of the exponential decay function $f(t) = 1 - e^{a \times t^b}$. The fit parameter are shown in Tab. 4.1. The dark control measurements can be viewed in Fig. 10.6. The raw spectra are shown in Fig. 10.16 - 10.24

Fig. 4.7 shows the decay of 50 μ M TEMPOL during polychromatic irradiation in mAb solutions at different concentrations. This irradiation was performed in a light chamber for comparability with other methods of investigation published by Hipper *et al.* (2022)^[24].

The photodegradation of mAbs was also tested via size exclusion chromatography (SEC), hydrophobic interaction chromatography (HIC) and protein A chromatography. It is dependent on the cumulative light dosage as well as the concentration of mAbs and oxygen^[24]. The concentration dependency of generation of reactive species can be confirmed with the TEMPOL decay experiment (Fig. 4.7). However, the separation of irradiation and EPR measurement is inferior to the fiber-coupled LED irradiation setup inside the MS5000 as shown in Fig. 4.8. There, 50 μ M TEMPOL with 125 mg/ml of mAb-I, mAb-II and mAb-III were irradiated inside the MS5000 with light at 420 nm. Since one sample stays inside the device during the irradiation, an arbitrary amount of spectra can be recorded with small time intervals between DI data points, while in Fig. 4.7 (D), each DI data point had to be separately taken from the irradiated sample inside the light chamber and are therefore limited by its volume. The latter is more practical work for the

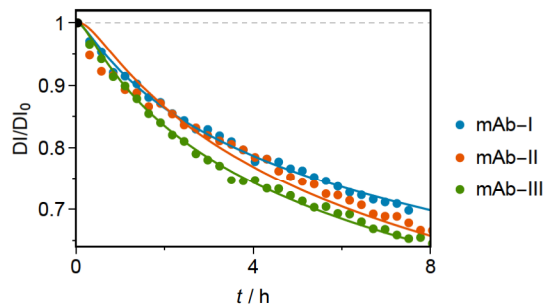


Figure 4.8: The DI decay of 50 μ M TEMPOL with 125 mg/ml of mAb-I (blue)/mAb-II (orange)/mAb-III (green) during monochromatic irradiation (420 nm) inside the MS5000 EPR spectrometer. The lines show the best fit of the exponential decay function $f(t) = 1 - e^{a \times t^b}$. The fit parameter are shown in Tab. 4.2. The dark control measurements can be viewed in fig. 10.25. The raw spectra are shown in fig. 10.29 - 10.31.

Table 4.1: Fit parameter, standard error, t-statistics and P-values of the exponential decay function $f(t) = 1 - e^{a \times t^b}$ used as fitting model in Fig. 4.7.

Antibody	Parameter	Estimate	Standard Error	t-Statistic	P-Value
mAb-I	a	-3.1779	0.081639	-38.9265	1.920×10^{-8}
	b	-0.2182	0.014832	-14.7157	6.186×10^{-6}
mAb-II	a	-2.9016	0.102725	-28.2469	1.302×10^{-7}
	b	-0.1702	0.021288	-7.9954	2.041×10^{-4}
mAb-III	a	-3.0409	0.186067	-16.3432	3.341×10^{-6}
	b	-0.1751	0.036329	-4.8195	2.941×10^{-3}

experimenter and more sensitive to error during sample collection. Both methods were fitted with an exponential decay function $f(t) = 1 - e^{a \times t^b}$. The fit parameters are shown in Tab. 4.1 and Tab. 4.2 for separated irradiation and the irradiation inside the MS5000, respectively. The standard errors, t-statistics and the P-values of the fitted parameter depicted in Tab. 4.2 are much smaller than in Tab. 4.1. This highlights the advantages of the fiber-coupled LED irradiation setup inside the MS5000.

Since mAbs are highly purified, protein-bound photosensitizers may cause the photodegradation in the visible range of light. These might be oxidation products of aromatic amino acids (tryptophane, tyrosine, histidine and phenylalanine) and sulfur-containing amino acids (cysteine and methionine)^[102,103], cation- π interactions with aromatic amino acids^[104–107] or trace levels of iron(III) forming complexes with amino acid side chains in mAbs and therefore extend the absorption band into visible range above 400 nm^[95,108]. A schematic representation of possible protein-bound photosensitizers within a monoclonal antibody is shown in Fig 4.9. In the following section, the influence of different buffer solutions will give further indications of the photosensitizer’s characteristics.

Table 4.2: Fit parameter, standard error, t-statistics and P-values of the exponential decay function $f(t) = 1 - e^{a \times t^b}$ used as fitting model in Fig. 4.8.

Antibody	Parameter	Estimate	Standard Error	t-Statistic	P-Value
mAb-I	a	-2.5673	0.026169	-98.10	5.180×10^{-36}
	b	-0.3665	0.006706	-54.65	3.451×10^{-29}
mAb-II	a	-2.7401	0.076669	-35.73	1.301×10^{-33}
	b	-0.4521	0.014742	-30.66	7.352×10^{-31}
mAb-III	a	-2.3842	0.015978	-149.21	6.635×10^{-80}
	b	-0.4052	0.003121	-129.83	3.141×10^{-76}

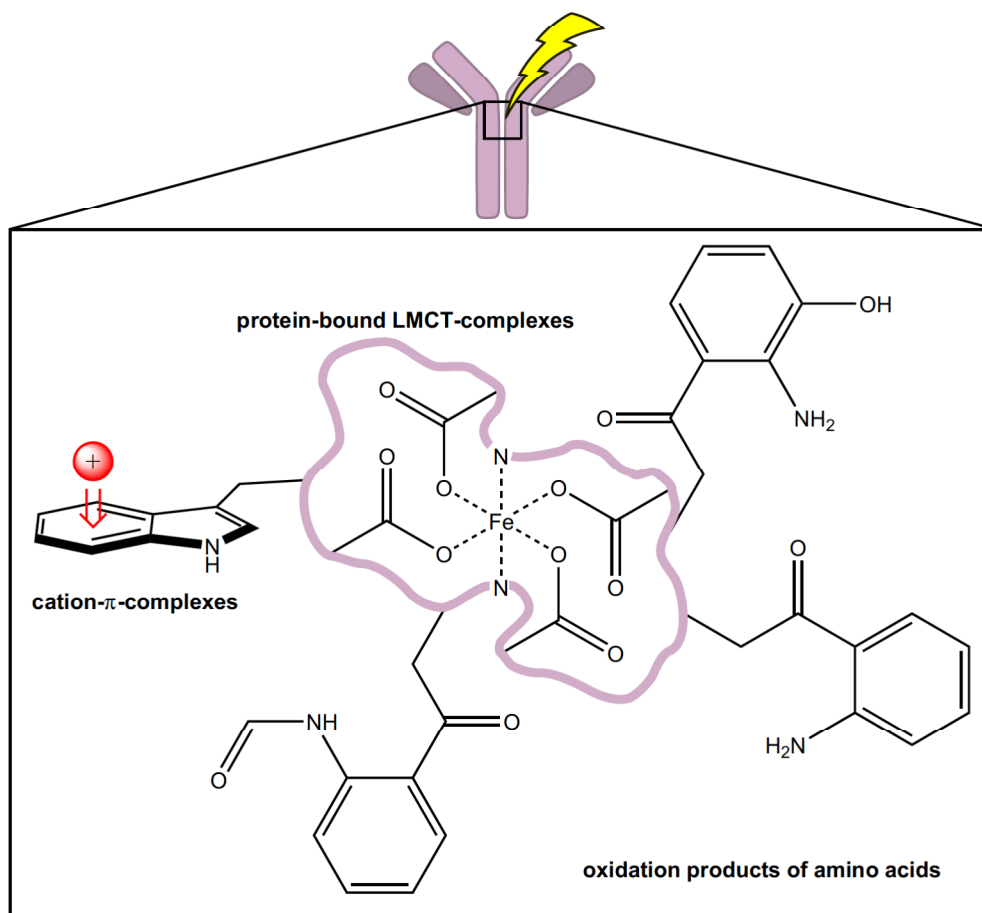


Figure 4.9: Schematic representation of possible protein-bound photosensitizers within a monoclonal antibody. The violet line represents a peptide chain of the antibody. The Trp oxidation products 3-OH-Kyn, Kyn and NFK^[109] are shown in clockwise order. The zoom is projected on the hinge region of the mAb, since Schöneich *et al.* (2022) have suggested a possible iron(III) binding site to be there^[95].

4.4.4 Buffer- and pH-dependent decay of TEMPOL in mAb solutions

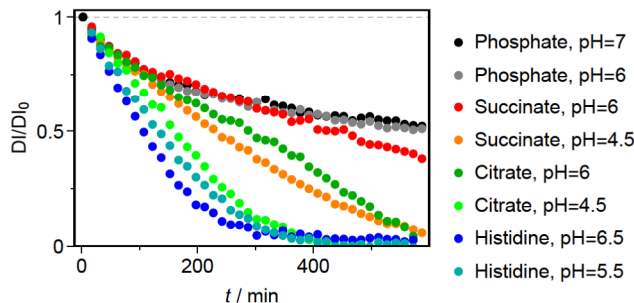


Figure 4.10: The pH- and buffer-dependent decay of TEMPOL in mAb solutions. Each sample contains 50 μM TEMPOL with 100 mg/ml of mAb-III inside different buffer solutions with different pH. The dark control measurements can be viewed in Fig. 10.32. The raw spectra are shown in Fig. 10.40 - 10.47

The buffer has a significant impact on the stability and viscosity of mAbs. In 82% of commercially available, highly concentrated mAbs (>100 mg/ml), Histidine (His) buffer is used to a great extent, because it significantly reduces viscosity and prevents aggregation^[110]. However, as shown in Fig. 4.10, His buffer (pH = 5.5-6.5) and citrate (pH = 4.5) seem to cause the fastest degradation of TEMPOL signal when irradiating mAb-III with blue light (420 nm). Phosphate buffer (pH = 6-7) has the greatest stabilizing effect.

This indicates, that an iron(III) complex might be the photosensitizer within this mAb. Iron complexes like iron(III) citrate are well known photosensitizers in the UV and visible range of light^[86,111,112]. They can produce ROS under aerobic conditions by photo-induced ligand-to-metal charge-transfer (LMCT) and an ensuing Fenton reaction^[86]. This reaction may be damaging for monoclonal antibodies (and TEMPOL), since hydrogen peroxide and hydroxyl radicals can be generated. Furthermore, His promotes photodegradation in the presence of iron^[108,110,113]. Hipper *et al.* (2022) found a decreased but still verifiable photodegradation of this mAb under a nitrogen atmosphere^[24]. This might be due to the generation of a carbon dioxide radical anion $\cdot\text{CO}_2^-$, which is possible under inert gas conditions via cleavage of the central carboxylate group of the citrate ligand in an iron(III) citrate complex^[108]. Schöneich *et al.* (2022) proposed the formation of a similar complex within the proteinogenic structure with a potential iron-binding site in an IgG1 antibody located in the hinge region at the side chains Asp²⁵², Thr²⁵⁹ and Glu²⁶¹^[95]. The presence of His leads to heavy chain fragmentation of the mAb under visible light irradiation^[95]. An excess of sequestrants like EDTA or similar chelators partially mitigate the photodegradation effect through the replacement of His in a mixed ligand mAb-iron(III)-His complex with an estimated stability constant $\log K = 26.5$ (iron(III)-EDTA complex $\log K = 25.1$)^[95,113].

4.5 Conclusion

The fiber-coupled LED irradiation setup inside the MS5000 is a suitable method for investigation of the photodegradation of monoclonal antibodies under visible light. It is superior to an approach where irradiation and EPR measurements are separated, because collection of multiple samples becomes unnecessary. This enables any desired amount of data collection, since the fiber-coupled LED irradiation EPR setup is not limited by the sample volume as it is the case with a separated setup.

Spin trapping is often considered first, when it comes to tracking the generation of radicals^[114]. However, EPR detectable adducts of spin traps usually have a limited half life of several minutes^[115], which may lead to difficulties in observation of slow radical formation via EPR due to a low steady state concentration. 4-hydroxy-2,2,6,6-tetramethylpiperidin-1-oxyl (TEMPOL) is a water-soluble, stable nitroxide radical, which can be deactivated in the presence of reactive oxygen species, alkyl-, peroxy- and hydroperoxyl radicals^[81]. This makes it suitable for tracking very slow radical generating processes over a long period of time, like demonstrated in this section for the photodegradation of mAbs during up to twelve hours of irradiation. In comparison to spin trapping, there might be no further information about the specific radical generated, since there are no EPR detectable adducts. Nevertheless, a relative interpretation of TEMPOL's EPR signal decays under different conditions may provide suitable information about the investigated photodegradation process.

The mAb concentration and buffer solution have a direct influence on the photodegradation of mAbs. Its investigation is able to give hints on the nature of a protein-bound photosensitizing species. Histidine and citrate buffer may accelerate the photodegradation in the presence of iron(III), which can be suppressed by addition of chelating agents like EDTA^[108,110,113]. In absence of metal ions, chelating agents and His buffer do not influence the photodegradation process^[116]. In this study of Schöneich *et al.* (2021), a tryptophane (Trp) oxidation product was identified as photosensitizer^[116].

For future investigation, spin labeling of mAbs at different positions could further elucidate where the photodegrading reactive species is generated within the protein structure. One could expect the radical signal to decay faster when the spin is located near the radical source.

5 The Photodegradation of Polysorbate

5.1 Introduction

Polysorbate is a class of emulsifiers that are commonly used in the food^[117,118], pharmaceutical^[28,29], and cosmetic^[119,120] industries. Surfactants such as polysorbate 20 and polysorbate 80 play a crucial role as excipients in stabilizing an active pharmaceutical ingredient like proteins, safeguarding against the development of protein particles^[30,31]. They provide protection from physical damage, which includes interface-induced protein aggregation, protein precipitation, and surface adsorption^[121–124].

Despite the advantages, photodegradation of proteins induced by UV and visible light can be observed in polysorbate containing solutions^[32,33]. Furthermore, not just structural varieties of polysorbates but also purity differences may have an impact on the magnitude of light-induced protein decay.

In this chapter, the differences in structure and purity grades of polysorbate 20 and 80 are discussed. Moreover, TEMPOL is used as EPR active spin probe for investigation of blue light (420 nm) induced polysorbate photodegradation. Additionally, 2,2,6,6-tetramethylpiperidine (TMP)^[125] and sodium azide^[126] are utilized as selective singlet oxygen ($^1\text{O}_2$) quenchers to elaborate the possible origin and properties of the reactive species as well as a visible light photosensitizer in polysorbate solutions.

5.2 Basics

5.2.1 Structure of polysorbates and its effect on therapeutic proteins

Polysorbates are copolymers produced by the reaction of sorbitol with ethylene oxide and fatty acids^[127]. Fig. 5.1 shows the structure of polysorbate 20 and polysorbate 80. According to the pharmacopoeias (Phr. Eu./USP), the approximate amount of all ethylene oxide moieties are standardized to be around 20. Nevertheless, the composition of polysorbates may vary between manufacturers and lots due to differences in raw materials and synthesis routes^[128,129]. Therefore, they can be designated as heterogeneous mixtures^[130]. The polydispersity of polysorbate is influenced by factors such as the degree of esterification, stepwise dehydration of sorbitol, and the composition of esterified fatty acids^[131,132]. About 40 to 60 % of the fatty acid in polysorbate 20 is lauric acid^[128]. The content of oleic acid within polysorbate 80 can differ from fraction to fraction in a range of 58 % up

to 98 %^[133,134], which influences the probability of subvisible particle formation but seems to have no direct effect on the stability, biological activity and innate immune response of therapeutic proteins^[134]. Contrary to this, various batches of polysorbate 20 seem to differ far more concerning micelle concentrations and effects on equilibrium surface tension, which may affect therapeutic proteins to a greater extend^[130].

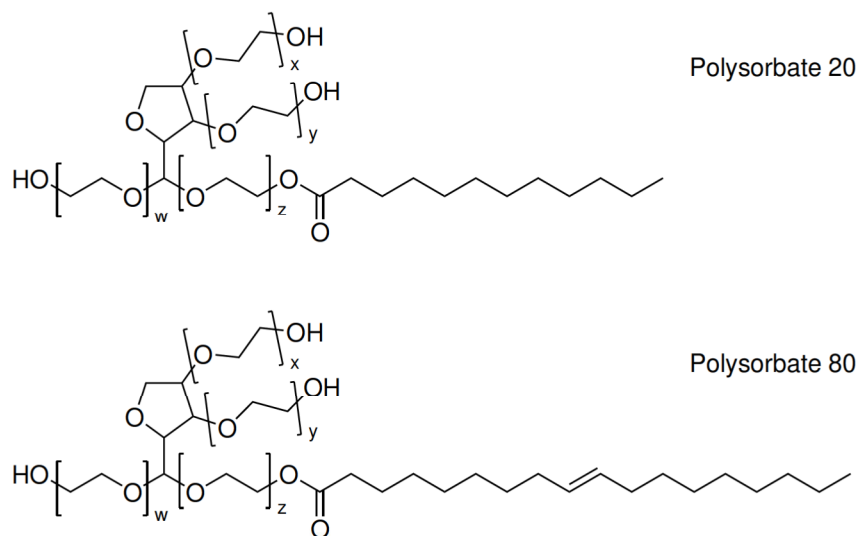


Figure 5.1: The structure of polysorbate 20 and polysorbate 80 with $w + x + y + z \approx 20$.

5.2.2 Different grades of polysorbate purity

Polysorbate is available in various purity levels, including 'High Purity' (HP) or 'Super Refined™' (SR) grades, with distinct designations from different suppliers^[129,135]. The SR grade is specifically formulated to exhibit minimal peroxide content and reduced oxidative impurities^[129]. Byproducts and process-related impurities, such as H_2O_2 , may be introduced during the manufacturing process of polysorbate^[136]. According to the pharmacopeias (Ph. Eur./USP/JP) the peroxide content in polysorbate 20 and polysorbate 80 is allowed to be up to 10 mEq/Kg^[137].

A significant concern with polysorbate is its vulnerability to degradation, which can be categorized as hydrolysis and oxidation^[138–140]. The oxidation of polysorbate can be triggered by various factors, including light, temperature, peroxides, and transition metal impurities^[138,140]. The oxidative degradation of polysorbate follows a radical cascade, resulting in the formation of peroxides^[140,141]. Its content seems to increase with storage time^[135]. These peroxides can facilitate the generation of oxygenated products in polysorbate, such as epoxides. This process may lead to the oxidation of polysorbate itself^[140,141] or compounds found in drug products, including the active pharmaceutical ingredient like a mAb^[139]. The polymeric structure of polysorbate is particularly susceptible to ox-

idation at specific sites, such as polyethylene glycol (PEG) moieties, unsaturated bonds (polysorbate 80)^[142], and ester bonds^[140,141].

5.3 Materials and methods

5.3.1 Chemicals

The different grades (High purity/HP and Super RefinedTM/SR) of polysorbate 20 and 80 were purchased from Croda International Plc. 4-Hydroxy-2,2,6,6-tetramethylpiperidine-1-oxyl (TEMPOL, 97 % purity), 4,4,6,6-tetramethylpiperidine (TMP, 99 % purity) and sodium azide (99.5 % purity) were purchased from Sigma-Aldrich Chemie GmbH (Taufkirchen, Germany).

5.3.2 EPR spectroscopy

The monochromatic irradiation setup within the MS5000 EPR spectrometer (Magnettech GmbH, Berlin, and Freiberg Instruments, Freiberg, Germany) is described in section 3.2. Micropipettes (BLAUBRAND® intraMARK, Wertheim, Germany) were filled with about 12 μ l of sample solution containing 50 μ M TEMPOL. The capillary tube sealant (CRITOSEAL® Leica) was used to close the sample tubes. The temperature was set to 25 °C (\pm 0.2 °C). A magnetic field sweep of 8 mT centered around 337.6 mT with a scan time of 60 s, a modulation amplitude of 0.05 mT (100 kHz) and a microwave power of 5 mW were used. Each spectrum is an accumulation of 5 scans. To calculate the double integrals (DI), the EPR spectra were integrated twice after a baseline correction.

5.4 Results and discussion

5.4.1 TEMPOL decay in irradiated polysorbate solutions

TEMPOL is used as EPR active spin probe for investigation of blue light (420 nm) induced photodegradation in 100 mg/ml polysorbate solutions. Polysorbate 20 and 80 are each tested in HP and SR grade. The initial EPR spectra before irradiation are displayed in Fig. 5.2. The signal intensity of TEMPOL differs according to the grades of polysorbate with 80SR > 20SR \approx 80HP > 20 HP. This may be due to the initial concentration of ROS in these solutions, which deactivate the paramagnetic nitroxide radical. The peroxide content in HP stock solutions is known to be higher than in the SR grade^[135]. This might explain the observed radical decay when mixing polysorbate and TEMPOL solutions.

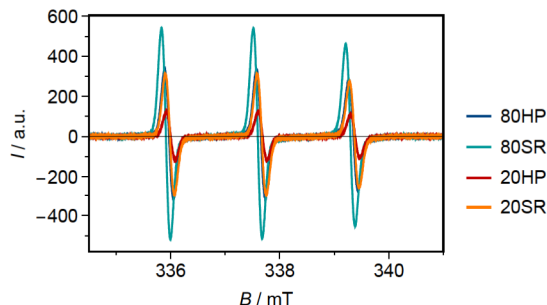


Figure 5.2: The EPR spectra of a freshly prepared solution of 50 μM TEMPOL with 100 mg/ml of polysorbate 80HP/80SR/20HP/20SR recorded at 25 $^{\circ}\text{C}$.

These solutions are irradiated with blue light (420 nm) inside the EPR spectrometer. The DI are normalized and depicted in Fig. 5.3. The fastest TEMPOL decay can be observed within the polysorbate 20HP solution. 20SR and 80SR exhibit almost no photodegradation, with 80SR being the most insusceptible to photodegradation. The dark control samples, shown in the upper right-hand corner of Fig. 5.3, emphasize that all decay is just triggered photochemically and not thermally. The magnitude of photodegradation can be explained by the coloring of the solution. At 420 nm, the absorbance of 100 mg/ml polysorbate solution ranges from ≈ 0 a.u. (80SR and 20SR) up to 0.1 a.u. (20HP) and ≈ 0.05 a.u. (80HP)^[unpublished data, manuskript in preparation, see chapter 12]. Furthermore, the broad absorption bands of polysorbate 20HP and 80HP reach up to a wavelength of approx. 500 nm and 450 nm, respectively.

Since the pure polysorbate (SR) show no absorption in the visible range^[143], the absorbance in the HP grade may originate from impurities which act as photosensitizers. With increasing cumulative light dosage, the visible light absorbance of polysorbate 20HP and 80HP decreases. This indicates a self-deactivation of the photosensitizer over time, which also explains the flattening increase of photoinduced oxidation markers^[unpublished data manuskript in preparation, see chapter 12]. Visible light photosensitizers may be introduced during synthesis of polysorbate^[127]. Catalytic amounts of metals (up to 10 ppm) are tolerated by the pharmacopeias (Ph. Eur./USP/JP)^[137] and iron might be one possible photosensitizing species^[144–146]. Doshi *et al.* (2020) reported a two to four times higher concentration of iron in the raw material of polysorbate 20HP compared to 20SR^[129].

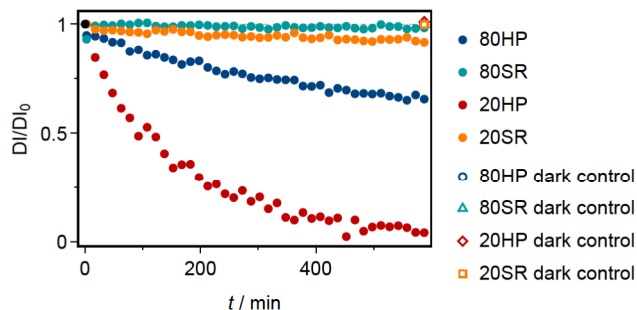


Figure 5.3: The DI decay of 50 μM TEMPOL with 100 mg/ml of polysorbate 80HP/80SR/20HP/20SR during monochromatic irradiation (420 nm) inside the MS5000 EPR spectrometer at 25 $^{\circ}\text{C}$. The raw spectra are shown in Fig. 10.48 - 10.55.

5.4.2 Selective $^1\text{O}_2$ quenching in irradiated polysorbate solutions

The presence of a photosensitizer in polysorbate was further confirmed by detecting and identifying singlet oxygen. Two methods were employed to varify the presence of singlet oxygen during visible light exposure. The initial approach utilized TEMPOL in the presence of 500 mM sodium azide (NaN_3), which selectively quenches singlet oxygen with a scavenging rate constant of $\approx 5 \times 10^8 \text{ M}^{-1}\text{s}^{-1}$ in water^[147,148]. The decay of TEMPOLs DI, shown in Fig.5.4, was compared in the presence and absence of NaN_3 during exposure to monochromatic light at 419.8 nm for approximately 600 minutes. polysorbate 20HP solutions displayed a reduction in TEMPOL of around 30 % in the presence of NaN_3 and approximately 95 % in the absence of NaN_3 after the light exposure. In polysorbate 80HP solutions, the decrease in TEMPOL content was only about -20 % in the presence of NaN_3 and roughly -30 % in its absence. Thus, it is evident that $^1\text{O}_2$ is generated by HP polysorbate solutions upon exposure to visible light and plays a significant role in the generation of ROS. Nevertheless, since the thousandfold excess of NaN_3 compared to the TEMPOL concentration does not inhibit the photodegradation, it is conceivable that $^1\text{O}_2$ may not be the only reactive species which is photochemically generated.

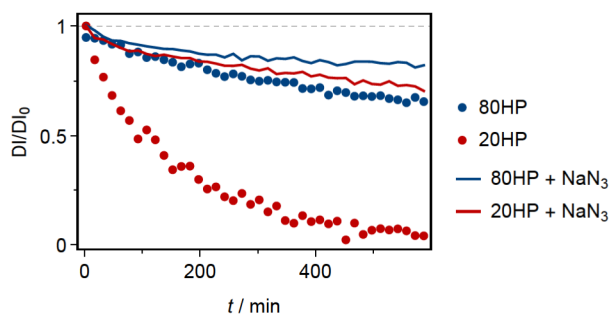


Figure 5.4: The DI decay of 50 μM TEMPOL and 100 mg/ml of polysorbate 80HP/20HP with and without 500 mM sodium azide during monochromatic irradiation (420 nm) inside the MS5000 EPR spectrometer at 25 $^{\circ}\text{C}$. The raw spectra are shown in Fig. 10.48/10.50/10.56/10.57.

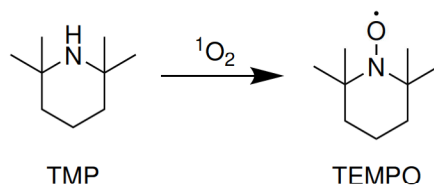


Figure 5.5: The reaction of 2,2,6,6-tetramethylpiperidine (TMP) to 2,2,6,6-tetramethylpiperidyl-1-oxyl (TEMPO) via reaction with singlet oxygen (${}^1\text{O}_2$).

The second approach for exploring singlet oxygen reactive species involves employing the spin trap 2,2,6,6-tetramethylpiperidine (TMP), which selectively reacts with singlet oxygen to the stable nitroxide radical 2,2,6,6-tetramethylpiperidyl-1-oxyl (TEMPO)^[149,150]. The reaction is displayed in Fig. 5.5. During a 60 min blue light (420 nm) irradiation of polysorbate with TMP, only 20HP exhibits a very clear generation of singlet oxygen during this short irradiation time. This aligns with the decrease in the TEMPOL signal. As a second control experiment, the polysorbate/TMP solutions were again dosed with NaN_3 which inhibits the TEMPO formation.

The presence of unsaturated fatty acids in polysorbate 80 may cause differences in the amount of detected ${}^1\text{O}_2$ between 20HP and 80HP. Oleic acid scavenges ${}^1\text{O}_2$ with a rate constant of $3 \times 10^4 \text{ M}^{-1}\text{s}^{-1}$ ^[151], which leads to a reduced reactivity towards TEMPOL/TMP. Although ${}^1\text{O}_2$ has a higher reactivity towards TMP (rate constant of $5.3 \times 10^5 \text{ M}^{-1}\text{s}^{-1}$)^[152], the photosensitizer could be bound within the polysorbate structure with a higher spatial proximity to the C-C double bond.

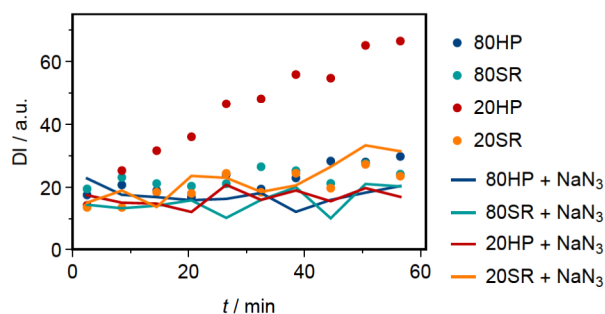


Figure 5.6: DI of 50 mM TMP and 100 mg/ml of polysorbate 80HP/80SR/20HP/20SR with and without 500 mM sodium azide during monochromatic irradiation (420 nm) inside the MS5000 EPR spectrometer at 25 °C. The dark controls are shown in Fig. 10.58. The raw spectra are shown in Fig. 10.48 - 10.70.

5.5 Conclusion

Polysorbate is a very important excipient in the pharmaceutical industry. Despite its stabilizing effects on an API, the photodegradation in the visible range of light still persists

in specific batches or high purity formulations. This may have a negative impact on API like therapeutic proteins.

TEMPOL is used to investigate the photodegradation of polysorbate 20 and 80 in different grades of purity (HP and SR) during blue light irradiation (420 nm) within the MS5000 benchtop EPR spectrometer. Polysorbate 80 induces less decay of TEMPOL under irradiation than polysorbate 20. Additionally, SR grades of both polysorbates are significantly less prone to degradation than less pure HP batches. The additional purification may remove possible visible light photosensitizers like iron^[144–146] and therefore improve the photostability of polysorbate.

Another photostability-increasing method is the addition of ROS scavengers like sodium azide and TMP for quenching of singlet oxygen^[125,126]. Polysorbate 20 was more stabilized after the addition of a quencher than polysorbate 80 compared to each initial photodegradation. This may arise from the unsaturated fatty acid in the structure of polysorbate 80. The C-C double bond can also act as a ROS quencher^[151], which might lead to a self-stabilizing effect.

In case of pharmaceutical application, polysorbate 80 should be used in its SR purity grade for the least amount of visible light photodegradation caused by this excipient. Furthermore, the unsaturated fatty acid in polysorbate 80 might be able to inhibit photodegradation caused by the API like a mAb itself. This potentially beneficial effect of overwhelmingly pure polysorbate 80 is yet to be investigated.

6 Bergman Cyclisation of Main-Chain Eneidyne Polymers

6.1 Introduction

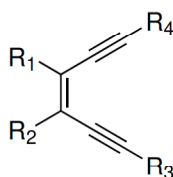


Figure 6.1: The enediyne (EDY) structure.

The enediyne (EDY) structure (Fig. 6.1) is known to produce reactive 1,4-dehydroaromatics via ring formation since the early 1970s^[153,154]. The significance of enediynes in natural antibiotics, such as neocarzinostatin chromophore, calicheamicins, esperamicins, and dynemicins, where in situ-generated diradicals induce DNA strand cleavage, has fueled intense interest in enediynes and the Bergman cyclization for many years^[34–37].

EDY-containing precursor polymers, as sources of reactive diradicals, have been utilized to construct linear conjugated polycyclic networks^[155], crosslinked polymers^[156], brush polymers^[157,158], and single-chain polymer nanoparticles^[159]. The integration of EDY into the main-chain of a polymer was successfully implemented by Cai *et al.* (2022)^[38].

In this chapter, the mechanism of the Bergman cyclisation and its application in main-chain enediyne polymers are discussed. EPR spectroscopy is utilized to investigate the photochemical and heat-induced radical formation and stability of different main-chain EDY polymers. Furthermore, TEMPOL is used as a radical scavenger to mimic an DNA cleavage experiment as published by Cai *et al.* (2022)^[38]. Moreover, compressed polymers are examined to elaborate on the influence of mechanical stress; and how the crosslinking mechanism may be influenced by the polymer structure in close proximity to the generated diradical.

6.2 Basics

6.2.1 Bergman cyclisation mechanism

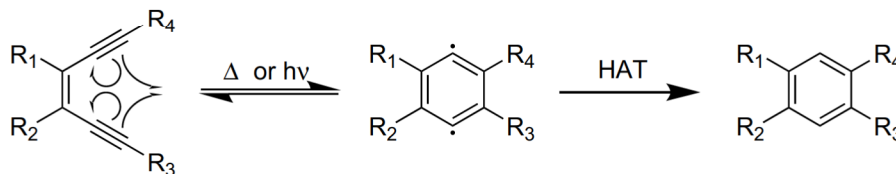


Figure 6.2: The Bergman cyclisation reaction mechanism of an enediyne structure can be triggered by light or heat. One electron pair in both carbon-carbon triple bonds will be split. Due to the planar enediyne structure a ring formation is prearranged and realised by recombination of the two outer electrons. The two remaining electrons are *para*-positioned in the σ -orbitals of the benzene ring. These radicals can be scavenged via an inter- or intramolecular hydrogen atom transfer (HAT).

The general Bergman cyclization mechanism is depicted in Fig 6.2. By thermal or photochemical activation of EDY structure a ring formation is induced which results in the emergence of two *para*-positioned σ -radicals^[154,160]. These reactive radicals abstract adjacent hydrogen atoms via a hydrogen atom transfer (HAT) reaction^[161].

In detail, the light- or heat-induced splitting of one electron pair of each acetylene groups into diradicals enables bending of these previously stiff groups. The bond angle at the carbon atoms, where the σ -radicals are localized, decreases from 180° to $\approx 140^\circ$. This reduces the distance between the outer carbon atoms, which also possess unpaired electrons. Subsequently, these electrons close the ring via a carbon-carbon bond formation^[162].

6.2.2 Main-chain enediyne polymers

The generation of reactive diradicals via Bergman cyclisation in polymers enables crosslinking of polymer chains^[163]. Cai *et al.* (2022)^[38] established a route of synthesizing novel polymers with an (*Z*)-octa-4-en-2,6-diyne-1,8-diamine (EDY-II, Fig. 6.4) motif integrated in the main-chain. This can be achieved by polycondensation of EDY-II with dialdehydes, which yields polyimines.

Since the stability of EDY-II is limited, it has to be produced *in situ* immediately before the polycondensation. Therefore, di-*tert*-butyl octa-4-en-2,6-diyne-1,8-diyl(*Z*)-dicarbamate (EDY-I/Boc-protected EDY-II) has to be deprotected before addition of dialdehydes in a 1/1 ratio^[38].

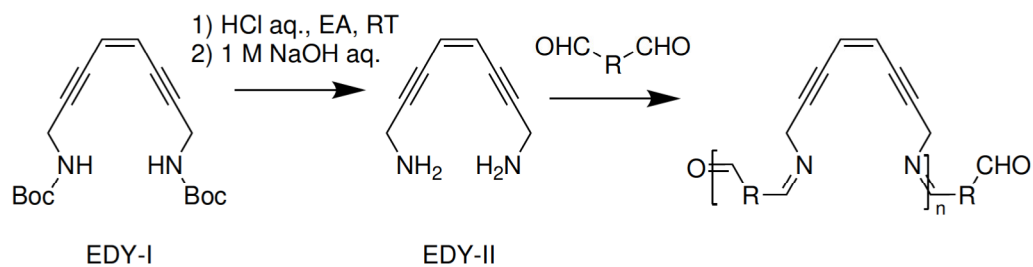


Figure 6.3: The general synthesis of main-chain enediyne polymers according to Cai *et al.* (2022)^[38]. The amine groups of EDY-I are deprotected to yield the labile EDY-II, which is used as reactant together with a dialdehyde for a polycondensation reaction.

6.3 Materials and methods

6.3.1 Chemicals

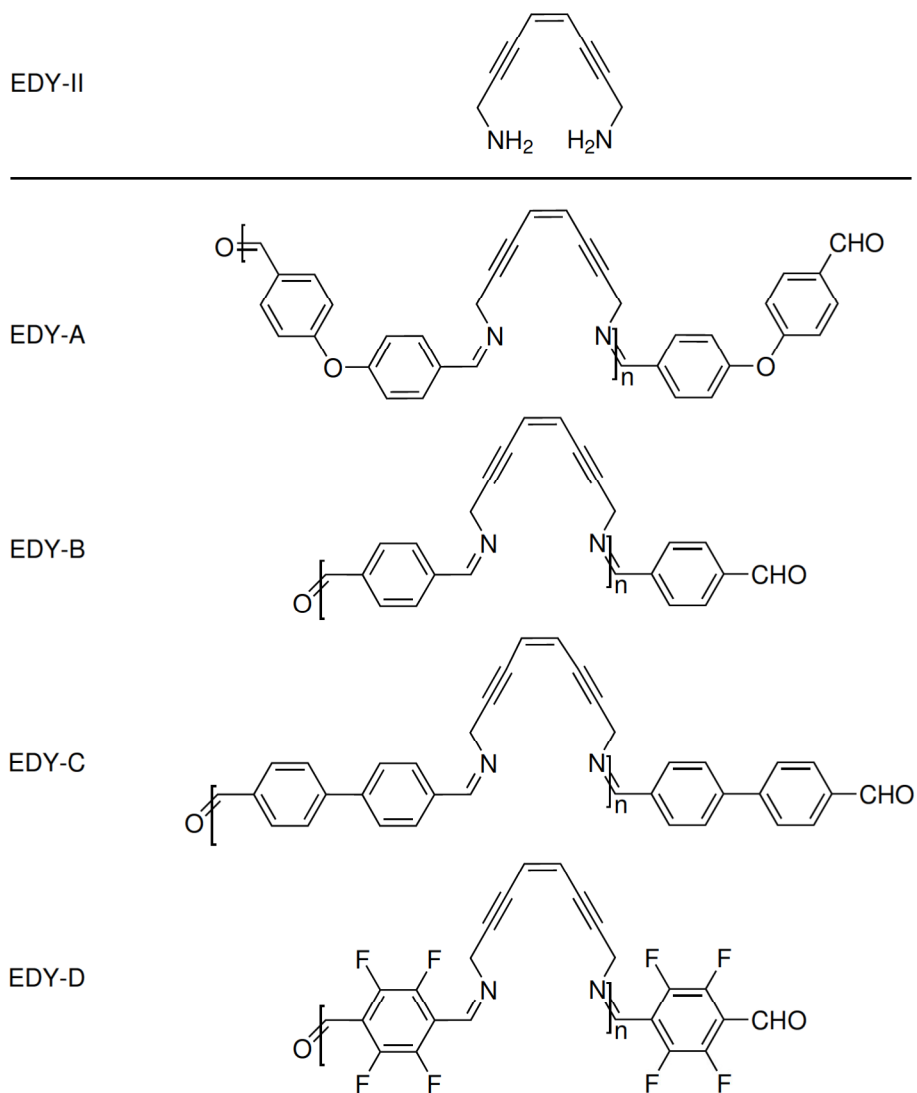


Figure 6.4: Structure of the monomer EDY-II and polymers EDY-A, EDY-B, EDY-C and EDY-D according to Cai *et al.* (2022)^[38].

All substances shown in Fig. 6.4 and 6.5 were synthesized by Yue Cai according to Cai *et al.* (2022)^[38] and Binder and colleagues (2023)^[164], respectively. All abbreviations were inherited from the literature^[38,164]. 4-hydroxy-2,2,6,6-tetramethyl-piperidin-1-oxyl (TEMPOL, 97 % purity), dichloromethane (DCM, >99.5 % purity) and dimethyl sulfoxide (DMSO, 99.7 % purity) were purchased from Sigma-Aldrich Chemie GmbH (Taufkirchen, Germany).

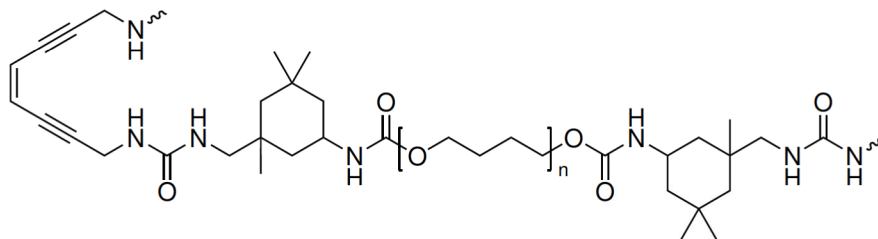


Figure 6.5: Structure of the polymer PIE according to Binder and colleagues (2023)^[164].

6.3.2 EPR spectroscopy

Sample preparation

The solutions of 20 mM EDY-A/B/C/D with 50 μ M TEMPOL were prepared in Tris-EDTA (TE) buffer with 6.6 vol% DMSO^[38]. Micropipettes (BLAUBRAND® intraMARK, Wertheim, Germany) were filled with about 12 μ l of sample solution containing 50 μ M TEMPOL. The capillary tube sealant (CRITOSEAL® Leica) was used to close the sample tubes.

Solid samples were put inside a 3 mm sample tube, which was closed with capillary tube sealant (CRITOSEAL® Leica).

The solid EDY-II was expected to be unstable. Therefore, immediately after synthesis, approx. 120 μ l solution of pure EDY-II in DCM was filled in a 3 mm sample tube. Afterwards, compressed air was utilized to evaporate the solvent in about five minutes. As soon as the solid was dry, it was placed in the MS5000 EPR spectrometer and spectra were collected.

Light-induced Bergman cyclisation inside the MS5000 EPR spectrometer

The monochromatic irradiation setup within the MS5000 EPR spectrometer (Magnettech GmbH, Berlin, and Freiberg Instruments, Freiberg, Germany) is described in section 3.2. The temperature was set to 25 °C (± 0.2 °C). A magnetic field sweep of 8 mT centered around 338 mT with a scan time of 60 s, a modulation amplitude of 0.05 mT (100 kHz) and a microwave power of 10 mW were used. Each spectrum is an accumulation of 10 scans. To calculate the double integrals (DI), the EPR spectra were integrated twice after a baseline correction.

Heat-induced Bergman cyclisation inside the MS5000 EPR spectrometer

CW EPR spectra were measured using the MS5000 EPR spectrometer (Magnettech GmbH, Berlin, and Freiberg Instruments, Freiberg, Germany). The temperature inside the spectrometer was set to 25 °C (± 0.2 °C) and gradually increased to 175 °C in steps of 25 °C. Before starting each measurement, the sample was equilibrated at each temperature for

20 min. A magnetic field sweep of 8 mT centered around 338 mT with a scan time of 60 s, modulation amplitude of 0.05 mT, modulation frequency of 100 kHz and a microwave power of 10 mW were set. Each spectrum is an accumulation of 10 scans.

TEMPOL as a radical scavenger

The monochromatic irradiation setup within the MS5000 EPR spectrometer (Magnettech GmbH, Berlin, and Freiberg Instruments, Freiberg, Germany) is described in section 3.2. The temperature was set to 37 °C (± 0.2 °C). A magnetic field sweep of 8 mT centered around 337.6 mT with a scan time of 60 s, a modulation amplitude of 0.05 mT (100 kHz) and a microwave power of 5 mW were used. Because of the fast decay of TEMPOL signal (Fig. 6.10), the double integrals (DI) were obtained every minute from each scan.

6.3.3 Mechanical stress

10 tons of force were applied on the polymer PIE. The compression was performed by Yue Cai according to the literature^[164].

6.4 Results and discussion

6.4.1 Radical generation and stability in main-chain enediyne polymers

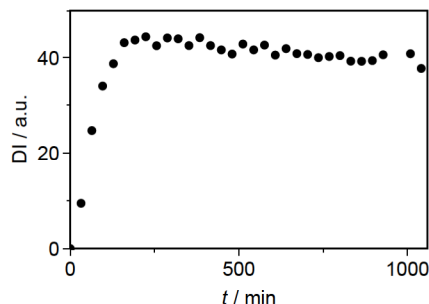


Figure 6.6: DI calculated from EPR spectra (Fig. 10.71) of freshly prepared solid EDY-II, after evaporating the solvent (DCM) at RT.

Firstly, the monomer EDY-II is tested. After evaporation of the solvent, EPR spectra of the sample were collected at RT, which is shown in Fig 6.6. Since the DI correlate with the amount of spins inside the resonator, a quick generation of carbon radicals can be observed during the first 225 min. A slow radical decay starts after the maximum is reached. No light reaches the sample during measurement, therefore the ambient temperature in the laboratory seems to be enough for triggering the Bergman cyclisation even in absence of light. Its initiation in EDY-II is inevitable.

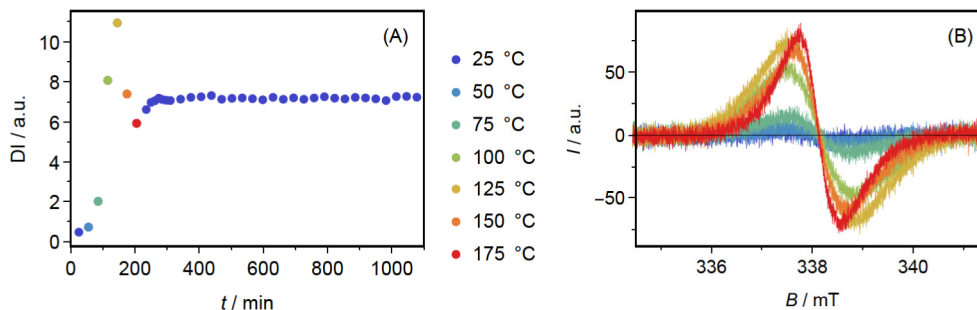


Figure 6.7: Stepwise heating of EDY-A from 25 °C to 175 °C in steps of 25 °C and then cooling down back to 25 °C inside the EPR spectrometer. The temperature changed every 30 min and an EPR spectrum was collected (B). After cooling down to 25 °C, the temperature remained constant and further EPR spectra were collected every 30 min (Fig. 10.72). The DI was calculated from all these spectra and plotted against the time (A).

Compared to EDY-II, the behavior of the EDY-group inside a polymer chain is significantly different. Fig. 6.7 (B) shows the EPR spectra of EDY-A at various temperatures. The related DI(t) curve is depicted in Fig. 6.7 (A) with consecutive periods of repeated measurements at RT to examine the stability of generated radicals. From 25 °C to 75 °C the conditions for the thermally induced Bergman cyclisation are not optimal, hence the DI increases just slightly. The most rapid jump in DI can be observed between 75 °C and 100 °C and reaches its maximum at 125 °C. After that the temperature is still rising but the DI decreases. Thenceforward, when the temperature is held constant at 25 °C, the DI is constant at a higher value compared to the start of the reaction. This is proof for the generation of stable radicals inside the polymer.

The EPR spectra shown in Fig. 6.7 (B) enable a detailed discussion about the proposed mechanism of the radical generation and recombination inside the polymer chain (Fig. 6.8). With increasing DI, the linewidth of the carbon radical signal broadens. Weak dipole-dipole interactions between nearby radicals may cause this so-called inhomogeneous broadening^[1]. These interactions increase with radical concentration^[165]. As the radicals combine through formation of crosslinks inside the polymer, the amount and the average distance between radicals decrease resulting in lower DI and linewidth, respectively (Fig. 6.7, 150 °C and 175 °C).

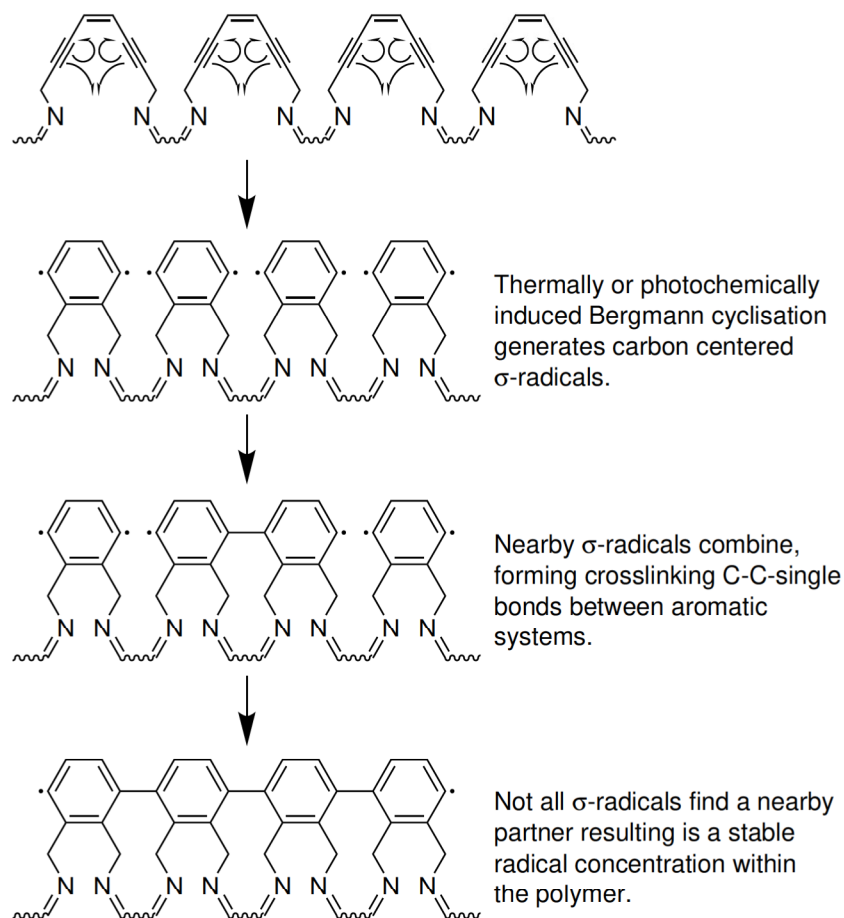


Figure 6.8: The proposed mechanism of radical generation via Bergman cyclisation and subsequent partial recombination of σ -radicals.

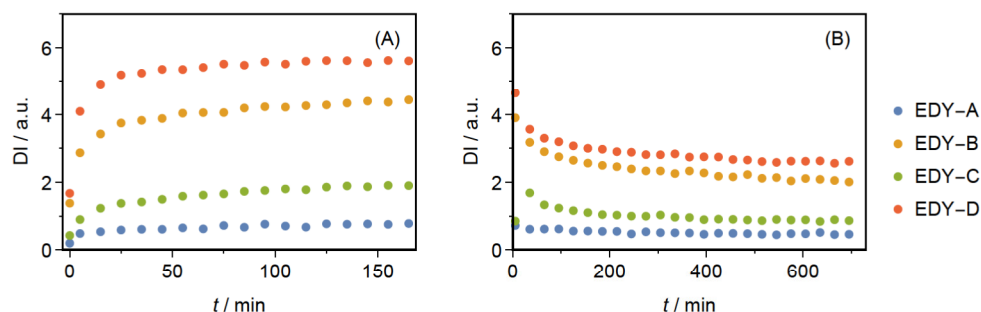


Figure 6.9: (A): The radical generation during monochromatic irradiation (420 nm) of polymers EDY-A/B/C/D measured inside the MS5000 EPR spectrometer at 25 °C. Immediately after (A), the light was switched off to monitor the radical decay and stability (B). The mass of the polymer samples vary from 1.84 mg to 2.4 mg, therefore, the DI is normalized on the initial mass of the samples. The raw spectra are shown in Fig. 10.73-10.80.

In addition to heat-induced Bergman cyclisation, it can also be initiated photochem-

ically^[154,166]. During blue light (420 nm) irradiation (Fig. 6.9 (A)), the DI increases to a maximum in each polymer as long as the LED is switched on. With absence of light (Fig. 6.9 (B)), recombination of the σ -radicals induces a quick decay of the observed EPR signal, which slowly converge to a stable radical concentration.

Although the fundamental trend is similar for each polymer, the quantity of generated radicals differ from polymer to polymer. EDY-D and EDY-B exhibit a significantly higher radical concentration than EDY-C and EDY-A during irradiation as well as afterwards. Various substituents bound to the EDY structure may influence the Bergman cyclisation efficiency via electronic effects^[167]. However, the EDY groups and non-EDY-components in the polymer chain are not conjugated, therefore, the specific structure may have no significant impact on the Bergman cyclisation. The differences in Fig. 6.9 might arise from various EDY concentrations inside the resonator due to the sheer spatial proportions of the non-EDY-components inside each polymer chain. Smaller groups like the terephthyl or 2,3,5,6-tetrafluoroterephthyl group in EDY-B and EDY-D, respectively, permit a tighter packing^[168] of EDY groups and a therefore higher observed radical concentration.

6.4.2 Scavenging of TEMPOL radicals in solution

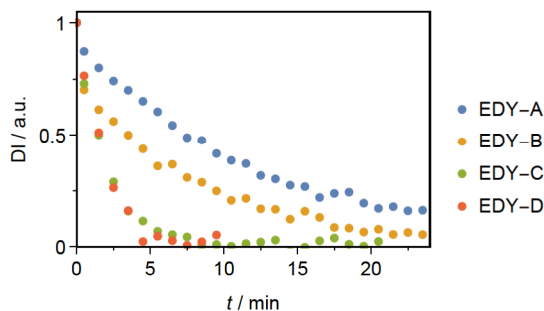


Figure 6.10: The DI decay of 50 μ M TEMPOL during irradiation of 20 mM Poly EDY-A/B/C/D solutions in TE buffer with 6.6 vol% DMSO at 37 °C. The raw spectra are shown in Fig. 10.81-10.84.

An application of main-chain enediyne polymer is DNA cleavage^[38]. These experiments are performed in an aqueous solution with the polymer, TE buffer and DMSO. Therefore, investigation of these polymers in solution is of interest. Unfortunately, the immediate HAT from surrounding solvent molecules to a σ -radical inhibits a direct observation with CW EPR spectroscopy when the polymers are dissolved^[169].

Therefore, TEMPOL is used as EPR active spin probe for investigation of blue light (420 nm) induced Bergman cyclisation in solution. Its decay is shown in Fig. 6.10. Contrary to the results in solid state, the polymer reactivity with TEMPOL in solution could indicate a stereoelectronic impact of the non-EDY-components on EDY in the polymer chain. This matches with the findings of Cai *et al.* (2022)^[38], where DNA cleavage

was performed under identical conditions with equal concentrations of enediyne segments (200 mM). A distinct stereoelectronic impact on DNA cleavage was observed. EDY-D, featuring tetrafluoro segments, and EDY-C, characterized by biphenyl structures, induced rapid cleavage, whereas EDY-B, with terephthyl groups, and EDY-A, derived from 4,4'-oxydibenzaldehyde, exhibited slower rates of cleavage^[38]. This may be explained by the electron-withdrawing effect of substituents, which might decrease the electron density in the σ -HOMO orbital. This could result in stabilizing the transition state and consequently lowering the barrier for Bergman cyclization^[38,170].

However, the DNA cleavage and TEMPOL decay experiment are both bimolecular reactions. Therefore, the conformation of the polymer chain and thereby the exposition of EDY groups to potential reactants in solution have to be taken into consideration^[171,172]. Moreover, it is conceivable that the non-EDY-components in the polymer chain may have different DNA binding affinities^[173,174]. Without further investigation it remains ambiguous if the reactivity differences between the polymers and a reactant are a consequence of specific influences on Bergman cyclisation itself or a result of distinct inter- and intramolecular interactions.

6.4.3 Influence of mechanical stress on the Bergman cyclisation

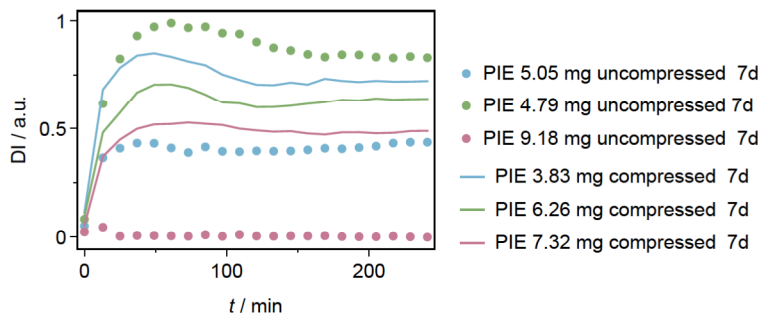


Figure 6.11: The heat-induced radical generation of PIE samples with and without 7 days of compression measured inside the MS5000 EPR spectrometer. Samples from the same batch are colored equally (blue, green or red). At $t=0$ min, the initial spectrum is recorded at RT. During the first ≈ 8 min, the temperature was increased to 175 °C and kept constant. The DI is normalized to the mass of each sample. The raw spectra are shown in Fig. 10.85 - 10.90.

The activation barrier for the Bergman cyclization can be reduced by increased bending of the interior angles at the proximal alkyne carbons in the EDY structure^[175]. Binder and colleagues (2023) found increased tensile strength of the polymer PIE after compression or stretching^[164]. Furthermore, DSC experiments revealed a decreased ΔH of compressed PIE compared to an uncompressed sample^[164]. This indicates a compression-induced Bergman cyclization with a subsequent crosslinking of PIE polymer chains.

If the polymer chains are crosslinked, the compressed sample should generate less radi-

cals upon heating compared to the uncompressed one since some EDY structures may have already reacted. However, this hypothesis can not be confirmed by the performed EPR experiments. As depicted in Fig. 6.11, compressed and uncompressed samples of three different batches of PIE show no consistent trend in radical generation. Two compressed samples lead to a higher DI than the uncompressed control samples and one PIE sample demonstrates the opposite behavior. Furthermore, an EPR signal of a nitrogen centered radical can occasionally be found in the provided PIE polymers (Fig. 6.12). These signals are difficult to detect because of the broad band and low signal-to-noise ratio, especially when the nitroxide is immobilized like depicted in Fig. 6.12 (C). They disappear during heating as soon as carbon centered radicals are generated and exhibit a significantly lower intensity (Fig. 10.88).

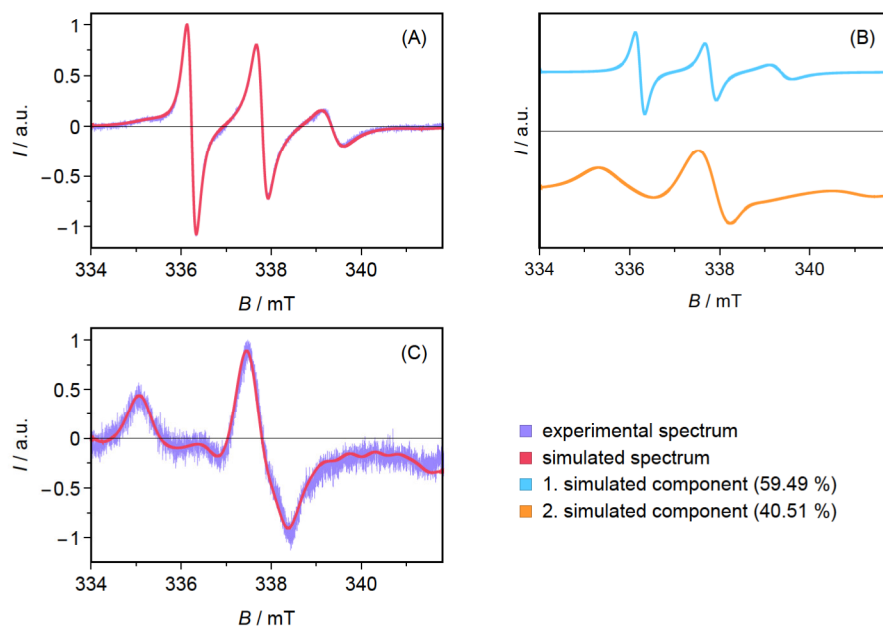


Figure 6.12: EPR spectra of one batch of PIE after synthesis (A) and after 7 days of storage (C). The experimental spectra and the simulated spectra depicted in purple and red, respectively. The simulated spectrum in (A) consists of two components shown in (B).

To prove the presumed characteristics of a radical, EPR spectrum simulations with the MATLAB toolbox *EasySpin* were performed^[76,77]. The EPR spectrum of PIE shown in Fig. 6.12 (A) was measured a few hours after synthesis. The spectrum simulation is a combination of two nitrogen centered radical species, separately plotted in Fig. 6.12 (B). The full set of simulation parameters is listed in Tab. 10.1. The first simulated component is a fast rotating radical with a rotation correlation time τ_c of 0.9 ns, which can be labeled as unbound radical. The second simulated component rotates much slower ($\tau_c = 5.3$ ns). After seven days of compression, the signal of unbound radical disappeared completely and one component with fully inhibited motion and $\tau_c = 905$ ns arises (Fig. 6.12 (C)).

The presence of nitrogen centered radicals indicate a more eclectic reaction mechanism for the PIE polymer than the one proposed in the previous section (Fig. 6.8). The structure of PIE, shown in Fig 6.5, is more complex than the structures of the EDY polymers (Fig. 6.4). PIE contains amide groups with nitrogen-bound hydrogen atoms. In addition to possible formations of carbon-carbon bonds by combination of two σ -radicals, such a reactive species may abstract a hydrogen atom from a nitrogen atom in the polymer chain. After this HAT, the unpaired electron might be localized at a nitrogen atom. This alternative mechanism would also lead to a crosslinking of PIE and a reduction in ΔH as reported in the DSC measurements by Binder and colleagues^[164]. Furthermore, PIE crosslinking and the consequentially increased stiffness of the polymer could explain the demobilization of the radical shown in Fig. 6.12 (C).

Further investigations could explicitly focus on the intramolecular atom transfer mechanisms in EDY/PIE polymers with related identification of intermediate radicals and the influence of substituents on their stability^[176].

6.5 Conclusion

The EDY structure is very unique due to its capability of generating highly reactive σ -radicals via photochemically or heat-induced Bergman cyclisation^[153,154]. The incorporation of EDY in the main-chain of polymers enables fine-tuning of parameters like stability and reactivity of both the EDY group and the eventually generated radicals. The non-EDY-components inside the polymer main-chain have a significant impact, since they determine the flexibility of the polymer chain and the distance between EDY groups, as well as the stereoelectronic influence on the EDY group. This can be observed in its efficiency as a DNA cleaver. The polymer EDY-D, containing 2,3,5,6-tetrafluoroterephthyl groups and EDY groups, shows the highest rate of radical generation as well as DNA cleavage.

EPR spectroscopy is a suitable method for the investigation of radicals inside EDY polymers. Observed signals of nitrogen-centered radicals in the polymer PIE indicate a more versatile crosslinking mechanism than just the recombination of generated σ -radicals. The amide groups with abstractable hydrogen atoms inside the polymer main-chain may serve as an intramolecular reactant towards reactive dehydroaromatics. Further investigations might be of interest. Different functional groups could be implemented in the main chain to selectively direct crosslinking. Spin-trapping may be used to uncover transition radicals and help to elucidate the underlying mechanism in more detail.

7 Investigation of Photoresponsive LCST-Polymers

7.1 Introduction

Photoactive moieties like spiropyrans^[177,178], cinnamates^[42,179], and azobenzenes^[180,181] can undergo structural changes, which alter their polarity and hydrophilicity. Among these, azo dyes are capable of *E*–*Z* photoisomerization, which increases their dipole moment, consequently enhancing their solubility in water. This process is reversible and virtually devoid of side reactions^[39].

Such light-responsive systems can be applied within a polymer matrix^[40,41]. This strategy allows for the manipulation of the phase transition temperature of thermo-responsive polymers, facilitating isothermal switching through irradiation as an alternative to temperature-induced switching^[39,42]. To ensure a high selectivity of such a reversible *E*–*Z* photoisomerization, the absorption bands of the *cis*- and *trans*-isomers have to be separated^[182].

Compounds based on aryl azopyrazole (AAP) exhibit such separated absorption bands as well as a long life time (10-1000 days) of the metastable *cis*-isomer^[183]. They find utility in surface modification^[184,185], as well as in the development of photo-responsive gelators^[186,187], enzyme inhibitors^[188,189], and shape memory materials^[190]. Furthermore, Steinbrecher *et al.* (2024)^[191] managed to integrate AAP-chromophores as a photo-trigger within thermo-responsive polymers to regulate their lower critical solution temperature (LCST) or coil-to-globule collapse transition temperature.

An increasing interest in photo-responsive polymers for target-specific and controlled drug delivery can be observed in recent years^[43–45]. Therefore, in this chapter, AAP-containing thermo- and photoresponsive polymers are characterized regarding their binding affinity towards the hydrophobic fatty acid model compound 5-DOXYL stearic acid (5-DSA), which can be investigated via EPR spectroscopy. The fiber-coupled LED irradiation setup enables selective photoisomerization within the EPR spectrometer and EPR spectrum simulations with the MATLAB toolbox *EasySpin*^[76,77] are applied to extract specific binding properties from the shape of the EPR spectrum. These are analyzed with a view on AAP-content of the polymer, differences of the *E*/*Z*-isomers and the impact of temperature.

7.2 Basics

7.2.1 Light-induced *E*–*Z* isomerisation of aryl azopyrazole

Photoinduced isomerization systems play a crucial role in chemical dynamics by leveraging light energy to drive molecular rearrangements. Upon absorption of light, molecules undergo electronic transitions to higher energy states, leading to alterations in their geometric configurations^[15,192].

The light-induced *E*-*Z* isomerization of AAP involves the reversible transformation between two geometric isomers, typically denoted as the *E* (*trans*) and *Z* (*cis*) isomers. AAP refers to a compound containing an azo group (-N=N-) attached to an aryl group (typically a phenyl ring) and a pyrazole ring^[192].

Upon absorption of light, the molecule undergoes excitation, leading to the promotion of electrons from the ground state to higher energy electronic states, usually the excited singlet state^[15]. This electronic excitation initiates a series of molecular rearrangements, ultimately resulting in the conversion between the *E* and *Z* isomeric forms. The azo group exhibits an in-plane lone electron pair in an π -orbital. Consequently, both the n,π^* and π,π^* excited states are implicated in two possible mechanisms of photoisomerization. The first mechanism involves a 180° rotation (twist) around the former double bond, accompanied by a reduction in bond order. In the second scenario, an in-plane inversion occurs as a result of the rehybridization of one nitrogen atom, with no significant alteration in the bond order. The specific isomerization pathway is contingent upon the type of excitation. Quantum chemical calculations and time-resolved experiments indicate that rotational *E*-*Z* interconversion in imines and azo compounds typically arises from their $^1n,\pi^*$ and $^3n,\pi^*$ states^[15].

7.2.2 Synthesis of DMAM-AAPEAm_x polymers

DMAM-AAPEAm_x polymers are copolymers of dimethyl-acrylamide (DMAM) and ethylazopyrazole-acrylamide (AAPEAm) with an AAP content of *x* ($[x] = \%$)^[191]. The synthesis of such a copolymer includes six steps, which are depicted in Fig. 7.1. Firstly, *p*-nitroaniline is diazotized with sodium nitrite and exposed to pentane-2,4-dione (Fig. 7.1 (a)). Secondly, a cyclisation reaction is performed with hydrazine to yield the aryl azopyrazole (Fig. 7.1 (b)), which is subsequently ethylated via a nucleophilic substitution with ethyl bromide (Fig. 7.1 (c)). After that, the nitro group is reduced with sodium sulfide (Fig. 7.1 (d)) and the newly formed amino group reacts with acryloyl chloride in the following step (Fig. 7.1 (e)). Finally, the statistical copolymerisation of AAPEAm and DMAM can be realised in dry THF utilizing the radical initiator AIBN (Fig. 7.1 (f))^[191].

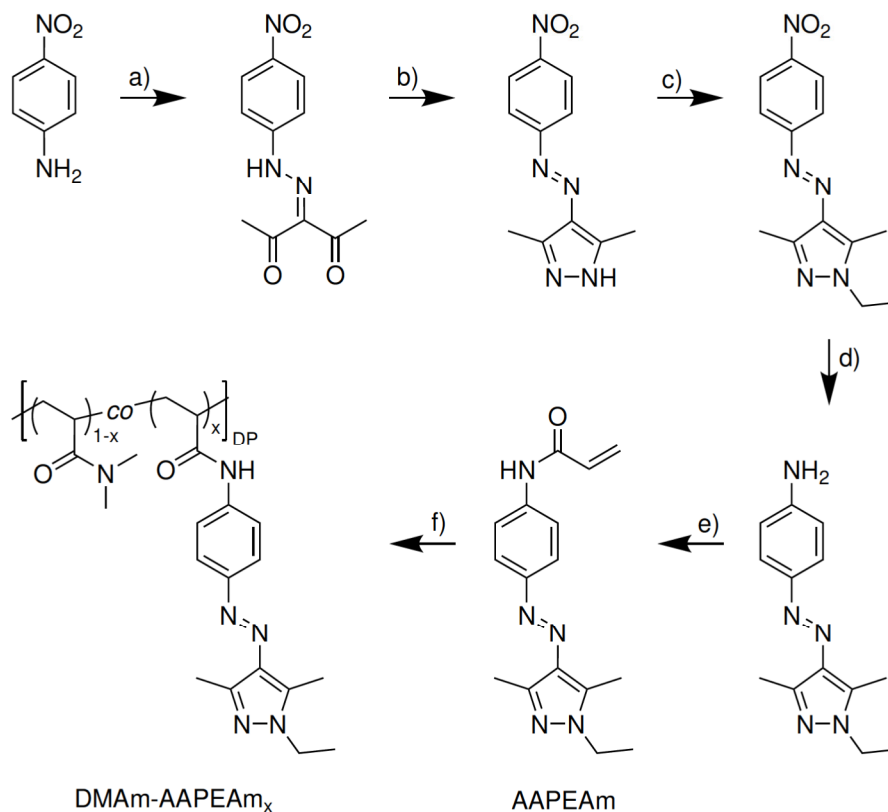


Figure 7.1: The synthesis of DMAm-AAPEAm_x, copolymers of dimethyl-acrylamide (DMAm) and ethyl-azopyrazole-acrylamide (AAPEAm), according to Steinbrecher *et al.* (2024)^[191]. a) NaNO₂/HCl/pentane-2,4-dione. b) hydrazine. c) EtBr. d) Na₂S. e) acryloyl chloride. f) DMAm/AIBN/THF.

7.3 Materials and methods

7.3.1 Chemicals

The monomer ethyl-azopyrazol-acrylamide (AAPEAm) and all copolymers of dimethyl-acrylamide (DMAm) and AAPEAm with the general structure shown in Fig. 7.2 were synthesized by René Steinbrecher according to Steinbrecher *et al.* (2024)^[191]. All abbreviations were inherited from the literature^[191]. For each polymer, the degree of polymerization (DP) and the azopyrazole content (x) are listed in Tab. 7.1.

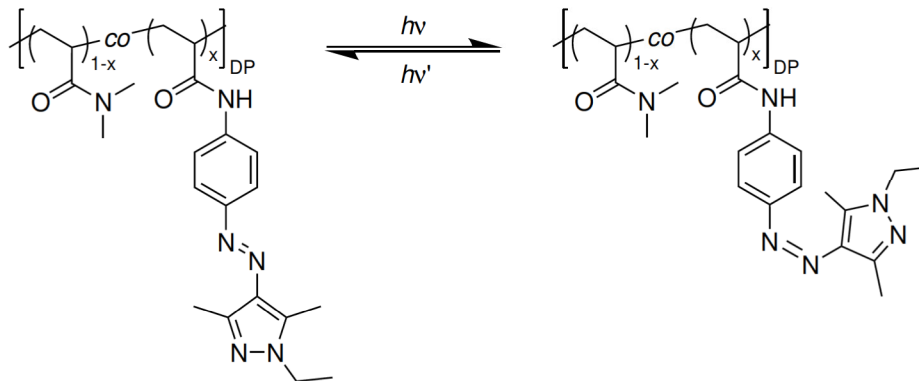


Figure 7.2: The general structure of DMAm-AAPEAm_x, copolymers of dimethyl-acrylamide (DMAm) and ethyl-azopyrazole-acrylamide (AAPEAm), according to Steinbrecher *et al.* (2024)^[191].

Table 7.1: The degree of polymerization (DP) and the azopyrazole content (x) of polymers investigated in this chapter. The general structure is depicted in Fig. 7.2^[191].

polymer	DP	x
DMAm-AAPEAm _{1.5}	115	1.5±0.5
DMAm-AAPEAm _{4.5}	120	4.5±0.5
DMAm-AAPEAm ₇	157	7.0±0.7
DMAm-AAPEAm ₈	101	8.0±0.8
DMAm-AAPEAm _{9.5}	147	9.5±1.0
DMAm-AAPEAm ₁₁	178	11.0±1.1

5-DOXYL stearic acid, ammonium salt (5-DSA, >99 % purity) was purchased from Avanti Polar Lipids (Alabaster, USA). Methanol (MeOH, HPLC-grade/>99.9 % purity) was procured from Sigma-Aldrich Chemie GmbH (Taufkirchen, Germany).

7.3.2 EPR spectroscopy

The monochromatic irradiation setup within the MS5000 EPR spectrometer (Magnettech GmbH, Berlin, and Freiberg Instruments, Freiberg, Germany) is described in section 3.2. Micropipettes (BLAUBRAND® intraMARK, Wertheim, Germany) were filled with about 10 µL of sample solution containing 10 mg/ml polymer and 100 µM 5-DSA. AAPEAm had to be dissolved in MeOH, due to low solubility in water. The capillary tube sealant (CRITOSEAL® Leica) was used to close the sample tubes.

The light-induced isomerization experiments were performed at 25 °C (± 0.2 °C). For recording a temperature series, the temperature inside the spectrometer was set to 15 °C (± 0.2 °C) and gradually increased to 75 °C in steps of 5 °C. Before starting each measurement, the sample was equilibrated at each temperature for 2 min.

A magnetic field sweep of 12 mT centered around 338 mT with a scan time of 60 s, a

modulation amplitude of 0.1 mT (100 kHz) and a microwave power of 4.8 mW were used to obtain EPR spectra. Each spectrum is an accumulation of 10 scans.

7.3.3 UV/Vis absorption spectroscopy

The absorption spectra of DMAm-AAPEAm solutions were recorded on a HP/Agilent 8453 UV/Vis Spectrophotometer (Agilent Technologies, Santa Clara, USA). The samples were filled inside a 500 μ l quartz glass cuvette with an optical path length of 10 mm. Photoisomerisation was performed via irradiation of the cuvette outside of the spectrometer using the LEDs of the fiber-coupled irradiation unit.

7.4 Results and discussion

7.4.1 Spin probe selection for investigation of hydrophobic interactions

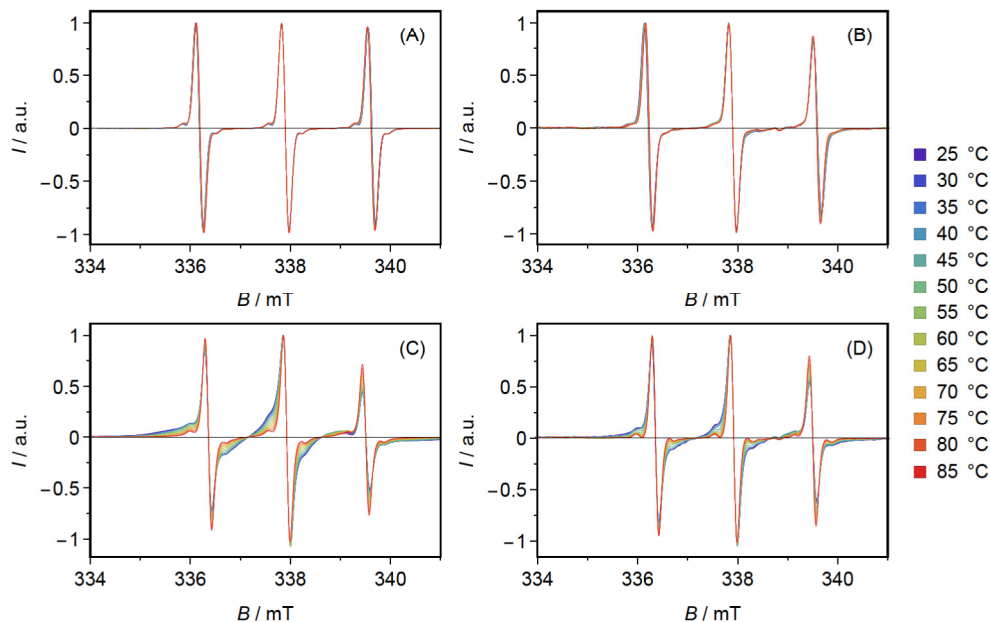


Figure 7.3: Processed EPR spectra of 100 μ M TEMPO (A)/TEMPOL-benzoate (B)/5-DSA (C)/16-DSA (D) in 10 mg/ml DMAm-AAPEAm₇ solution while gradually heating from 25 °C to 85 °C in steps of 5 °C. The raw spectra are shown in fig. 10.91. These were filtered and normalized. Furthermore, the zero crossing of the center field peak was adjusted to the same magnetic field value of the first spectrum (25 °C) in each subfigure. 5-DSA shows the most interaction with the polymer, since the spectra are most broadened in (C) compared to (A), (B) and (D).

A variety of spin probes can be used for researching hydrophobic interactions in aqueous polymer solutions^[193–196]. The spin probe is required to have amphiphilic properties for combination of water-solubility with a hydrophobic group. Furthermore, temperature stability and photostability are necessary.

TEMPO, TEMPOL-benzoate and spin-labeled stearic acid 5-DSA and 16-DSA are mixed with an aqueous solution of 10 mg/ml DMAM-AAPEAm₇. The normalized EPR spectra at different temperatures are depicted in Fig. 7.3. A strong interaction between a spin probe and a hydrophobic makromolecule leads to a reduction in rotational motion of the spin probe. A polymer is much larger and therefore has a lower rotation correlation time τ_c , which is partially adapted by a bound spin probe. This inhibition of motion causes a significant change in the shape of the normalized EPR spectra^[1]. A quick qualitative interpretation can be done by evaluation of the line-broadening. Faster rotation equals sharper signals, which indicates less interaction with the polymer. The normalized EPR spectra of 5-DSA show the largest linewidth, depicted in Fig. 7.3 (C). Therefore, 5-DSA is the spin probe of choice for further EPR measurements.

7.4.2 Light-induced *E-Z* isomerisation at room temperature

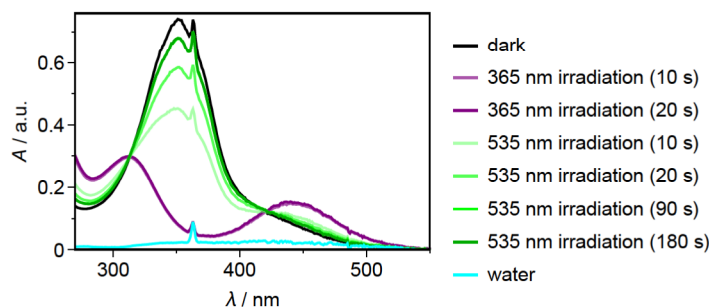


Figure 7.4: UV/vis spectra of 0.02 mg/ml DMAM-AAPEAm_{1.5}. Firstly, the sample was measured in darkness. Then, the sample was irradiated twice for 10 seconds with UV (365 nm) light. Both purple spectra overlap. Lastly, green light (535 nm) irradiation was applied to the sample. Water was used as a background and measured again to varify, that the spike at 360 nm is an artifact from the device and not a signal of the samples.

The *cis*- or *trans*-isomers of AAP photoswitches can be determined by UV/vis-spectroscopy, due to their unique differences in absorption porperties^[197]. UV/vis-spectra of 0.02 mg/ml DMAM-AAPEAm_{1.5} polymer solution are shown in Fig. 7.4. The absorption band of *trans*-AAP has its maximum at approx. 350 nm, which is highest in the spectrum of the initially measured sample with no irradiation applied. After exposure to UV light (365 nm), *trans*-AAP switches to *cis*-AAP and the absorption band at approx. 350 nm disappears. The two newly originated absorption bands are at approx. 320 nm and 440 nm. Green light (535 nm) can be utilized to switch *cis*-AAP back into the *trans*-isomer (Fig. 7.4, green spectra).

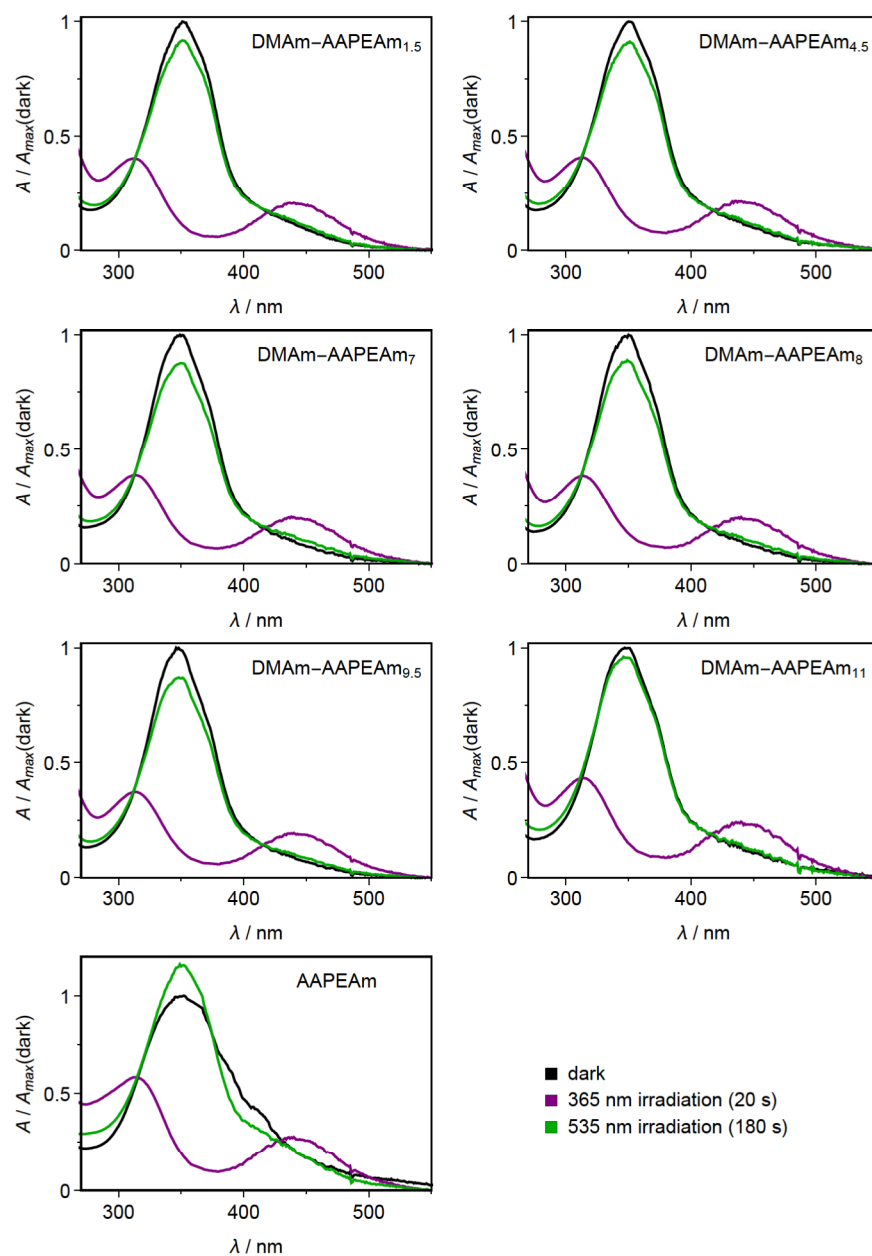


Figure 7.5: UV/vis spectra of DMAm-AAPEAm_x polymers and the AAPEAm monomer. Firstly, the samples were measured in darkness. Then, the samples were irradiated for 20 seconds with UV (365 nm) light. Lastly, green light (535 nm) irradiation was applied for 180 seconds. All spectra are normalized to the maximum absorption of each dark spectrum. The spike at 360 nm, caused by the device, is removed retrospectively. The raw spectra are displayed in Fig. 10.92.

The light-induced *E-Z* isomerisation is almost immediately realised. After at most ten seconds of UV light irradiation, the absorption spectrum of *cis*-AAP is reached (Fig. 7.4, purple spectrum). Due to the low absorbance of *cis*-AAP at wavelengths above 500 nm, the

irradiation time has to be significantly longer to achieve a switch back to *trans*-AAP. After 90 seconds of green light exposure, the final state is achieved. The spectrum, measured after 180 seconds, looks identical, therefore no changes can be observed upon irradiation longer than 90 seconds. However, the final spectrum is not identical with the initially measured 'dark' spectrum. The absorption intensity is slightly lower at 350 nm and higher at 440 nm. This indicates the presence of a small amount of *cis*-AAP within DMAM-AAPEAm_{1.5} even after the light-induced *Z-E* isomerisation, which may be due to a small proportion of blue light emitted by the green LED (see emission spectrum, Fig. 3.3). Although *trans*- and *cis*-AAP have different absorption maxima, branches of each of their absorption bands overlap, which may always lead to small proportion of both states present in the polymer.

The UV/vis spectra of dark, UV-light exposed and green light exposed DMAM-AAPEAm_x polymers are displayed in Fig. 7.5. Since the AAP content varies between different polymers, all spectra of each polymer are normalized to the absorption maximum of the dark spectrum. The behaviour is very alike across all DMAM-AAPEAm_x polymers. A noticeable difference is a higher similarity of the dark and green light-induced *trans*-AAP state in DMAM-AAPEAm₁₁ compared to the other polymers. However, the greatest difference can be found between DMAM-AAPEAm_x polymers and the AAPEAm monomer. AAPEAm seems to have a higher proportion of *cis*-AAP even without additional exposure to irradiation. This is indicated by an increase in intensity of the absorption band at 350 nm when being subjected to green light compared to the initial 'dark' spectrum.

To elaborate on the binding affinity of DMAM-AAPEAm_x polymers towards the hydrophobic spin probe 5-DSA, EPR spectrum simulations with the MATLAB toolbox *EasySpin* was performed^[76,77]. An EPR spectrum consists of all paramagnetic signals within the sample. The EPR spectrum simulations facilitate the reconstruction of the shape of the measured spectrum and enable the abstraction of specific binding parameters. In this case, the spectrum is composed of two different paramagnetic signals. One being the freely rotating 5-DSA molecule, which exhibits no interaction with the polymer, and the other one being a slowly rotating 5-DSA molecule. The latter can be considered as polymer-bound.

DMAM-AAPEAm_x polymer solutions were measured in darkness, during UV light exposure and followed by green light irradiation. The polymer concentration was set to 10 mg/ml, which is sufficiently high to detect noticeable binding affinities towards 100 μ M 5-DSA. The analysis focuses on the change of polymer-bound 5-DSA proportion ($X(5\text{-DSA}_{\text{bound}})$) as well as the rotation correlation time (τ_c) of bound 5-DSA. Fig. 7.6 displays the experimental EPR spectra (black) and the corresponding EPR spectrum simulations (red).

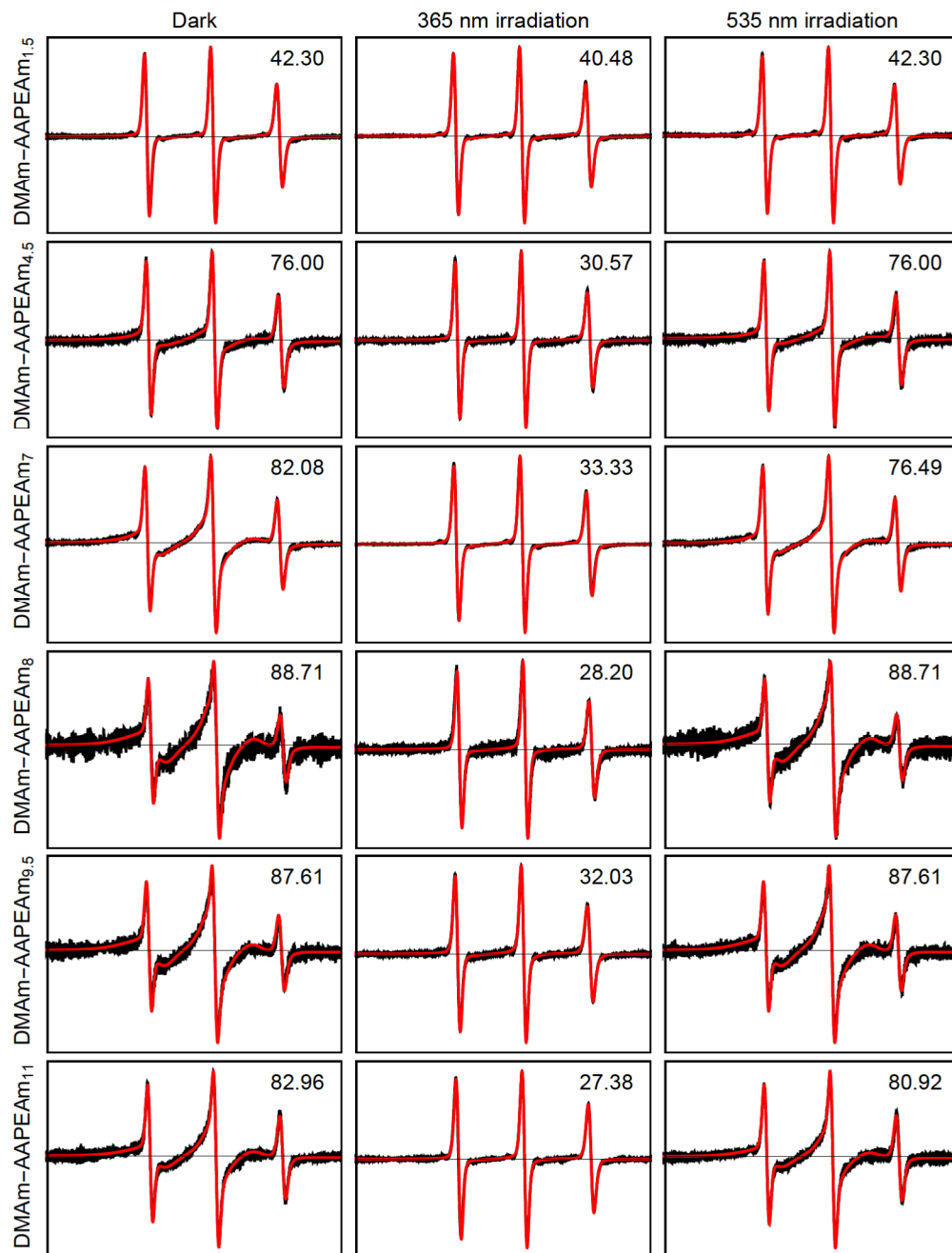


Figure 7.6: EPR spectra (black) and the *EasySpin* EPR spectra simulations (red) before irradiation (dark), during 365 nm irradiation and after 535 nm irradiation of the DMAM-AAPEAm_x polymers ($c = 10$ mg/ml) with 100 μ M 5-DSA. Each simulated spectrum is a combination of two spin systems; one fast rotating nitroxide radical with rotation correlation times τ_c of ≈ 0.05 - 0.2 ns and one slower rotating nitroxide radical with rotation correlation times τ_c of ≈ 2 - 4.5 ns. The motionally inhibited radical species is considered to be polymer-bound 5-DSA and its percentage amount is displayed in the upper right hand corner for each simulated spectrum. The simulation parameters are listed in Tab. 10.2.

The proportion of polymer-bound 5-DSA ($X(5\text{-DSA}_{\text{bound}})$) and its rotation correlation time (τ_c) is dependent on the AAP content (x) inside the DMAM-AAPEAm_x polymers, which is depicted in Fig. 7.7. In the *trans*-state of AAP, the binding capacity of DMAM-AAPEAm_x polymers is higher compared to *cis*-AAP upon UV light exposure. Over 80 % of 5-DSA is bound at the polymer chain for $x < 7\%$. The light-induced *E-Z* isomerisation leads to a reduction in binding capability of the polymer. Depending on the AAP content, $X(5\text{-DSA}_{\text{bound}})$ is reduced to approx. 5-34 %. The bound component's τ_c measures approx. 1.5 to 4.5 ns. During green light irradiation almost all DMAM-AAPEAm_x polymers recover their initial binding capacity. Two outliers are DMAM-AAPEAm₇ and DMAM-AAPEAm₁₁. These polymers have two highest degrees of polymerisation (DP) of 157 and 178. After the release of bound 5-DSA, long polymer chains may change their conformation and inhibit the diffusion of 5-DSA back to possible binding sites. It is noteworthy that the deviations of simulations of irradiated EPR spectra are significantly higher than their dark counterpart. This is due to the higher content of fast rotating spin probe. The sharp signals overshadow the signals of bound 5-DSA, which makes it almost coalesce with the baseline. This impedes an optimal determination of bound content and its exact properties like τ_c .

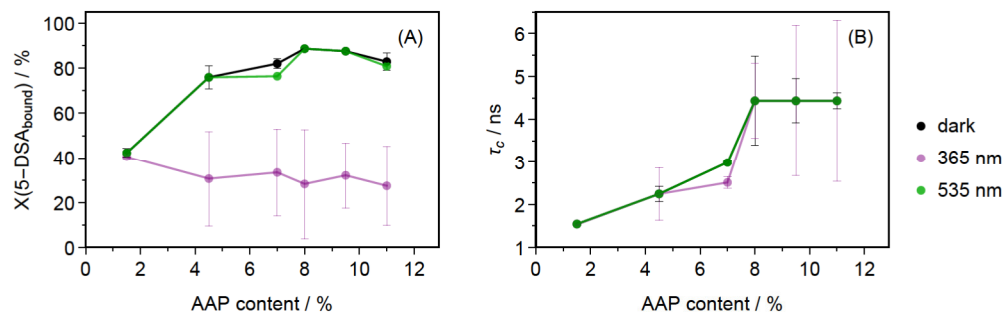


Figure 7.7: The results of the EPR spectrum simulations displayed in Fig. 7.6 are plotted against the AAP content (x) of the DMAM-AAPEAm_x polymers. (A) shows the percentage of polymer-bound 5-DSA ($X(5\text{-DSA}_{\text{bound}})$) and (B) depicts the rotation correlation time τ_c of polymer-bound 5-DSA dependent on x. Error bars are added for the 'dark' and '365 nm' conditions. They represent the standard deviation calculated from values shown here and results from temperature series under identical conditions (25 °C) shown in Fig. 7.10

The monomer AAPEAm was also tested in the same manner as DMAM-AAPEAm_x, shown in Fig. 7.8. Although the light-induced *E-Z* isomerisation was observed in UV/vis spectroscopy, no change in binding affinity could be observed in the presence of 5-DSA. The reasons for that may be twofold. Firstly, the monomer molecules themselves are very small compared to the polymer. An attachment of 5-DSA onto AAPEAm leads to a much lesser motional inhibition, which can be determined by the lower rotation correlation time of 1.3 ns (compared to 2-4.5 ns). Secondly, AAPEAm is less water-soluble than the polymers and 50 vol% of methanol is necessary to achieve the desired concentration

of 10 mg/ml. This less polar solvent mixture reduces the polarity difference between a potentially unpolar AAP group and the surrounding environment, which may also reduce the driving force of binding hydrophobic 5-DSA.

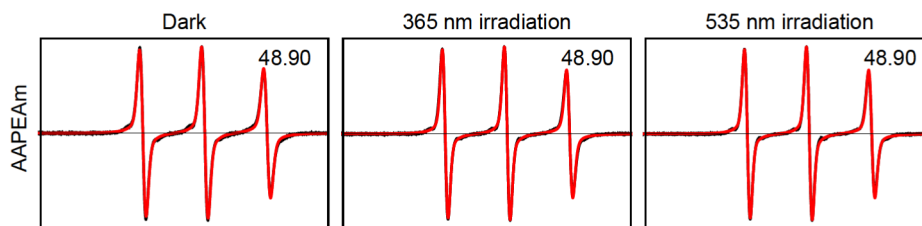


Figure 7.8: EPR spectra (black) and the *EasySpin* EPR spectra simulations (red) before irradiation (dark), during 365 nm irradiation and after 535 nm irradiation of 10 mg/ml AAPEAm monomer with 100 μ M 5-DSA in aqueous MeOH solution (50 vol%). Each simulated spectrum is a combination of two spin systems; one fast rotating nitroxide radical with rotation correlation time $\tau_c = 0.1$ ns and one slower rotating nitroxide radical with a rotation correlation time $\tau_c = 1.3$ ns. The motionally inhibited radical species is considered to be AAPEAm-bound 5-DSA and its percentage is displayed in the upper right hand corner for each simulated spectrum. The simulation parameters do not change during this experiment with $g_{iso}(bound) = g_{iso}(free) = 2.00465$, $A_{iso}(bound) = 40.76$ and $A_{iso}(free) = 42.28$.

7.4.3 Temperature-dependent light-induced *E-Z* isomerisation

The DMAm-AAPEAm_x polymers exhibit a phase transition temperature between 20 and 80 °C^[191]. This cloudpoint temperature is influenced by the amount of AAP in the polymer and its *cis*- or *trans*-form. A temperature series (10-75 °C) of each 10 mg/ml DMAm-AAPEAm_x polymer solution with 100 μ M 5-DSA can be measured via EPR spectroscopy during darkness as well as UV light exposure to investigate the binding affinity of these polymers during phase transition.

Such a temperature series with experimental and simulated spectra is depicted in Fig. 7.9 for non-irradiated DMAm-AAPEAm₇. The UV light-exposed temperature series as well as the same measurements and simulations for all other polymers and the AAPEAm monomer are listed in the appendix in Fig. 10.93-10.105.

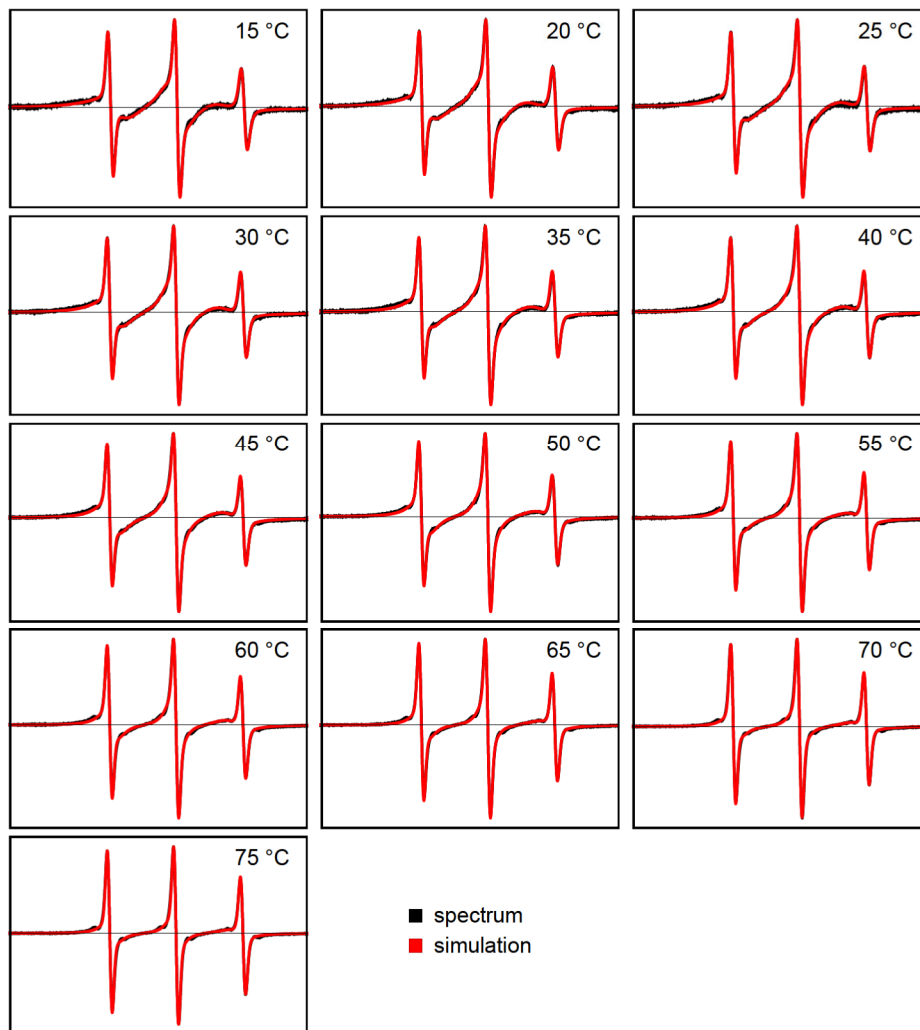


Figure 7.9: EPR spectra (black) and the *EasySpin* EPR spectrum simulations (red) of 10 mg/ml DMAM-AAPEAm₇ with 100 μ M 5-DSA recorded in darkness and at different temperatures. Each simulated spectrum is a combination of two spin systems; one fast rotating nitroxide radical with rotation correlation times τ_c of ≈ 0.05 -0.2 ns and one slower rotating nitroxide radical with rotation correlation times τ_c of ≈ 1.5 -3 ns. The simulation parameters are listed in Tab. 10.7.

From these simulations $X(5\text{-DSA}_{\text{bound}})$ is obtained and plotted against the temperature. It is shown in Fig. 7.10 (A) for all dark temperature series and (B) during UV irradiation. Similar to the results in the previous chapter, DMAM-AAPEAm_x polymers show a maximum of 5-DSA binding (80-90%) at AAP contents above 7% and at temperatures between 15-45 °C. Above 45 °C, the binding capacities seem to slightly decrease with higher temperatures, which may be due to the elevated kinetic energies of the 5-DSA and polymer molecules. The average binding capacity of dark DMAM-AAPEAm_{4.5} and DMAM-AAPEAm_{1.5} are approx. 70% and 45%, respectively, which shows a correlation of binding capacity and AAP content up to the saturation above 7%.

During UV irradiation (Fig. 7.10 (B)), the data does not produce such a clear picture at first glance. Except for DMAM-AAPEAm_{1.5}, all samples seem to exhibit a similar temperature-dependent decrease in binding capacity but the data appears to be disordered with a view on AAP content. However, this is not a coincidence. The average proportion of polymer-bound 5-DSA is calculated for each irradiated temperature series and subtracted from the average proportion of polymer-bound 5-DSA during each dark temperature series to yield the average difference of proportion of polymer-bound 5-DSA for each DMAM-AAPEAm_x polymer and AAPEAm monomer. This is depicted in Fig. 7.11. It clearly displays the dependency on AAP content and the differences in binding capacity between *trans*- and *cis*-isomers in DMAM-AAPEAm_x polymers.

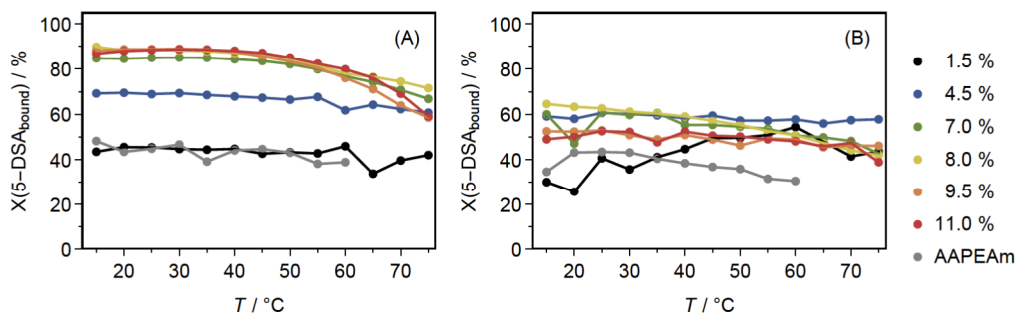


Figure 7.10: The percentage of polymer-bound 5-DSA ($X(5\text{-DSA}_{\text{bound}})$) at different temperatures in darkness (A) and during irradiation with UV (365 nm) light (B). The legend displays the AAP content (x) of the DMAM-AAPEAm_x polymers and the monomer AAPEAm. All data was obtained from *EasySpin* EPR spectrum simulations shown in Fig. 7.9 and Fig. 10.93-10.105.

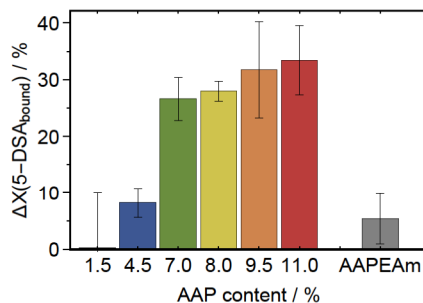


Figure 7.11: The average difference of proportion of polymer-bound 5-DSA ($X(5\text{-DSA}_{\text{bound}})$) between dark and irradiated conditions shown in Fig. 7.10.

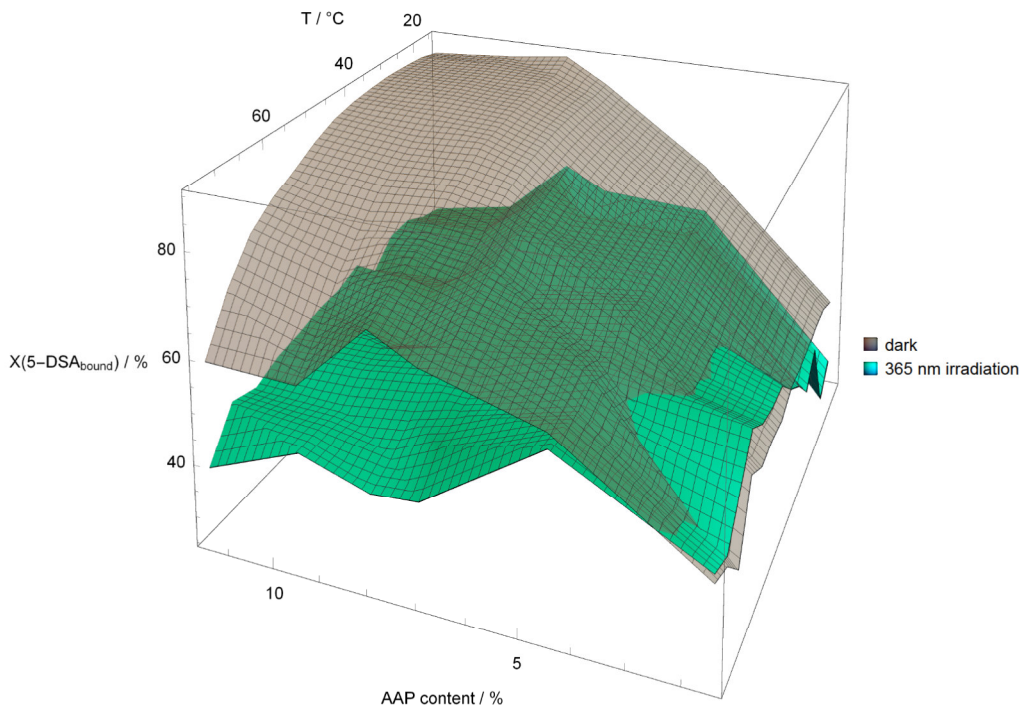


Figure 7.12: Fig. 7.10 (A) and (B) can be combined to one three-dimensional plot. The percentage of polymer-bound 5-DSA ($X(5\text{-DSA}_{\text{bound}})$, z-axis) is dependent on the AAP content of the DMAm-AAPEAm_x polymers (x-axis) and the temperature (T , y-axis). Two planes span all information for comparing dark (gray) and irradiated (cyan) photoresponsive polymers. The two planes overlap at low proportions of AAP content. The binding of 5-DSA increases with rising AAP content up to 88 % of polymer-bound 5-DSA under dark conditions at $T = 20\text{-}40\text{ }^{\circ}\text{C}$. At higher temperatures above $40\text{ }^{\circ}\text{C}$ the interaction between 5-DSA and DMAm-AAPEAm_x polymers is reduced under dark conditions. During irradiation, the higher temperatures do not have such a significant impact on $X(5\text{-DSA}_{\text{bound}})$.

In summary, the binding capacity of DMAm-AAPEAm_x polymers is influenced by the temperature and the AAP content within the polymer as well as its *cis-trans*-isomerism, which can be switched via UV light (*E-Z* isomerisation) or green light (*Z-E* isomerisation) irradiation. This is again depicted in the synoptic three-dimensional Fig. 7.12. The phase transition temperatures of DMAm-AAPEAm_x polymers^[191] have no observable effect on the binding capacity towards the hydrophobic model compound 5-DSA. This enables the design of photoresponsive AAPEAm-containing polymers with independent phase transition and binding properties.

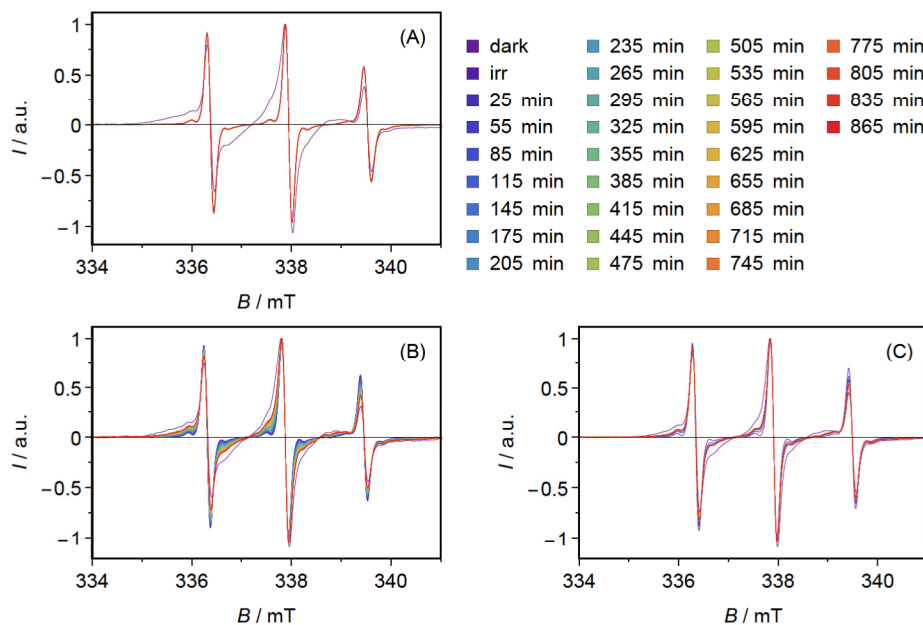
7.4.4 Temperature-dependent relaxation after *E*–*Z* photoisomerisation

Figure 7.13: Normalized EPR spectra of 10 mg/ml DMAm-AAPEAm₇ with 100 μ M 5-DSA at 25 °C (A), 45 °C (B) and 65 °C (C). The first and broadest EPR spectrum was recorded in the dark. Afterwards, the sample was irradiated (365 nm) during the acquisition of the second spectrum 'irr'. To monitor possible *cis*-*trans*-relaxation, spectra were collected during 865 min of darkness after irradiation (see legend). The raw EPR spectra are shown in Fig. 10.106.

Since the *trans*-isomer of the AAP photoswitches is the initial state in DMAm-AAPEAm_x polymers when preparing a polymer solution, it can be presumed thermodynamically favoured. Consequentially, a relaxation from *cis* to *trans* inside the polymer chain is conceivable.

Fig. 7.13 shows EPR spectra of 10 mg/ml DMAm-AAPEAm₇ with 100 μ M 5-DSA at 25 °C (A), 45 °C (B) and 65 °C (C). After UV irradiation, multiple EPR spectra were collected every 30 minutes over a total duration of 14 hours. The change of the spectral shape can be compared to the dark spectrum, which was measured first. During the observed time span, none of the three samples exhibit the recreation of the initial dark state. At 25 °C, the sample seems to fully remain in its irradiated state even when the UV light is switched off for hours. Weston *et al.* (2014)^[183] reported a half-life of 10 days for *Z*-1,3,5-trimethyl-4-(phenyldiazenyl)-1H-pyrazole, which is the N-methyl-substituted photoswitch, similar to the N-ethyl-substituted photoswitch used in this chapter. At 45 °C, spectra broaden over time during the first approx. twelve hours until they reach a stable state between 'dark' and 'irradiated'. A blend of *cis*- and *trans*-AAP inside the polymer chain is likely to exist. A similar behaviour can be seen in Fig. 7.13 (C). However, the stable mix of *cis*- and *trans*-AAP is reached much faster, during the first two

hours. Furthermore, the interactions between DMAm-AAPEAm₇ and 5-DSA are weaker indicated by a less broadened spectrum at 65 °C.

The following factors may merge into a full explanation of these observations. At room temperature the kinetic energy of the AAP photoswitches is not high enough to switch back from *cis* to *trans* state without green light irradiation. Higher temperatures lead to a reconstruction of the strong interactions between DMAm-AAPEAm₇ and 5-DSA, which may be due to an increase in the amount of *trans*-AAP. The temperature itself determines the final ratio of *cis*- and *trans*-AAP. It seems that with higher temperature the stable mix of *cis*- and *trans*-AAP is reached faster and the proportion is shifted towards more *cis*-AAP.

7.5 Conclusion

The setup for fiber-coupled LED irradiation within the MS5000 Benchtop EPR spectrometer is well suitable for the investigation of photoresponsive polymers. EPR spectrum simulations can be utilized to gather profound insights into the binding properties of DMAm-AAPEAm_x polymers towards a hydrophobic spin-labeled model compound like 5-DSA.

The AAP photoswitches have the capability of light-induced *E-Z* isomerisation, which changes their dipole moment^[198]. Built into a polymer chain, the AAP content determines the phase transition temperature of these LCST polymers^[191] as well as the binding affinity towards 5-DSA. The UV light-induced *E-Z* isomerisation triggers a release of bound 5-DSA, whose quantity is proportionate to the AAP content. This will also increase the phase transition temperature^[191]. Green light-induced *Z-E* isomerisation leads to a complete rebinding of 5-DSA, which may just be slightly impaired by long polymer chains (DP>157).

AAP content above 7 % will lead to a further decrease of the cloudpoint temperature^[191] but does not increase the binding capacity of these polymers. Moreover, the interaction between DMAm-AAPEAm_x and 5-DSA is not impacted by the phase transition. These two facts may allow for a partially independent polymer design for binding properties and phase transition. Future studies might also investigate the binding of other molecules of interest and variation of the non-photoswitchable polymer backbone. Moreover, modification of the AAP moieties to red-shift the absorption bands would enhance the possibility of in vivo use as a drug delivery system^[181].

8 Conclusion

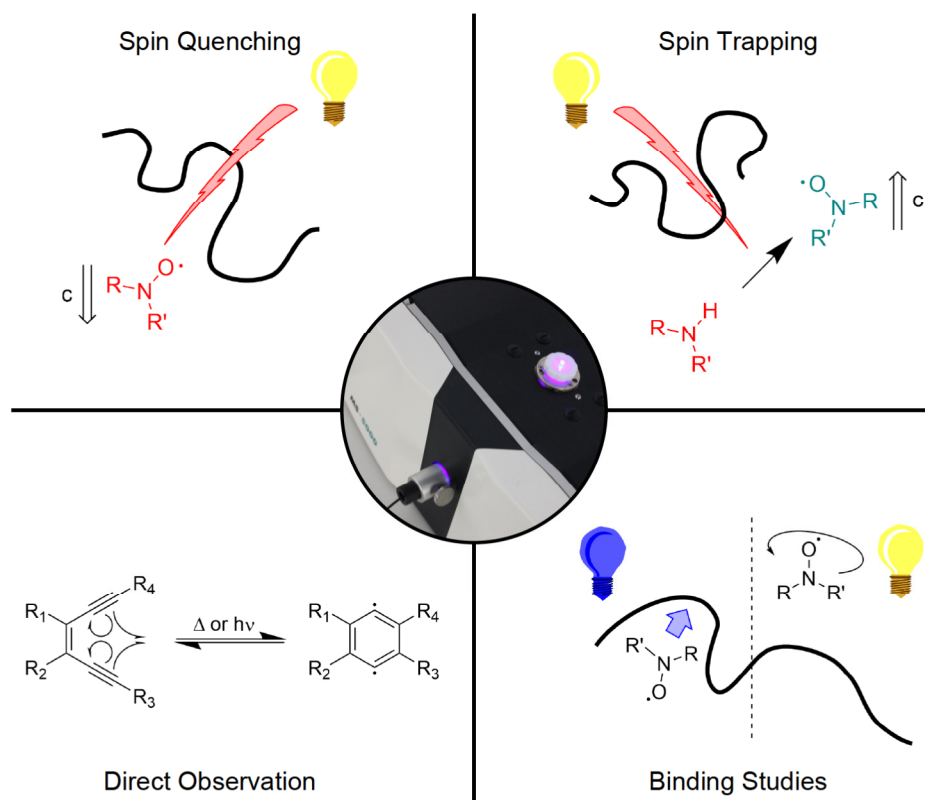


Figure 8.1: Schematic representation of possible applications enabled by the fiber-coupled LED irradiation within the MS5000 Benchtop EPR spectrometer. In the center is a picture of the EPR spectrometer during irradiation. The thick black curvy lines are illustrations of a makromolecule like a mAb or a polymer. In the upper left hand corner, 'Spin Quenching' portrays the utilization of a stable spin probe like a nitroxide radical for quantification of a photodegradation process. The irradiation of a makromolecule of interest (mAb in chapter 4, polysorbate in chapter 5, EDY-containing polymers in chapter 6) leads to a detectable decrease in radical concentration upon reacting with photochemically generated reactive species. The opposite approach is displayed in the upper right hand corner, where a diamagnetic species scavenges reactive photodegradation products and is subsequently converted to a paramagnetic species with increasing concentration during irradiation. Such a 'Spin Trapping' experiment is discussed in chapter 5. Moreover, a 'Direct Observation' of photochemical radical generation is possible (chapter 6) and depicted in the bottom left hand corner. Finally, 'Binding Studies' of a spin probe-polymer mixture is feasible with EPR spectroscopy. The irradiation-coupled EPR spectrometer setup enables such studies upon photoresponsive polymers, which may behave differently during light-exposure and in darkness. This is represented in the bottom right hand corner and discussed in chapter 7.

8 Conclusion

In this thesis, the setup and application of a fiber-coupled LED irradiation within the MS5000 Benchtop EPR spectrometer is explored. It combines the advantages of detecting radical signals in an irradiated environment. Furthermore, irradiating over a long period of time is not limited by anything like the sample volume as it would be if samples are taken from a light exposed bulk solution. Additionally, possible variations caused by sample collection are non-existent. Approaches of investigation are schematically concluded in Fig. 8.1.

A direct observation of photochemically generated radicals via Bergman cyclisation is shown in chapter 6. The incorporation of EDY in the main-chain of polymers^[38] enables fine-tuning of parameters like stability and reactivity of both the EDY group and the eventually generated radicals. The non-EDY-components inside the polymer main-chain have a significant impact, since they determine the flexibility of the polymer chain and the distance between EDY groups, as well as the stereoelectronic influence on the EDY group. Furthermore, groups with abstractable hydrogen atoms in the polymer chain may serve as an intramolecular reactant towards the generated σ -radicals.

Slow photodegradation processes or the observation of radicals with a short lifetime have to be investigated indirectly. This can be done by scavenging reactive photochemically generated radical species. Such a scavenger molecule can be either diamagnetic and subsequently convert to a paramagnetic species or vice versa, leading to an increase or decrease of EPR signal, respectively. The stable radical TEMPOL is used as a spin probe in chapter 4, 5 and 6. Its decay in various mAb + buffer solutions is able to give hints on the nature of a protein-bound photosensitizing species like iron(III)^[108,110,113] (chapter 4). In chapter 6, TEMPOL is used to mimic a DNA cleavage experiment of EDY-containing polymers. Moreover, photodegradation of polysorbate 20 and 80 in different grades of purity is investigated (chapter 5). Polysorbate 80SR is least prone to degradation from irradiation. Furthermore, the addition of another selective quencher such as sodium azide enables qualitative determination of photochemically generated reactive species. A radical generating experiment is also demonstrated via irradiation of polysorbate with TMP.

Due to the detailed information about rotational motion of a spin system embedded in EPR spectra^[1], spectrum simulations can be utilized to gather insights in the binding properties of DMAM-AAPEAm_x polymers^[191] towards a hydrophobic spin-labeled model compound like 5-DSA (chapter 7). These polymers have photoresponsive aryl azopyrazole groups, which are capable of changing their dipole moment via light-induced *E-Z* isomerisation. This impacts the binding capacity towards 5-DSA, which is higher in the *trans*-form and lower in the *cis*-form of the photoswitch. The amount of repulsion of bound spin probe is correlated to the content of photoswitches in the polymer chain. This research may lay the foundation of light-controlled drug delivery.

In conclusion, the possible applications for fiber-coupled LED irradiation within an EPR spectrometer are manifold. This thesis can be used as a blueprint for extending an EPR

8 *Conclusion*

spectrometer with an irradiation source. The only requirement is an opening inside the resonator for the insertion of an optical fiber cable.

8 *Conclusion*

9 References

- [1] V. Chechik, E. Carter, D. Murphy, *Electron Paramagnetic Resonance (Oxford Chemistry Primers)*, Oxford University Press, USA, **2016**.
- [2] A. J. Hoff, *Advanced EPR: applications in biology and biochemistry*, Elsevier, **2012**.
- [3] H. M. Swartz, N. Khan, J. Buckey, R. Comi, L. Gould, O. Grinberg, A. Hartford, H. Hopf, H. Hou, E. Hug, et al., *NMR in Biomedicine* **2004**, *17*, 335–351.
- [4] M. Hunger, J. Weitkamp, *Angewandte Chemie International Edition* **2001**, *40*, 2954–2971.
- [5] S. Van Doorslaer, D. M. Murphy, *EPR Spectroscopy: Applications in Chemistry and Biology* **2012**, 1–39.
- [6] A. Lund, M. Shiotani, *Applications of EPR in radiation research*, Springer, **2014**.
- [7] D. Hinderberger, *EPR Spectroscopy: Applications in Chemistry and Biology* **2012**, 67–89.
- [8] B. Schweitzer-Chaput, M. A. Horwitz, E. de Pedro Beato, P. Melchiorre, *Nature chemistry* **2019**, *11*, 129–135.
- [9] L. Chang, Q. An, L. Duan, K. Feng, Z. Zuo, *Chemical Reviews* **2021**, *122*, 2429–2486.
- [10] S. Sharma, A. P. Pandey, A. Sharma, *Advanced Synthesis & Catalysis* **2020**, *362*, 5196–5218.
- [11] R. Ameta, A. K. Chohadia, A. Jain, P. B. Punjabi in *Advanced oxidation processes for waste water treatment*, Elsevier, **2018**, pp. 49–87.
- [12] L. Clarizia, D. Russo, I Di Somma, R. Marotta, R. Andreozzi, *Applied Catalysis B: Environmental* **2017**, *209*, 358–371.
- [13] I. V. Alabugin, W.-Y. Yang, R. Pal in *CRC Handbook of Organic Photochemistry and Photobiology, Third Edition-Two Volume Set*, CRC Press, **2019**, pp. 549–592.
- [14] Y. Xiao, A. Hu, *Macromolecular rapid communications* **2011**, *32*, 1688–1698.
- [15] P. Klán, J. Wirz, *Photochemistry of Organic Compounds - From Concepts to Practice*, John Wiley & Sons, New York, **2009**.
- [16] M. A. Uddin, H. Yu, L. Wang, K.-u.-R. Naveed, F. Haq, B. U. Amin, S. Mehmood, A. Nazir, Y. Xing, D. Shen, *Journal of Polymer Science* **2020**, *58*, 1924–1948.

- [17] C. F. Chignell, A. G. Motten, R. H. Sik, C. E. Parker, K. Reszka, *Photochemistry and photobiology* **1994**, *59*, 5–11.
- [18] A. Staško, K. Szaboova, V. Cholvad, O. Nuyken, J. Dauth, *Journal of Photochemistry and Photobiology A: Chemistry* **1993**, *69*, 295–304.
- [19] Bruker Announces Acquisition of MagneTech’s EPR Business, <https://www.bruker.com/en/news-and-events/news/2019/bruker-announces-acquisition-of-magnetechs-epr-business.html>, Accessed: 2024-03-11.
- [20] MagneTech ESR5000, <https://www.bruker.com/de/products-and-solutions/mr/epr-instruments/magnetechesr5000.html>, Accessed: 2024-03-11.
- [21] M. Borregón, K. Martínez, A. Ramos, I. Ramos, B. Berzal, M. Mazariegos, E. Martínez, T. Hernández, B. Doger, V. Moreno, *Cancer Chemotherapy and Pharmacology* **2022**, *89*, 577–584.
- [22] M. J. McConnell, *Drug Discovery Today* **2019**, *24*, 1132–1138.
- [23] E. Hipper, M. Blech, D. Hinderberger, P. Garidel, W. Kaiser, *Pharmaceutics* **2021**, *14*, 72.
- [24] E. Hipper, F. Lehmann, W. Kaiser, G. Hübner, J. Buske, M. Blech, D. Hinderberger, P. Garidel, *International Journal of Pharmaceutics: X* **2022**, 100155.
- [25] W. Kaiser, T. Schultz-Fademrecht, M. Blech, J. Buske, P. Garidel, *International Journal of Pharmaceutics* **2021**, *604*, 120723.
- [26] A. Sreedhara, J. Yin, M. Joyce, K. Lau, A. T. Wecksler, G. Deperalta, L. Yi, Y. J. Wang, B. Kabakoff, R. S. Kishore, *European Journal of Pharmaceutics and Biopharmaceutics* **2016**, *100*, 38–46.
- [27] C. Schöneich, *Pharmaceutical Research* **2020**, *37*, DOI 10.1007/s11095-020-2763-8.
- [28] M. T. Jones, H.-C. Mahler, S. Yadav, D. Bindra, V. Corvari, R. M. Fesinmeyer, K. Gupta, A. M. Harmon, K. D. Hinds, A. Koulov, W. Liu, K. Maloney, J. Wang, P. Y. Yeh, S. K. Singh, *Pharmaceutical Research* **2018**, *35*, DOI 10.1007/s11095-018-2430-5.
- [29] S. Dahotre, A. Tomlinson, B. Lin, S. Yadav, *Journal of Pharmaceutical and Biomedical Analysis* **2018**, *157*, 201–207.
- [30] V. Corvari, L. O. Narhi, T. M. Spitznagel, N. Afonina, S. Cao, P. Cash, I. Cecchini, M. R. DeFelippis, P. Garidel, A. Herre, A. V. Koulov, T. Lubiniecki, H.-C. Mahler, P. Mangiagalli, D. Nesta, B. Perez-Ramirez, A. Polozova, M. Rossi, R. Schmidt, R. Simler, S. Singh, A. Weiskopf, K. Wuchner, *Biologicals* **2015**, *43*, 457–473.

- [31] L. O. Narhi, D. K. Chou, T. R. Christian, S. Gibson, B. Jagannathan, W. Jiskoot, S. Jordan, A. Sreedhara, L. Waxman, T. K. Das, *Journal of Pharmaceutical Sciences* **2022**, *111*, 887–902.
- [32] S. R. Singh, J. Zhang, C. O'Dell, M.-C. Hsieh, J. Goldstein, J. Liu, A. Srivastava, *AAPS PharmSciTech* **2012**, *13*, 422–430.
- [33] M. Agarkhed, C. O'Dell, M.-C. Hsieh, J. Zhang, J. Goldstein, A. Srivastava, *AAPS PharmSciTech* **2012**, *14*, 1–9.
- [34] K. C. Nicolaou, W. Dai, *Angewandte Chemie International Edition in English* **1991**, *30*, 1387–1416.
- [35] K. C. Nicolaou, A. L. Smith, E. W. Yue, *Proceedings of the National Academy of Sciences* **1993**, *90*, 5881–5888.
- [36] A. L. Smith, K. C. Nicolaou, *Journal of Medicinal Chemistry* **1996**, *39*, 2103–2117.
- [37] S. Van Lanen, B. Shen, *Current Topics in Medicinal Chemistry* **2008**, *8*, 448–459.
- [38] Y. Cai, F. Lehmann, E. Peiter, S. Chen, J. Zhu, D. Hinderberger, W. H. Binder, *Polymer Chemistry* **2022**, *13*, 3412–3421.
- [39] D. Kungwachakun, M. Irie, *Die Makromolekulare Chemie Rapid Communications* **1988**, *9*, 243–246.
- [40] M. Russew, S. Hecht, *Advanced Materials* **2010**, *22*, 3348–3360.
- [41] J. Boelke, S. Hecht, *Advanced Optical Materials* **2019**, *7*, DOI 10.1002/adom.201900404.
- [42] A. Laschewsky, E. D. Rekaï, *Macromolecular Rapid Communications* **2000**, *21*, 937–940.
- [43] V. M. Martín Giménez, G. Arya, I. A. Zucchi, M. J. Galante, W. Manucha, *Soft Matter* **2021**, *17*, 8577–8584.
- [44] M. Fernández, J. Orozco, *Polymers* **2021**, *13*, 2464.
- [45] W. Zhao, Y. Zhao, Q. Wang, T. Liu, J. Sun, R. Zhang, *Small* **2019**, *15*, DOI 10.1002/smll.201903060.
- [46] F. Gerson, W. Huber, *Electron Spin Resonance Spectroscopy of Organic Radicals*, Wiley, **2003**.
- [47] W. Pauli, *Naturwiss* **1924**, *12*, 741.
- [48] G. Wedler, *Lehrbuch der physikalischen Chemie*, Wiley-VCH, **2004**.
- [49] M. M. Roessler, E. Salvadori, *Chemical Society Reviews* **2018**, *47*, 2534–2553.
- [50] N. Atherton, *Chemical Society Reviews* **1993**, *22*, 293–298.
- [51] S Goudsmit, R. Bacher, *Physical Review* **1929**, *34*, 1501.

- [52] S Goudsmit, *Physical Review* **1931**, *37*, 663.
- [53] M. G. Shenkar, B. Rananavare, J. H. Freed, *Biochimica et Biophysica Acta (BBA) - General Subjects* **1990**, *1036*, 228–236.
- [54] M. A. Uddin, H. Yu, L. Wang, K. Naveed, F. Haq, B. U. Amin, S. Mehmood, A. Nazir, Y. Xing, D. Shen, *Journal of Polymer Science* **2020**, *58*, 1924–1948.
- [55] W. Dunham, R. Sands, S. Klein, E. Duell, L. Rhodes, C. Marcelo, *Spectrochimica Acta Part A: Molecular and Biomolecular Spectroscopy* **1996**, *52*, 1357–1368.
- [56] M. G. Bakker, B. Fowler, M. K. Bowman, G. S. Patience, *The Canadian Journal of Chemical Engineering* **2020**, *98*, 1668–1681.
- [57] M. J. Junk, H. W. Spiess, D. Hinderberger, *Journal of Magnetic Resonance* **2011**, *210*, 210–217.
- [58] C. Varano Casasanta, *Microscopy Today* **2022**, *30*, 46–46.
- [59] K. F. Lim, *Journal of Chemical Education* **2005**, *82*, 145.
- [60] D. F. Swinehart, *Journal of Chemical Education* **1962**, *39*, 333.
- [61] W. Heisenberg, *Zeitschrift für Physik* **1927**, *43*, 172–198.
- [62] L. G. Weyer, *Applied Spectroscopy Reviews* **1985**, *21*, 1–43.
- [63] C. M. Marian, *WIREs Computational Molecular Science* **2011**, *2*, 187–203.
- [64] In *The IUPAC Compendium of Chemical Terminology*, International Union of Pure and Applied Chemistry (IUPAC), **2014**.
- [65] T. Förster, *Radiation Research Supplement* **1960**, *2*, 326.
- [66] R. M. Clegg in *Laboratory Techniques in Biochemistry and Molecular Biology*, Elsevier, **2009**, 1–57.
- [67] J. W. Verhoeven, *Pure and Applied Chemistry* **1996**, *68*, 2223–2286.
- [68] D. L. Dexter, *The Journal of Chemical Physics* **1953**, *21*, 836–850.
- [69] E. Reijerse, A. Savitsky, *EPR Spectroscopy: Fundamentals and Methods* **2018**, 235.
- [70] M. Hruszowiec, K. Nowak, B. Szlachetko, M. P. Grzelczak, W. Czarczyński, E. F. Pliński, T. Więckowski, *Journal of Telecommunications and Information Technology* **2017**, 18–25.
- [71] N. R. Council et al., *Microwave processing of materials, Vol. 473*, National Academies Press, **1994**.
- [72] K. Kishore, S. A. Akbar, *IEEE Sensors Journal* **2020**, *20*, 10345–10354.
- [73] *In Vivo EPR (ESR)*, (Ed.: L. J. Berliner), Springer US, **2003**.
- [74] G. R. Eaton, S. S. Eaton, D. P. Barr, R. T. Weber in *Quantitative EPR*, Springer Vienna, **2010**, pp. 63–67.

- [75] A. I. Lvovsky in *Encyclopedia of Optical and Photonic Engineering (Print)-Five Volume Set*, CRC Press, **2015**, pp. 1–6.
- [76] S. Stoll, A. Schweiger, *Journal of Magnetic Resonance* **2006**, *178*, 42–55.
- [77] EasySpin, <http://easyspin.org/>, Accessed: 2024-03-11.
- [78] J. Lehner, S. Stoll, *The Journal of Chemical Physics* **2020**, *152*, DOI 10.1063/1.5139935.
- [79] T. Hauenschild, J. Reichenwallner, V. Enkelmann, D. Hinderberger, *Chemistry – A European Journal* **2016**, *22*, 12825–12838.
- [80] S. H. Arabi, B. Aghelnejad, C. Schwieger, A. Meister, A. Kerth, D. Hinderberger, *Biomaterials Science* **2018**, *6*, 478–492.
- [81] D. L. Marshall, M. L. Christian, G. Gryn’ova, M. L. Coote, P. J. Barker, S. J. Blanksby, *Organic & Biomolecular Chemistry* **2011**, *9*, 4936.
- [82] D. R. Davies, S. Chacko, *Accounts of chemical research* **1993**, *26*, 421–427.
- [83] M. L. Chiu, D. R. Goulet, A. Teplyakov, G. L. Gilliland, *Antibodies* **2019**, *8*, 55.
- [84] M. S. Castelli, P. McGonigle, P. J. Hornby, *Pharmacology Research & Perspectives* **2019**, *7*, DOI 10.1002/prp2.535.
- [85] M. Berger, V. Shankar, A. Vafai, *The American Journal of the Medical Sciences* **2002**, *324*, 14–30.
- [86] C. Schöneich, *International Journal of Molecular Sciences* **2022**, *23*, DOI 10.3390/ijms23158262.
- [87] P. Atkins, J. Paula, *Atkins’ physical chemistry*, Oxford University press, **2008**.
- [88] M. S. Baptista, J. Cadet, P. Di Mascio, A. A. Ghogare, A. Greer, M. R. Hamblin, C. Lorente, S. C. Nunez, M. S. Ribeiro, A. H. Thomas, M. Vignoni, T. M. Yoshimura, *Photochemistry and Photobiology* **2017**, *93*, 912–919.
- [89] C. Schweitzer, R. Schmidt, *Chemical Reviews* **2003**, *103*, 1685–1758.
- [90] M. Klaper, W. Fudickar, T. Linker, *Journal of the American Chemical Society* **2016**, *138*, 7024–7029.
- [91] Y. H. Tan, M. Liu, B. Nolting, J. G. Go, J. Gervay-Hague, G.-y. Liu, *ACS Nano* **2008**, *2*, 2374–2384.
- [92] P. Garidel, A. B. Kuhn, L. V. Schäfer, A. R. Karow-Zwick, M. Blech, *European Journal of Pharmaceutics and Biopharmaceutics* **2017**, *119*, 353–360.
- [93] J. Li, M. Jiang, H. Zhou, P. Jin, K. M. C. Cheung, P. K. Chu, K. W. K. Yeung, *Global Challenges* **2018**, *3*, DOI 10.1002/gch2.201800058.
- [94] L. Chen, L. Wang, Y. Wan, Y. Zhang, Z. Qi, X. Wu, H. Xu, *Advanced Materials* **2019**, *32*, DOI 10.1002/adma.201904433.

9 References

- [95] Y. Zhang, C. Schöneich, *Molecular Pharmaceutics* **2022**, *20*, 650–662.
- [96] L. Augenstein, J. Nag-Chaudhuri, *Nature* **1964**, *203*, 1145–1147.
- [97] A. J. P. Teunissen, C. Pérez-Medina, A. Meijerink, W. J. M. Mulder, *Chemical Society Reviews* **2018**, *47*, 7027–7044.
- [98] P. R. Erickson, K. J. Moor, J. J. Werner, D. E. Latch, W. A. Arnold, K. McNeill, *Environmental Science & Technology* **2018**, *52*, 9170–9178.
- [99] M. I. Gutiérrez, S. M. Fernández, W. A. Massad, N. A. García, *Redox Report* **2006**, *11*, 153–158.
- [100] E. Sikorska, I. Khmelinskii, A. Komasa, J. Koput, L. F. Ferreira, J. R. Herance, J. L. Bourdelande, S. L. Williams, D. R. Worrall, M. Insińska-Rak, M. Sikorski, *Chemical Physics* **2005**, *314*, 239–247.
- [101] A. Albini, *Photochem. Photobiol. Sci.* **2016**, *15*, 319–324.
- [102] R. Kehm, T. Baldensperger, J. Raupbach, A. Höhn, *Redox Biology* **2021**, *42*, 101901.
- [103] R. Torosantucci, C. Schöneich, W. Jiskoot, *Pharmaceutical Research* **2013**, *31*, 541–553.
- [104] D. A. Dougherty, *Science* **1996**, *271*, 163–168.
- [105] D. A. Dougherty, *Accounts of Chemical Research* **2012**, *46*, 885–893.
- [106] L. J. Juszczak, A. S. Eisenberg, *Journal of the American Chemical Society* **2017**, *139*, 8302–8311.
- [107] J. P. Gallivan, D. A. Dougherty, *Proceedings of the National Academy of Sciences* **1999**, *96*, 9459–9464.
- [108] Y. Zhang, D. S. Richards, E. N. Grotemeyer, T. A. Jackson, C. Schöneich, *Molecular Pharmaceutics* **2022**, *19*, 4026–4042.
- [109] Y. Li, A. Polozova, F. Gruia, J. Feng, *Analytical Chemistry* **2014**, *86*, 6850–6857.
- [110] Y. Zhang, C. Schöneich, *European Journal of Pharmaceutics and Biopharmaceutics* **2023**, *190*, 231–241.
- [111] E. Illés, S. G. Patra, V. Marks, A. Mizrahi, D. Meyerstein, *Journal of Inorganic Biochemistry* **2020**, *206*, 111018.
- [112] C. J. Miller, A. L. Rose, T. D. Waite, *Frontiers in Marine Science* **2016**, *3*, DOI 10.3389/fmars.2016.00134.
- [113] Y. Zhang, M. E. Ballesteros, C. Schöneich, *European Journal of Pharmaceutics and Biopharmaceutics* **2023**, *190*, 121–130.
- [114] M. J. Davies, *Methods* **2016**, *109*, 21–30.

9 References

- [115] N. Khan, C. M. Wilmot, G. M. Rosen, E. Demidenko, J. Sun, J. Joseph, J. O'Hara, B. Kalyanaraman, H. M. Swartz, *Free Radical Biology and Medicine* **2003**, *34*, 1473–1481.
- [116] I. Prajapati, N. R. Larson, S. Choudhary, C. Kalonia, S. Hudak, R. Esfandiary, C. R. Middaugh, C. Schöneich, *Molecular Pharmaceutics* **2021**, *18*, 3223–3234.
- [117] Y.-T. Zhu, Y.-Z. Yuan, Q.-P. Feng, M.-Y. Hu, W.-J. Li, X. Wu, S.-Y. Xiang, S.-Q. Yu, *Toxicology and Applied Pharmacology* **2021**, *414*, 115411.
- [118] Y. Lu, Y.-Y. Wang, N. Yang, D. Zhang, F.-Y. Zhang, H.-T. Gao, W.-T. Rong, S.-Q. Yu, Q. Xu, *Toxicological Sciences* **2014**, *139*, 317–327.
- [119] M. Mezei, *Journal of Investigative Dermatology* **1975**, *64*, 165–168.
- [120] H. Khan, N. Akhtar, T. Mahmood, A. Jameel, S. Mohsin, *International Journal of Cosmetic Science* **2014**, *37*, 76–81.
- [121] B. A. Kerwin, *Journal of Pharmaceutical Sciences* **2008**, *97*, 2924–2935.
- [122] T. W. Patapoff, O. Esue, *Pharmaceutical Development and Technology* **2009**, *14*, 659–664.
- [123] M. Rabe, A. Kerth, A. Blume, P. Garidel, *European Biophysics Journal* **2020**, *49*, 533–547.
- [124] T. Diederichs, J. J. Mittag, J. Humphrey, S. Voss, S. Carle, J. Buske, P. Garidel, *International Journal of Pharmaceutics* **2023**, *635*, 122660.
- [125] L. Zang, F. van Kuijk, B. Misra, H. Misra, *Biochemistry and molecular biology international* **1995**, *37*, 283–293.
- [126] M. Bancirova, *Luminescence* **2011**, *26*, 685–688.
- [127] H. Sun, R. Yang, J. Wang, X. Yang, J. Tu, L. Xie, C. Li, Q. Lao, C. Sun, *RSC Advances* **2017**, *7*, 15127–15138.
- [128] D. Hewitt, T. Zhang, Y.-H. Kao, *Journal of Chromatography A* **2008**, *1215*, 156–160.
- [129] N. Doshi, R. Fish, K. Padilla, S. Yadav, *Journal of Pharmaceutical Sciences* **2020**, *109*, 2986–2995.
- [130] A. Tomlinson, I. E. Zarraga, B. Demeule, *Molecular Pharmaceutics* **2020**, *17*, 2345–2353.
- [131] R. Zhang, Y. Wang, L. Tan, H. Y. Zhang, M. Yang, *Journal of Chromatographic Science* **2012**, *50*, 598–607.
- [132] P. Alvarez, S. Detremmerie, T. Cucu, G. Vanhoenacker, S. Denorme, C. Lecluyse, J. Deryckere, B. D'Haenens, F. David, P. Sandra, *LCGC Europe* **2023**, (Ed.: K. Sandra), 267–274.

- [133] D. Ilko, A. Braun, O. Germershaus, L. Meinel, U. Holzgrabe, *European Journal of Pharmaceutics and Biopharmaceutics* **2015**, *94*, 569–574.
- [134] M. A. Pegues, K. Szczepanek, F. Sheikh, S. G. Thacker, B. Aryal, M. K. Ghorab, S. Wolfgang, R. P. Donnelly, D. Verthelyi, V. A. Rao, *Pharmaceutical Research* **2021**, *38*, 1961–1975.
- [135] G. Kollamaram, G. Williams, *Journal of Excipients and Food Chemicals* **2021**, *12*, 32–40.
- [136] W. R. Wasylaschuk, P. A. Harmon, G. Wagner, A. B. Harman, A. C. Templeton, H. Xu, R. A. Reed, *Journal of Pharmaceutical Sciences* **2007**, *96*, 106–116.
- [137] A. Martos, W. Koch, W. Jiskoot, K. Wuchner, G. Winter, W. Friess, A. Hawe, *Journal of Pharmaceutical Sciences* **2017**, *106*, 1722–1735.
- [138] R. S. Kishore, A. Pappenberger, I. B. Dauphin, A. Ross, B. Buergi, A. Staempfli, H.-C. Mahler, *Journal of Pharmaceutical Sciences* **2011**, *100*, 721–731.
- [139] N. R. Larson, Y. Wei, I. Prajapati, A. Chakraborty, B. Peters, C. Kalonia, S. Hudak, S. Choudhary, R. Esfandiary, P. Dhar, C. Schöneich, C. R. Middaugh, *Journal of Pharmaceutical Sciences* **2020**, *109*, 633–639.
- [140] J. Weber, J. Buske, K. Mäder, P. Garidel, T. Diederichs, *International Journal of Pharmaceutics: X* **2023**, *6*, 100202.
- [141] M. Donbrow, E. Azaz, A. Pillersdorf, *Journal of Pharmaceutical Sciences* **1978**, *67*, 1676–1681.
- [142] J. Yao, D. K. Dokuru, M. Noestheden, S. S. Park, B. A. Kerwin, J. Jona, D. Ostovic, D. L. Reid, *Pharmaceutical Research* **2009**, *26*, 2303–2313.
- [143] W. Peter Wuelfing, K. Kosuda, A. C. Templeton, A. Harman, M. D. Mowery, R. A. Reed, *Journal of Pharmaceutical and Biomedical Analysis* **2006**, *41*, 774–782.
- [144] Z. CHENG, X. WANG, Q. CHEN, J. GUO, *International Journal of Applied Pharmaceutics* **2022**, 205–212.
- [145] S. Zhou, C. Schöneich, S. K. Singh, *AAPS PharmSciTech* **2011**, *12*, 411–421.
- [146] K. A. Fliszar, D. Walker, L. Allain, *PDA Journal of Pharmaceutical Science and Technology* **2006**, *60*, 337–342.
- [147] W. R. Haag, T. Mill, *Photochemistry and Photobiology* **1987**, *45*, 317–321.
- [148] R. D. Hall, C. F. Chignell, *Photochemistry and Photobiology* **1987**, *45*, 459–464.
- [149] T. Takajo, Y. Kurihara, K. Iwase, D. Miyake, K. Tsuchida, K. Anzai, *Chemical and Pharmaceutical Bulletin* **2020**, *68*, 150–154.
- [150] L. Zang, F. van Kuijk, B. Misra, H. Misra, *Biochemistry and molecular biology international* **1995**, *37*, 283–293.

- [151] C. Vever-Bizet, M. Dellinger, D. Brault, M. Rougee, R. V. Bensasson, *Photochemistry and Photobiology* **1989**, *50*, 321–325.
- [152] L. Zang, Z. Zhang, H. P. Misra, *Photochemistry and Photobiology* **1990**, *52*, 677–683.
- [153] R. R. Jones, R. G. Bergman, *Journal of the American Chemical Society* **1972**, *94*, 660–661.
- [154] R. G. Bergman, *Accounts of Chemical Research* **1973**, *6*, 25–31.
- [155] S. Chen, Q. Li, S. Sun, Y. Ding, A. Hu, *Macromolecules* **2017**, *50*, 534–541.
- [156] C. R. Hickenboth, J. D. Rule, J. S. Moore, *Tetrahedron* **2008**, *64*, 8435–8448.
- [157] X. Cheng, J. Ma, J. Zhi, X. Yang, A. Hu, *Macromolecules* **2009**, *43*, 909–913.
- [158] J. Ma, X. Ma, S. Deng, F. Li, A. Hu, *Journal of Polymer Science Part A: Polymer Chemistry* **2011**, *49*, 1368–1375.
- [159] B. Zhu, J. Ma, Z. Li, J. Hou, X. Cheng, G. Qian, P. Liu, A. Hu, *Journal of Materials Chemistry* **2011**, *21*, 2679.
- [160] A. Evenzahav, N. J. Turro, *Journal of the American Chemical Society* **1998**, *120*, 1835–1841.
- [161] S. Sarkar, K. P. S. Cheung, V. Gevorgyan, *Chemical Science* **2020**, *11*, 12974–12993.
- [162] J. C. Santos, J. Andres, A. Aizman, P. Fuentealba, V. Polo, *The Journal of Physical Chemistry A* **2005**, *109*, 3687–3693.
- [163] C. Miao, J. Zhi, S. Sun, X. Yang, A. Hu, *Journal of Polymer Science Part A: Polymer Chemistry* **2010**, *48*, 2187–2193.
- [164] Y. Cai, W. H. Binder, *Macromolecular Rapid Communications* **2023**, *44*, DOI 10.1002/marc.202300440.
- [165] B. L. Bales, M. Meyer, S. Smith, M. Peric, *The Journal of Physical Chemistry A* **2009**, *113*, 4930–4940.
- [166] S. Chen, B. Huang, S. Sun, Y. Ding, A. Hu, *Asian Journal of Organic Chemistry* **2017**, *6*, 775–779.
- [167] M. Klein, T. Walenzyk, B. König, *Collection of Czechoslovak Chemical Communications* **2004**, *69*, 945–965.
- [168] L.-N. Zou, X. Cheng, M. L. Rivers, H. M. Jaeger, S. R. Nagel, *Science* **2009**, *326*, 408–410.
- [169] V. Madhavan, R. H. Schuler, R. W. Fessenden, *Journal of the American Chemical Society* **1978**, *100*, 888–893.
- [170] M. Prall, A. Wittkopp, A. A. Fokin, P. R. Schreiner, *Journal of Computational Chemistry* **2001**, *22*, 1605–1614.

- [171] L. Qin, L. Li, Y. Sha, Z. Wang, D. Zhou, W. Chen, G. Xue, *Polymers* **2018**, *10*, 1007.
- [172] Y. Huang, S. Cheng, *Journal of Polymer Science* **2021**, *59*, 2819–2831.
- [173] K. J. Breslauer, D. P. Remeta, W. Y. Chou, R. Ferrante, J. Curry, D. Zaunczkowski, J. G. Snyder, L. A. Marky, *Proceedings of the National Academy of Sciences* **1987**, *84*, 8922–8926.
- [174] M. Tang, F. Szoka, *Gene Therapy* **1997**, *4*, 823–832.
- [175] P. Bhattacharya, S. Chakraborty, A. Balaji, A. Basak, *RSC Advances* **2022**, *12*, 23552–23565.
- [176] J. Hioe, D. Šakić, V. Vrček, H. Zipse, *Org. Biomol. Chem.* **2015**, *13*, 157–169.
- [177] J. Buback, M. Kullmann, F. Langhojer, P. Nuernberger, R. Schmidt, F. Würthner, T. Brixner, *Journal of the American Chemical Society* **2010**, *132*, 16510–16519.
- [178] K. Imato, K. Momota, N. Kaneda, I. Imae, Y. Ooyama, *Chemistry of Materials* **2022**, *34*, 8289–8296.
- [179] T. Matsuhira, H. Yamamoto, T.-a. Okamura, *Chemistry Letters* **2009**, *38*, 666–667.
- [180] A. A. Beharry, G. A. Woolley, *Chemical Society Reviews* **2011**, *40*, 4422.
- [181] M. Dong, A. Babalhavaeji, S. Samanta, A. A. Beharry, G. A. Woolley, *Accounts of Chemical Research* **2015**, *48*, 2662–2670.
- [182] M. W. H. Hoorens, M. Medved', A. D. Laurent, M. Di Donato, S. Fanetti, L. Slappendel, M. Hilbers, B. L. Feringa, W. Jan Buma, W. Szymanski, *Nature Communications* **2019**, *10*, DOI 10.1038/s41467-019-10251-8.
- [183] C. E. Weston, R. D. Richardson, P. R. Haycock, A. J. P. White, M. J. Fuchter, *Journal of the American Chemical Society* **2014**, *136*, 11878–11881.
- [184] D. T. Nguyen, M. Freitag, C. Gutheil, K. Sotthewes, B. J. Tyler, M. Böckmann, M. Das, F. Schlüter, N. L. Doltsinis, H. F. Arlinghaus, B. J. Ravoo, F. Glorius, *Angewandte Chemie International Edition* **2020**, *59*, 13651–13656.
- [185] N. B. Arndt, F. Schlüter, M. Böckmann, T. Adolphs, H. F. Arlinghaus, N. L. Doltsinis, B. J. Ravoo, *Langmuir* **2022**, *38*, 735–742.
- [186] B. Pramanik, S. Ahmed, *Gels* **2022**, *8*, 533.
- [187] M. Browning, A. Jefferson, J. Geter, K. Ghebreyessus, *Photochem* **2023**, *3*, 427–441.
- [188] A. M. Schulte, D. Kolarski, V. Sundaram, A. Srivastava, F. Tama, B. L. Feringa, W. Szymanski, *International Journal of Molecular Sciences* **2022**, *23*, 5326.
- [189] B. G. Dwyer, C. Wang, D. Abegg, B. Racioppo, N. Qiu, Z. Zhao, D. Pechalrieu, A. Shuster, D. G. Hoch, A. Adibekian, *Angewandte Chemie International Edition* **2020**, *60*, 3071–3079.

- [190] G. Davidson-Rozenfeld, L. Stricker, J. Simke, M. Fadeev, M. Vázquez-González, B. J. Ravoo, I. Willner, *Polymer Chemistry* **2019**, *10*, 4106–4115.
- [191] R. Steinbrecher, P. Zhang, C. M. Papadakis, P. Müller-Buschbaum, A. Taubert, A. Laschewsky, *Chemical Communications* **2024**, *60*, 1747–1750.
- [192] Y. Wang, X. Liu, G. Cui, W. Fang, W. Thiel, *Angewandte Chemie* **2016**, *128*, 14215–14219.
- [193] D. Kurzbach, D. R. Kattnig, B. Zhang, A. D. Schlüter, D. Hinderberger, *Chemical Science* **2012**, *3*, 2550.
- [194] A. Wasserman, L. Yasina, M. Motyakin, I. Aliev, N. Churochkina, L. Rogovina, E. Lysenko, V. Baranovsky, *Spectrochimica Acta Part A: Molecular and Biomolecular Spectroscopy* **2008**, *69*, 1344–1353.
- [195] A. Rübe, K. Mäder, *Journal of Biomedical Nanotechnology* **2005**, *1*, 208–213.
- [196] J. Reichenwallner, A. Thomas, T. Steinbach, J. Eisermann, C. E. H. Schmelzer, F. Wurm, D. Hinderberger, *Biomacromolecules* **2019**, *20*, 1118–1131.
- [197] L. Stricker, M. Böckmann, T. M. Kirse, N. L. Doltsinis, B. J. Ravoo, *Chemistry – A European Journal* **2018**, *24*, 8639–8647.
- [198] S. Crespi, N. A. Simeth, B. König, *Nature Reviews Chemistry* **2019**, *3*, 133–146.

9 References

10 Appendix

10.1 The LED-coupled EPR spectrometer setup

Product:
FC5-LED-365A-420Z-535TR-690M-850V Multi channel fiber coupled LED source with dual fiber.
S/N: 3160
Mfg. Date: June/2020
The User Manual can be found on-line on our Technical Documents page:
<http://www.prizmatix.com/pdf/FC/FC2-3-5-7-LED-UserManual-04.pdf>

Measuring instruments:

- A) Thorlabs S142C with 2" integrating Sphere and PM100
- B) Ophir Nova II with L50(150)A-35-BB sensor (for collimated beams)
- C) StellarNET EPP2000 Spectrometer

Ch. 1: LED 365A Output power 1500um fiber (NA=0.5, L=1 m) : 185 [mW], With Collimator: 175[mW]

Emission Spectrum:

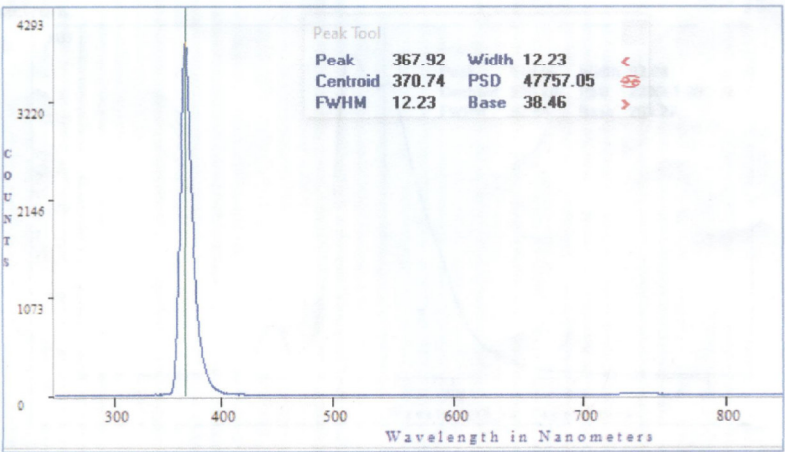
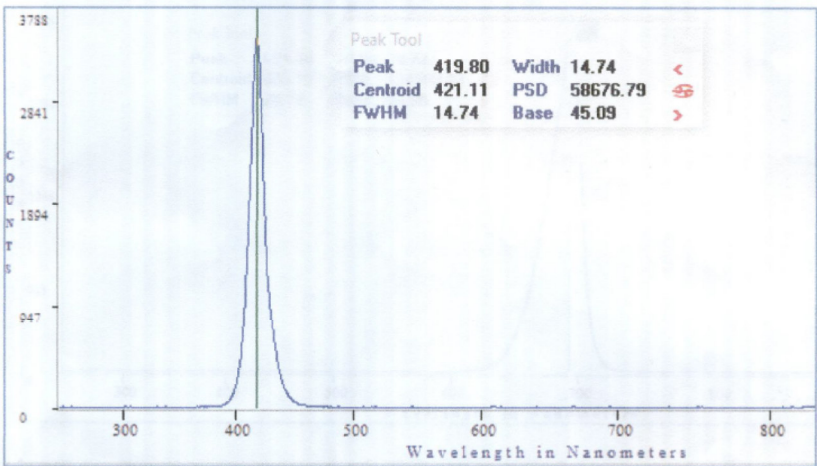


Figure 10.1: Excerpt (1/2) from the final product test report of the FC5 Multi channel fiber coupled LED light source (Prizmatix Ltd., Cholon, Israel).

Ch. 2: LED 420Z

**Output power 1500um fiber (NA=0.5, L=1m) : 215 [mW], With Collimator: 200[mW]
Emission Spectrum:**



Ch. 3: LED 535TR

**Output power 1500um fiber (NA=0.5, L=1 m) : 220 [mW], With Collimator: 200[mW]
Emission Spectrum:**

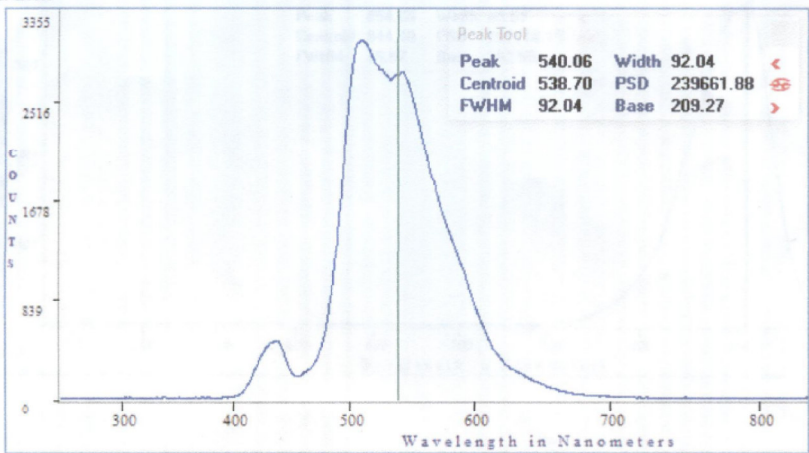


Figure 10.2: Excerpt (2/2) from the final product test report of the FC5 Multi channel fiber coupled LED light source (Prizmatix Ltd., Cholon, Israel).

10.2 The photodegradation in monoclonal antibody solutions

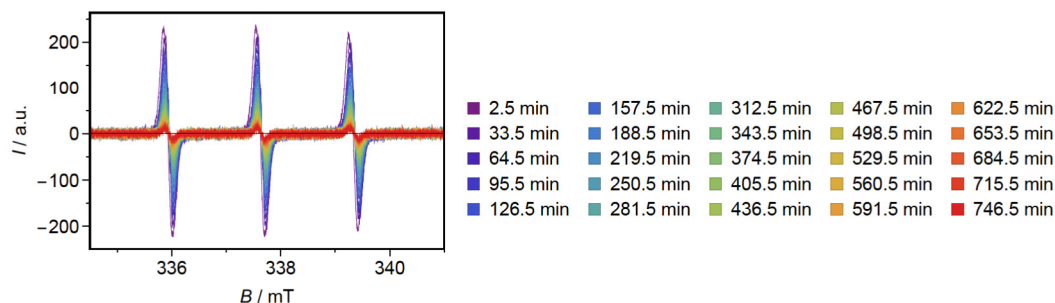


Figure 10.3: EPR spectra of 50 μM TEMPOL + 100 mg/ml mAb-II during irradiation with UV light, which were used to calculate the DI shown in Fig. 4.6.

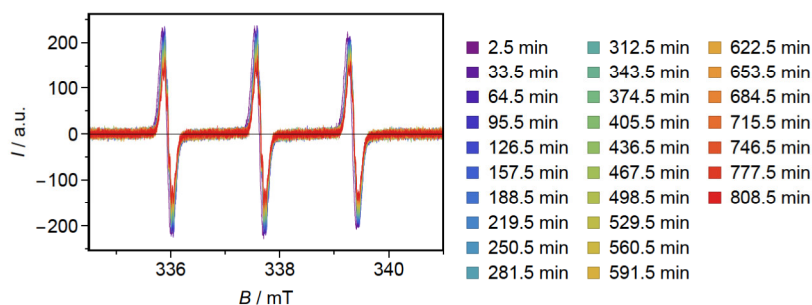


Figure 10.4: EPR spectra of 50 μM TEMPOL + 100 mg/ml mAb-II during irradiation with blue light, which were used to calculate the DI shown in Fig. 4.6.

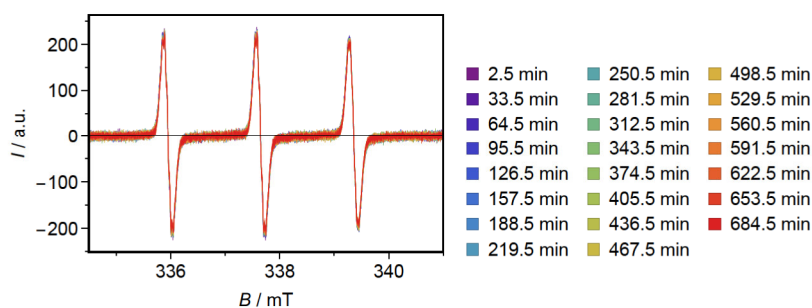


Figure 10.5: EPR spectra of 50 μM TEMPOL + 100 mg/ml mAb-II during irradiation with green light, which were used to calculate the DI shown in Fig. 4.6.

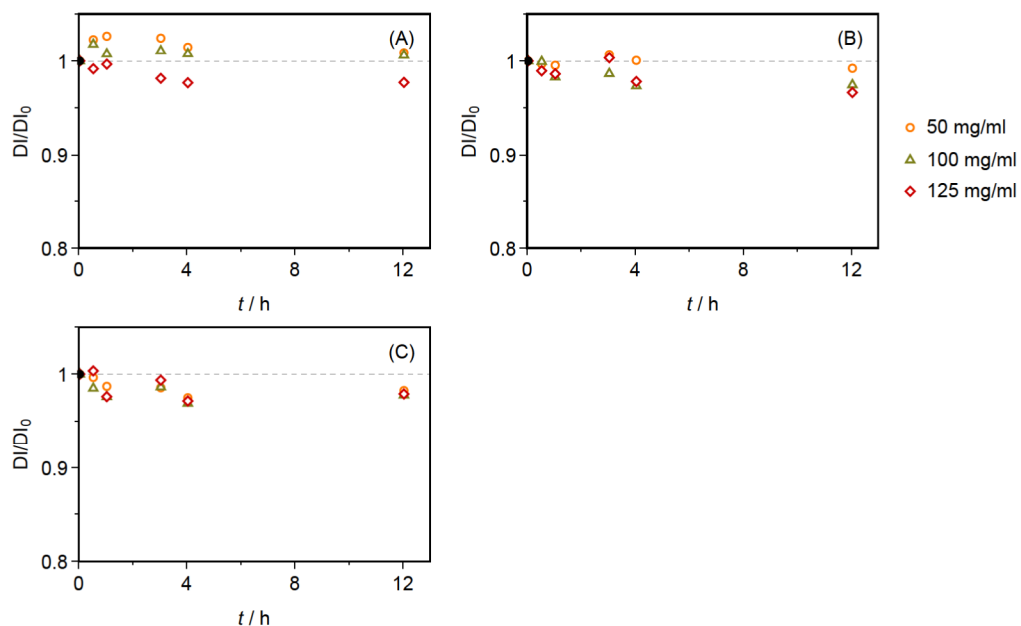


Figure 10.6: Normalized DI calculated from raw EPR spectra shown in Fig. 10.7. - 10.15

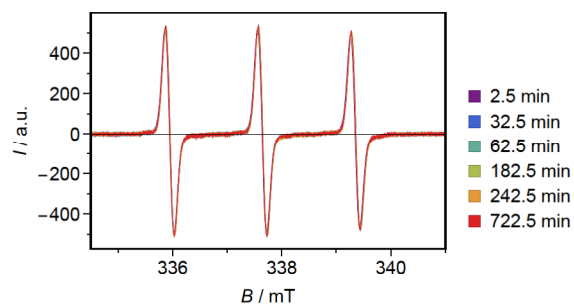


Figure 10.7: EPR spectra of 50 μ M TEMPOL in 50 mg/ml mAb-I solution, which were used to calculate the DI shown in Fig. 10.6.

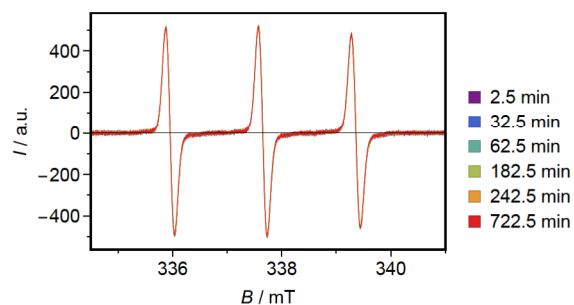


Figure 10.8: EPR spectra of 50 μ M TEMPOL in 100 mg/ml mAb-I solution, which were used to calculate the DI shown in Fig. 10.6.

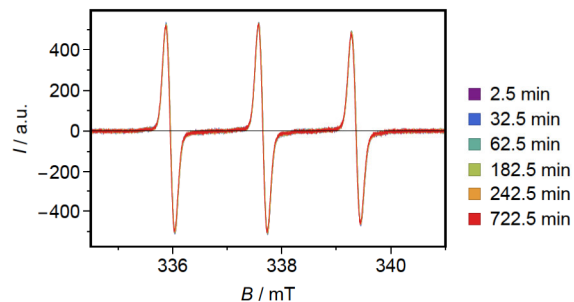


Figure 10.9: EPR spectra of 50 μM TEMPOL in 125 mg/ml mAb-I solution, which were used to calculate the DI shown in Fig. 10.6.

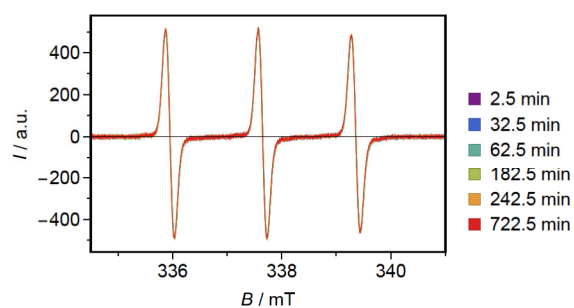


Figure 10.10: EPR spectra of 50 μM TEMPOL in 50 mg/ml mAb-II solution, which were used to calculate the DI shown in Fig. 10.6.

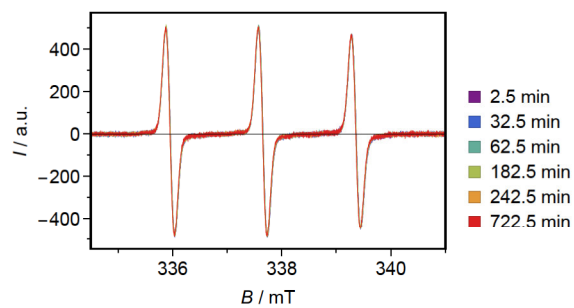


Figure 10.11: EPR spectra of 50 μM TEMPOL in 100 mg/ml mAb-II solution, which were used to calculate the DI shown in Fig. 10.6.

10 Appendix

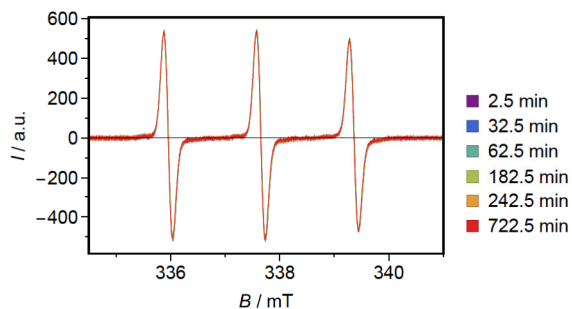


Figure 10.12: EPR spectra of 50 μM TEMPOL in 125 mg/ml mAb-II solution, which were used to calculate the DI shown in Fig. 10.6.

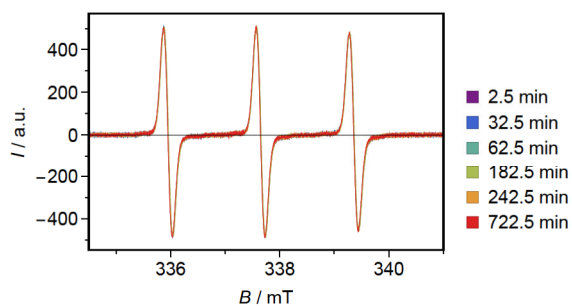


Figure 10.13: EPR spectra of 50 μM TEMPOL in 50 mg/ml mAb-III solution, which were used to calculate the DI shown in Fig. 10.6.

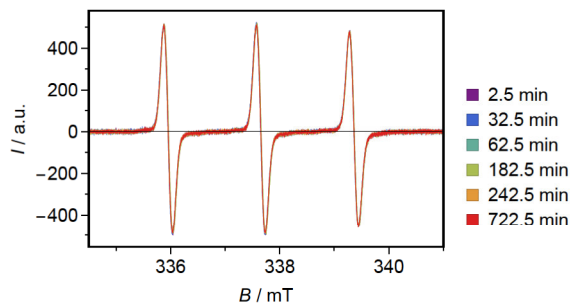


Figure 10.14: EPR spectra of 50 μM TEMPOL in 100 mg/ml mAb-III solution, which were used to calculate the DI shown in Fig. 10.6.

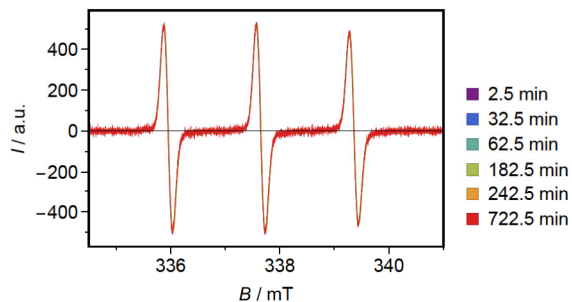


Figure 10.15: EPR spectra of 50 μM TEMPOL in 125 mg/ml mAb-III solution, which were used to calculate the DI shown in Fig. 10.6.

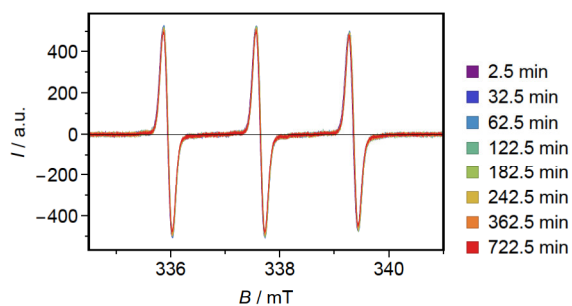


Figure 10.16: EPR spectra of 50 μM TEMPOL in 50 mg/ml mAb-I solution during irradiation inside the light chamber, which were used to calculate the DI shown in Fig. 4.7.

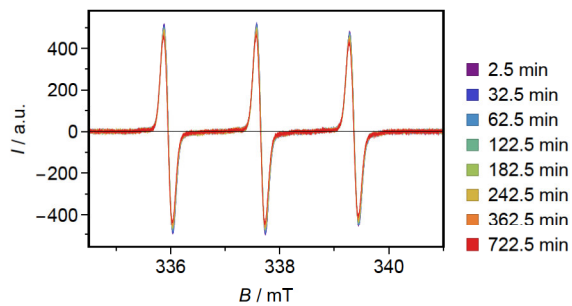


Figure 10.17: EPR spectra of 50 μM TEMPOL in 100 mg/ml mAb-I solution during irradiation inside the light chamber, which were used to calculate the DI shown in Fig. 4.7.

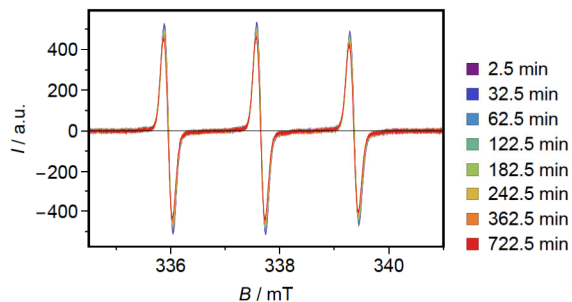


Figure 10.18: EPR spectra of 50 μM TEMPOL in 125 mg/ml mAb-I solution during irradiation inside the light chamber, which were used to calculate the DI shown in Fig. 4.7.

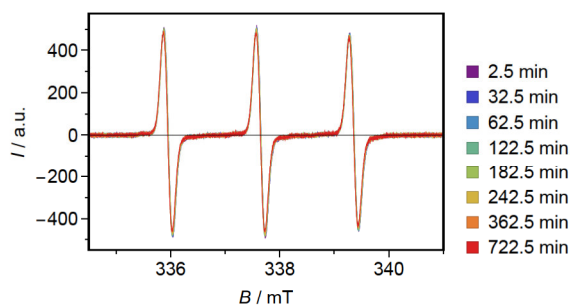


Figure 10.19: EPR spectra of 50 μM TEMPOL in 50 mg/ml mAb-II solution during irradiation inside the light chamber, which were used to calculate the DI shown in Fig. 4.7.

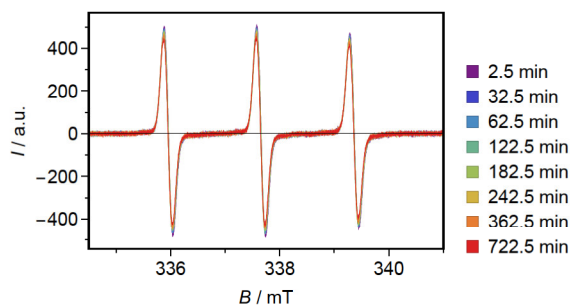


Figure 10.20: EPR spectra of 50 μM TEMPOL in 100 mg/ml mAb-II solution during irradiation inside the light chamber, which were used to calculate the DI shown in Fig. 4.7.

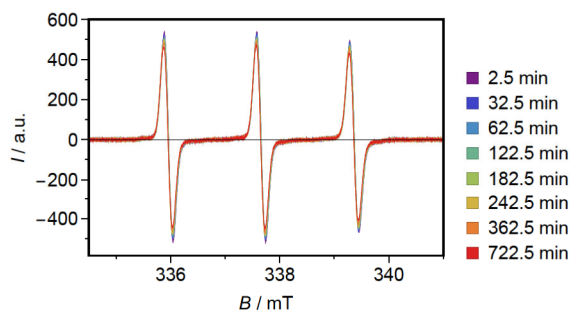


Figure 10.21: EPR spectra of 50 μM TEMPOL in 125 mg/ml mAb-II solution during irradiation inside the light chamber, which were used to calculate the DI shown in Fig. 4.7.

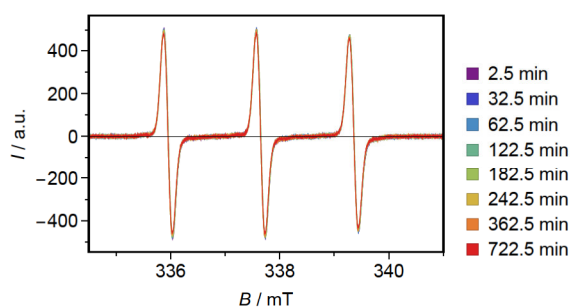


Figure 10.22: EPR spectra of 50 μM TEMPOL in 50 mg/ml mAb-III solution during irradiation inside the light chamber, which were used to calculate the DI shown in Fig. 4.7.

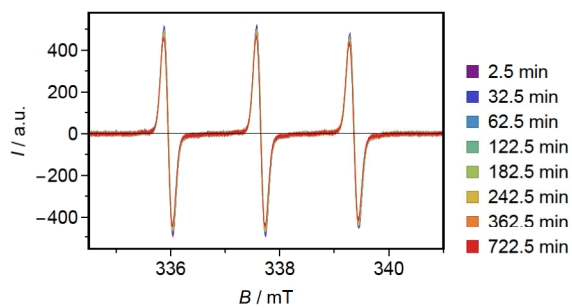


Figure 10.23: EPR spectra of 50 μM TEMPOL in 100 mg/ml mAb-III solution during irradiation inside the light chamber, which were used to calculate the DI shown in Fig. 4.7.

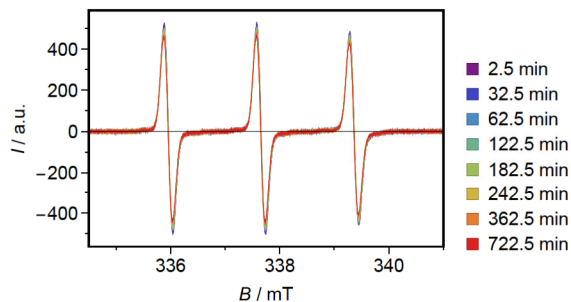


Figure 10.24: EPR spectra of 50 μM TEMPOL in 125 mg/ml mAb-III solution during irradiation inside the light chamber, which were used to calculate the DI shown in Fig. 4.7.

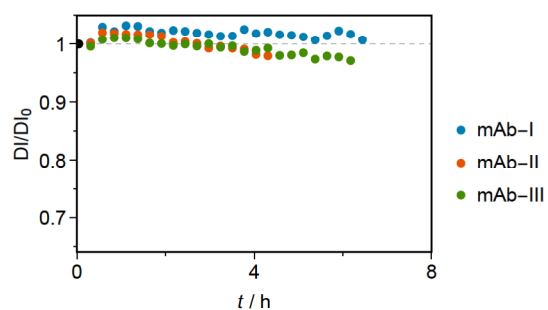


Figure 10.25: Normalized DI calculated from raw EPR spectra shown in Fig. 10.26. - 10.28

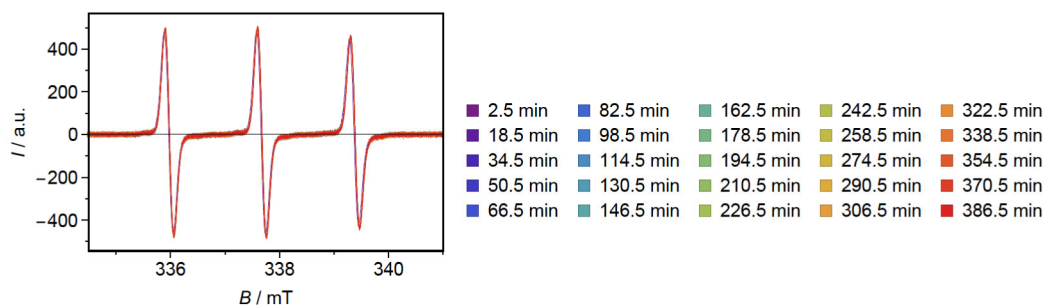


Figure 10.26: EPR spectra of 50 μM TEMPOL in 125 mg/ml mAb-I solution, which were used to calculate the DI shown in Fig. 10.25.

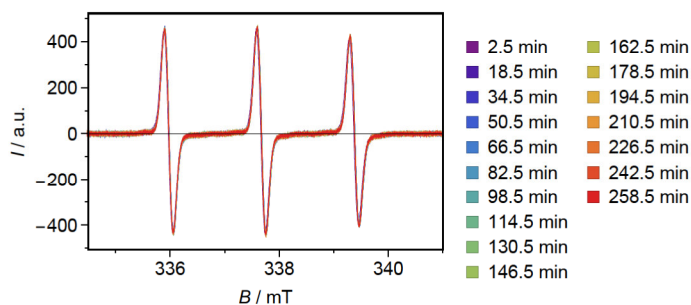


Figure 10.27: EPR spectra of 50 μM TEMPOL in 125 mg/ml mAb-II solution, which were used to calculate the DI shown in Fig. 10.25.

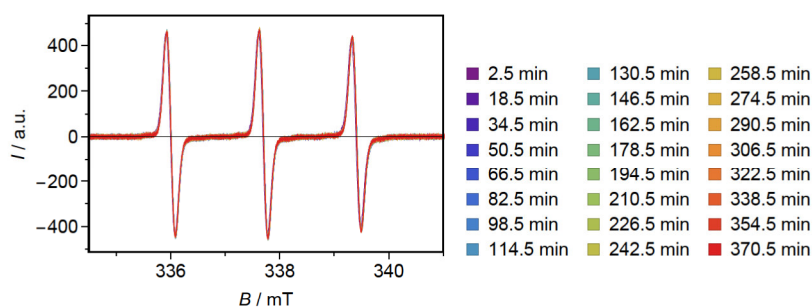


Figure 10.28: EPR spectra of 50 μM TEMPOL in 125 mg/ml mAb-III solution, which were used to calculate the DI shown in Fig. 10.25.

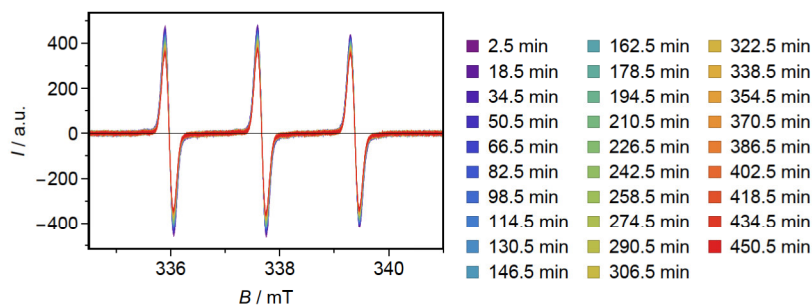


Figure 10.29: EPR spectra of 50 μM TEMPOL in 125 mg/ml mAb-I solution during irradiation with blue light, which were used to calculate the DI shown in Fig. 4.8.

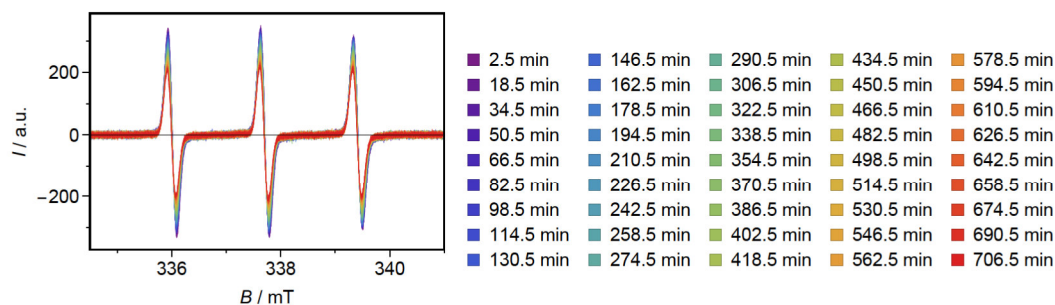


Figure 10.30: EPR spectra of 50 μM TEMPOL in 125 mg/ml mAb-II solution during irradiation with blue light, which were used to calculate the DI shown in Fig. 4.8.

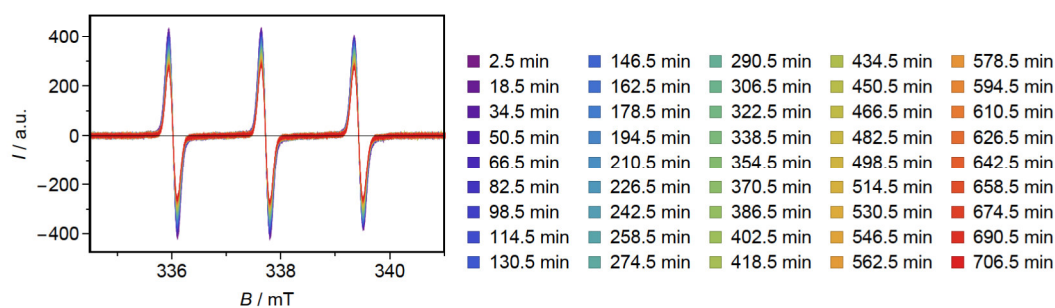


Figure 10.31: EPR spectra of 50 μM TEMPOL in 125 mg/ml mAb-III solution during irradiation with blue light, which were used to calculate the DI shown in Fig. 4.8.

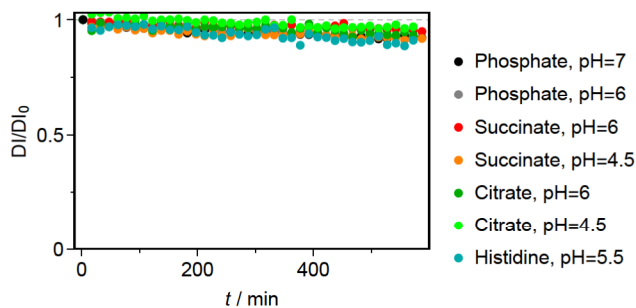


Figure 10.32: Normalized DI calculated from raw EPR spectra shown in Fig. 10.33-10.39.

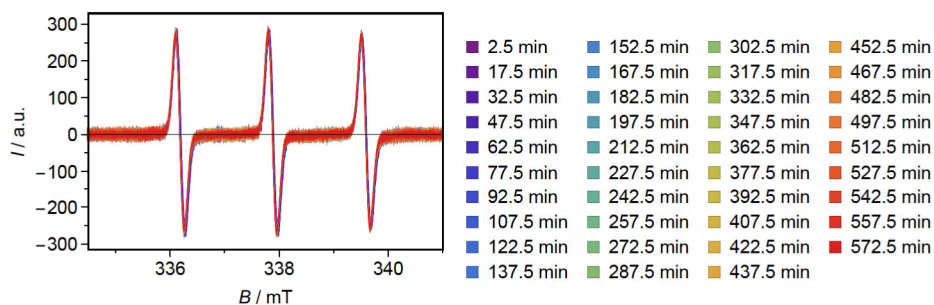


Figure 10.33: EPR spectra of 50 μM TEMPOL + 100 mg/ml mAb-III in 50 mM citrate buffer (pH=6), which were used to calculate the DI shown in Fig. 10.32.

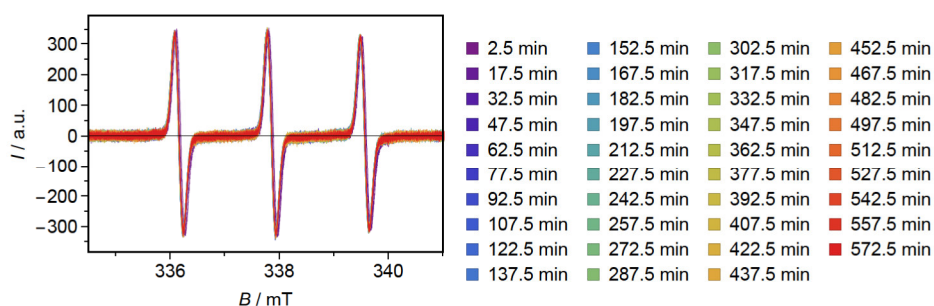


Figure 10.34: EPR spectra of 50 μM TEMPOL + 100 mg/ml mAb-III in 50 mM citrate buffer (pH=4.5), which were used to calculate the DI shown in Fig. 10.32.

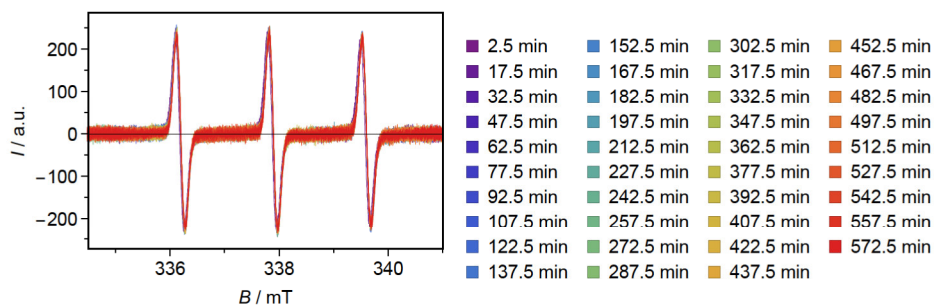


Figure 10.35: EPR spectra of 50 μM TEMPOL + 100 mg/ml mAb-III in 50 mM histidine buffer (pH=5.5), which were used to calculate the DI shown in Fig. 10.32.

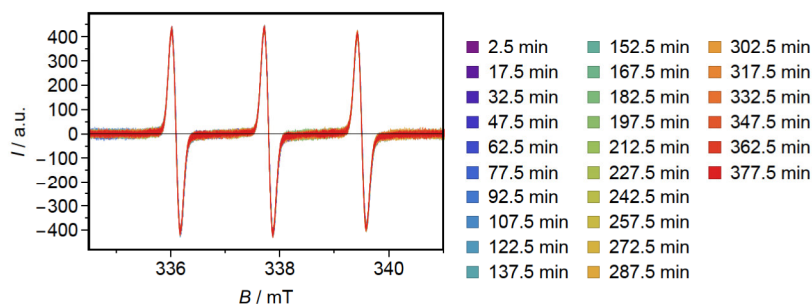


Figure 10.36: EPR spectra of 50 μ M TEMPOL + 100 mg/ml mAb-III in 50 mM phosphate buffer (pH=6), which were used to calculate the DI shown in Fig. 10.32.

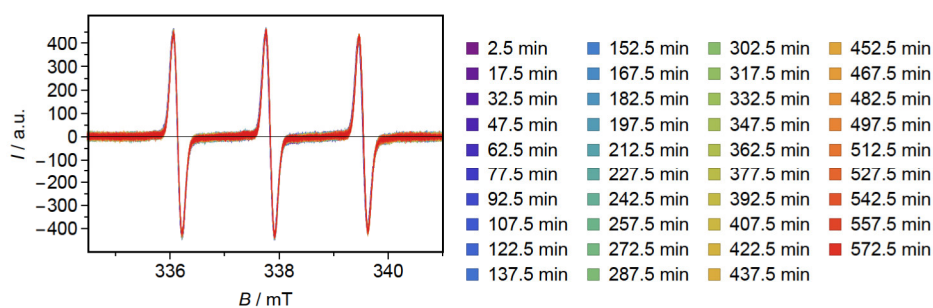


Figure 10.37: EPR spectra of 50 μ M TEMPOL + 100 mg/ml mAb-III in 50 mM phosphate buffer (pH=7), which were used to calculate the DI shown in Fig. 10.32.

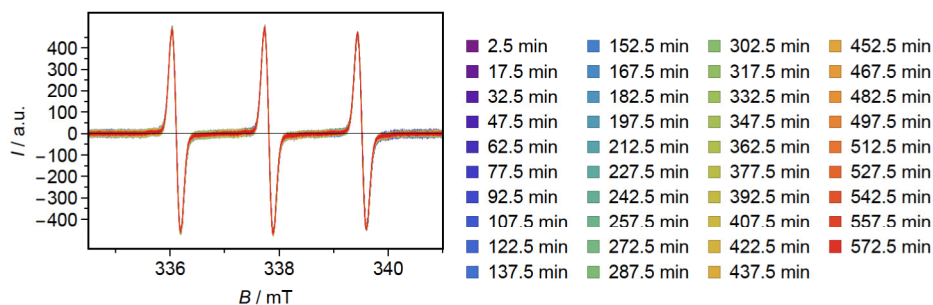


Figure 10.38: EPR spectra of 50 μ M TEMPOL + 100 mg/ml mAb-III in 50 mM succinate buffer (pH=6), which were used to calculate the DI shown in Fig. 10.32.

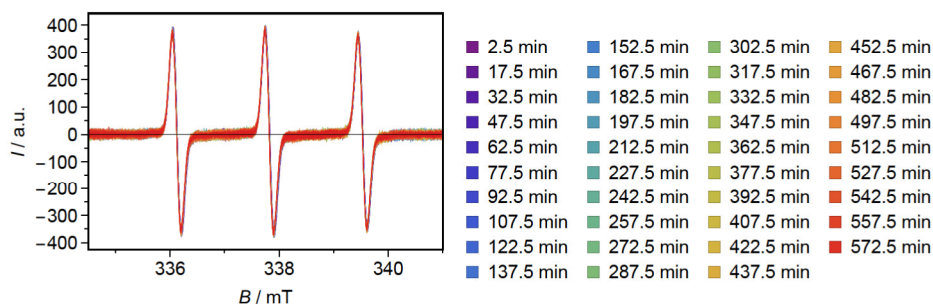


Figure 10.39: EPR spectra of 50 μM TEMPOL + 100 mg/ml mAb-III in 50 mM succinate buffer (pH=4.5), which were used to calculate the DI shown in Fig. 10.32.

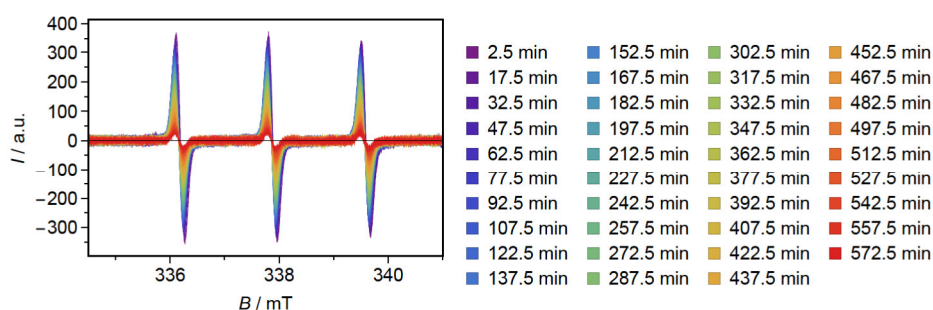


Figure 10.40: EPR spectra of 50 μM TEMPOL + 100 mg/ml mAb-III in 50 mM citrate buffer (pH=6) during irradiation with blue light, which were used to calculate the DI shown in Fig. 4.10.

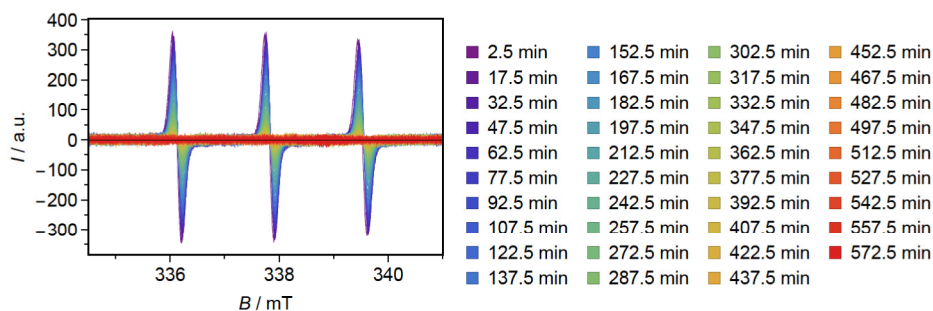


Figure 10.41: EPR spectra of 50 μM TEMPOL + 100 mg/ml mAb-III in 50 mM citrate buffer (pH=4.5) during irradiation with blue light, which were used to calculate the DI shown in Fig. 4.10.

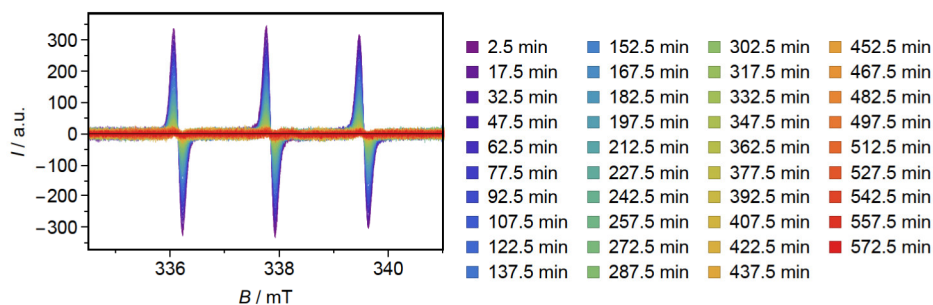


Figure 10.42: EPR spectra of 50 μM TEMPOL + 100 mg/ml mAb-III in 50 mM histidine buffer (pH=5.5) during irradiation with blue light, which were used to calculate the DI shown in Fig. 4.10.

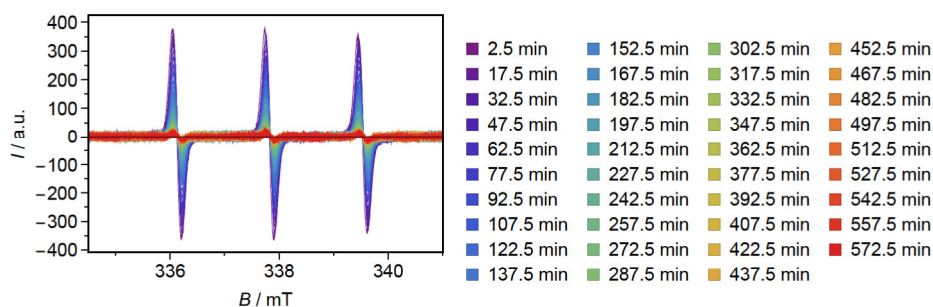


Figure 10.43: EPR spectra of 50 μM TEMPOL + 100 mg/ml mAb-III in 50 mM histidine buffer (pH=6.5) during irradiation with blue light, which were used to calculate the DI shown in Fig. 4.10.

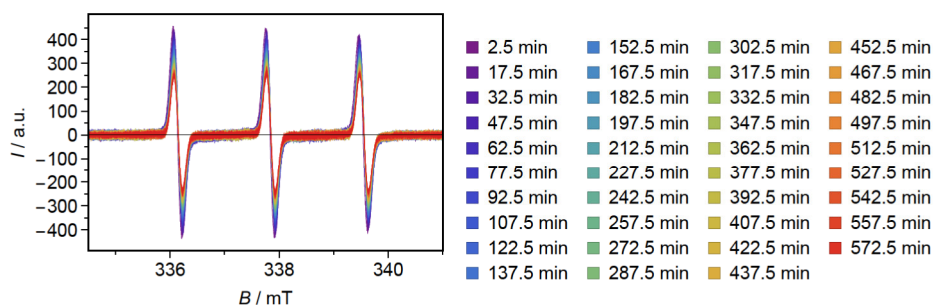


Figure 10.44: EPR spectra of 50 μM TEMPOL + 100 mg/ml mAb-III in 50 mM phosphate buffer (pH=6) during irradiation with blue light, which were used to calculate the DI shown in Fig. 4.10.

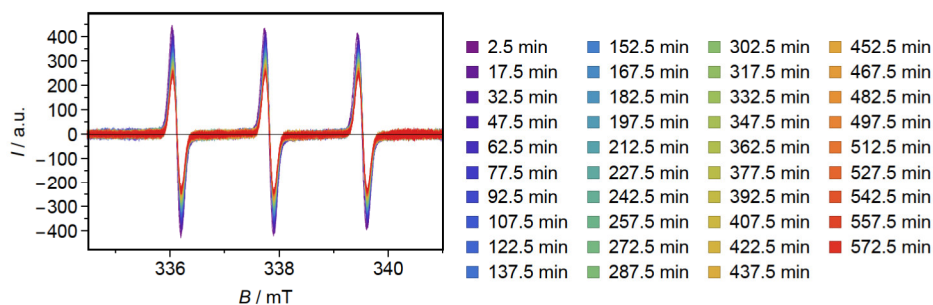


Figure 10.45: EPR spectra of 50 μM TEMPOL + 100 mg/ml mAb-III in 50 mM phosphate buffer (pH=7) during irradiation with blue light, which were used to calculate the DI shown in Fig. 4.10.

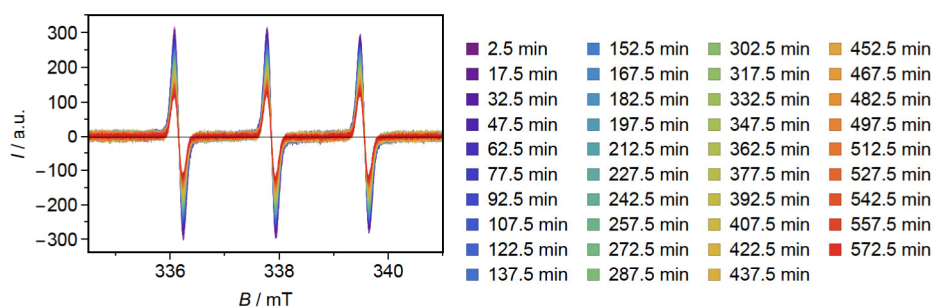


Figure 10.46: EPR spectra of 50 μM TEMPOL + 100 mg/ml mAb-III in 50 mM succinate buffer (pH=6) during irradiation with blue light, which were used to calculate the DI shown in Fig. 4.10.

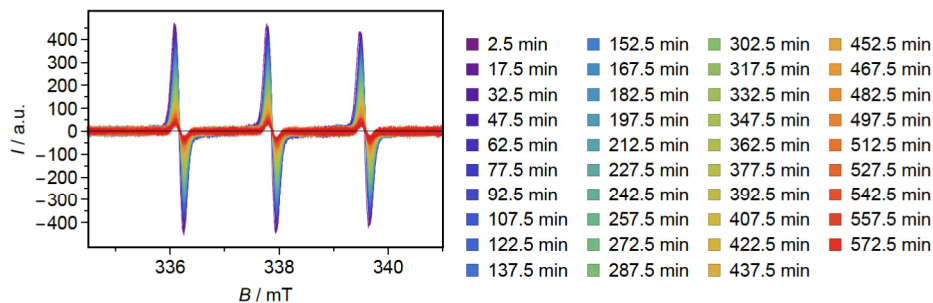


Figure 10.47: EPR spectra of 50 μM TEMPOL + 100 mg/ml mAb-III in 50 mM succinate buffer (pH=4.5) during irradiation with blue light, which were used to calculate the DI shown in Fig. 4.10.

10.3 The photodegradation of polysorbate

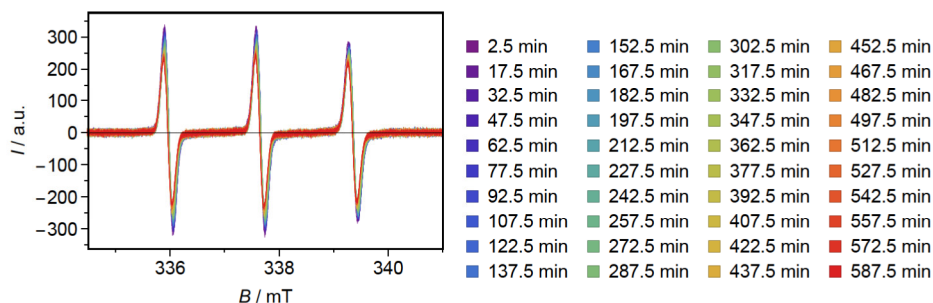


Figure 10.48: EPR spectra of 50 μM TEMPOL + 100 mg/ml polysorbate 80HP during irradiation with blue light, which were used to calculate the DI shown in Fig. 5.3.

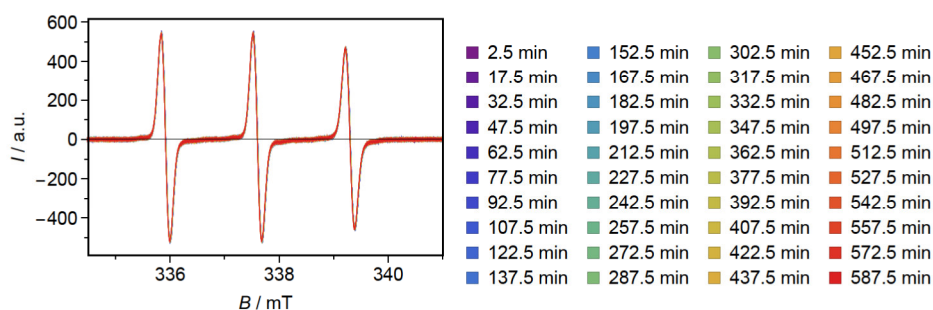


Figure 10.49: EPR spectra of 50 μM TEMPOL + 100 mg/ml polysorbate 80SR during irradiation with blue light, which were used to calculate the DI shown in Fig. 5.3.

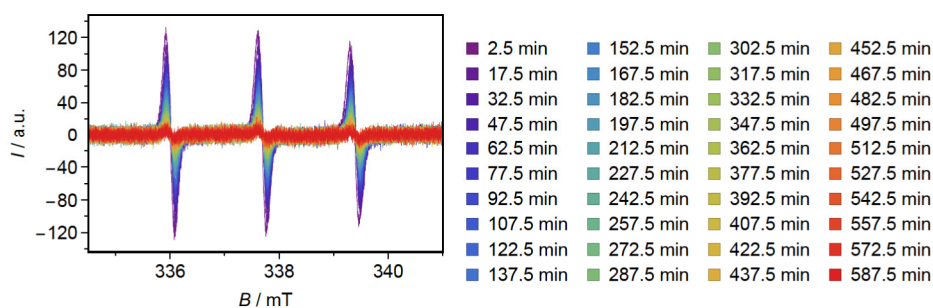


Figure 10.50: EPR spectra of 50 μM TEMPOL + 100 mg/ml polysorbate 20HP during irradiation with blue light, which were used to calculate the DI shown in Fig. 5.3.

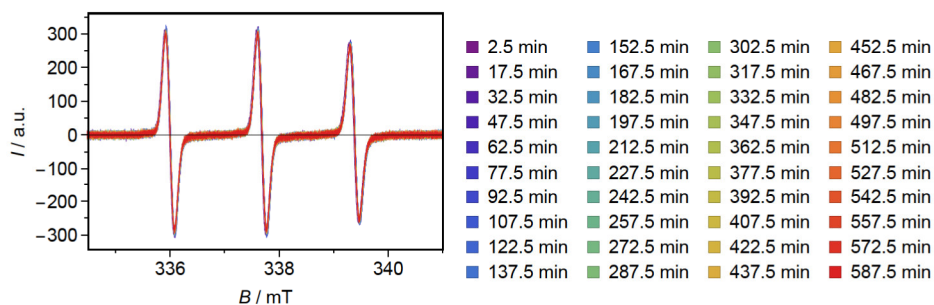


Figure 10.51: EPR spectra of 50 μM TEMPOL + 100 mg/ml polysorbate 20SR during irradiation with blue light, which were used to calculate the DI shown in Fig. 5.3.

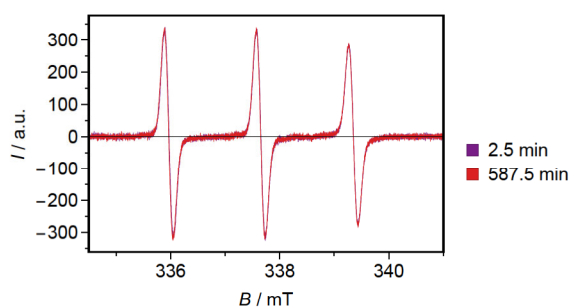


Figure 10.52: EPR spectra of 50 μM TEMPOL + 100 mg/ml polysorbate 80HP, which were used to calculate the DI of the dark control shown in Fig. 5.3.

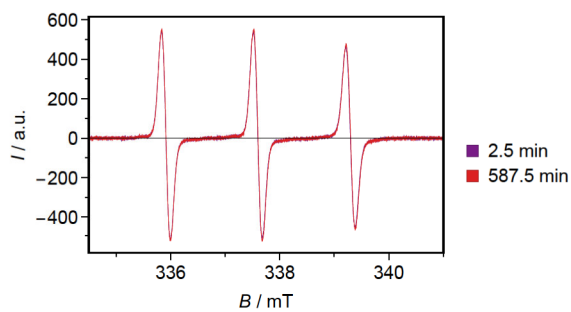


Figure 10.53: EPR spectra of 50 μM TEMPOL + 100 mg/ml polysorbate 80SR, which were used to calculate the DI of the dark control shown in Fig. 5.3.

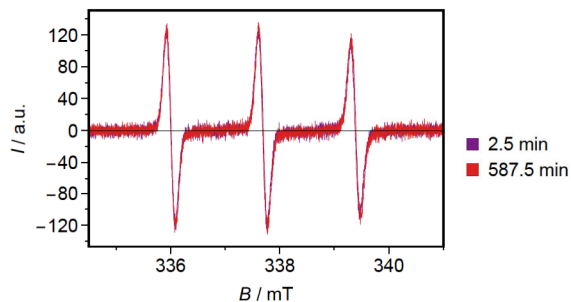


Figure 10.54: EPR spectra of 50 μM TEMPOL + 100 mg/ml polysorbate 20HP, which were used to calculate the DI of the dark control shown in Fig. 5.3.

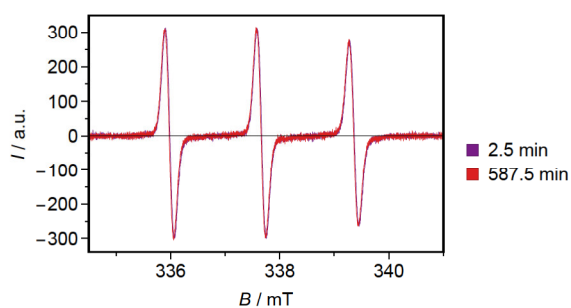


Figure 10.55: EPR spectra of 50 μM TEMPOL + 100 mg/ml polysorbate 20SR, which were used to calculate the DI of the dark control shown in Fig. 5.3.

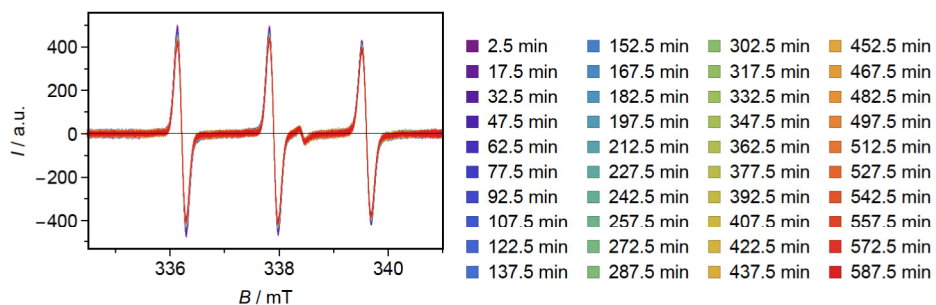


Figure 10.56: EPR spectra of 50 μM TEMPOL + 100 mg/ml polysorbate 80HP + 500 mM sodium azide during irradiation with blue light, which were used to calculate the DI shown in Fig. 5.4.

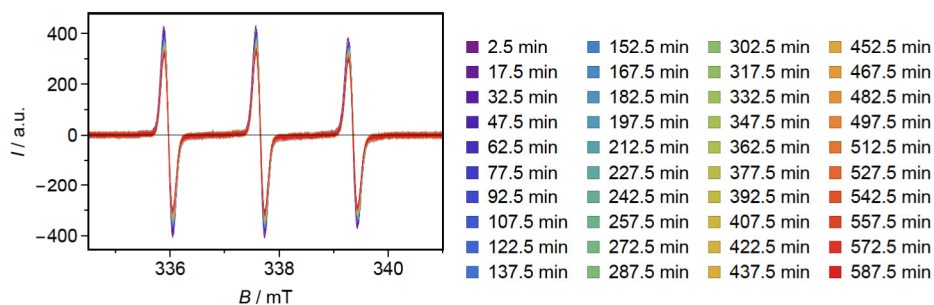


Figure 10.57: EPR spectra of 50 μ M TEMPOL + 100 mg/ml polysorbate 20HP + 500 mM sodium azide during irradiation with blue light, which were used to calculate the DI shown in Fig. 5.4.

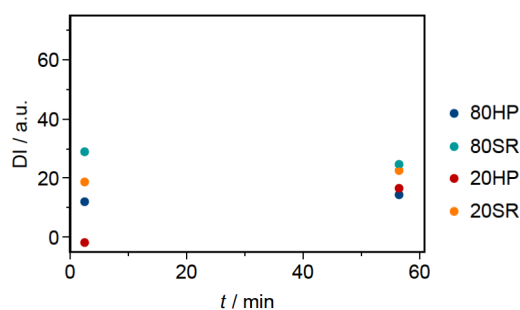


Figure 10.58: DI of 50 mM TMP with 100 mg/ml of polysorbate 80HP/80SR/20HP/20SR at 25 °C. The raw spectra are shown in Fig. 10.59 - 10.55.

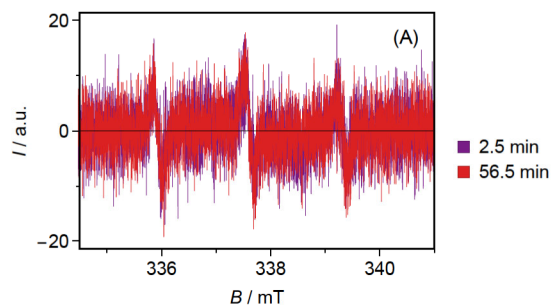


Figure 10.59: EPR spectra of 50 mM TMP + 100 mg/ml polysorbate 80HP recorded at 25 °C, which were used to calculate the DI shown in Fig. 10.58.

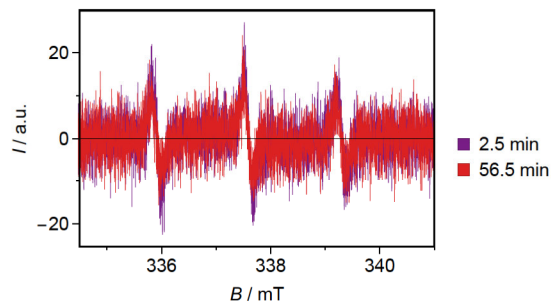


Figure 10.60: EPR spectra of 50 mM TMP + 100 mg/ml polysorbate 80SR recorded at 25 °C, which were used to calculate the DI shown in Fig. 10.58.

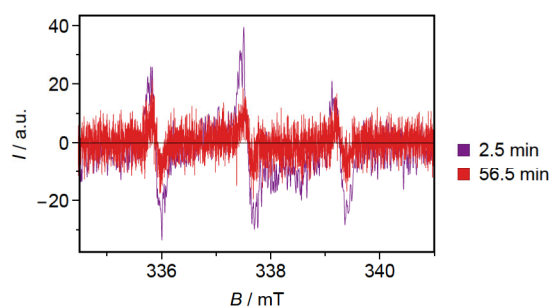


Figure 10.61: EPR spectra of 50 mM TMP + 100 mg/ml polysorbate 20HP recorded at 25 °C, which were used to calculate the DI shown in Fig. 10.58.

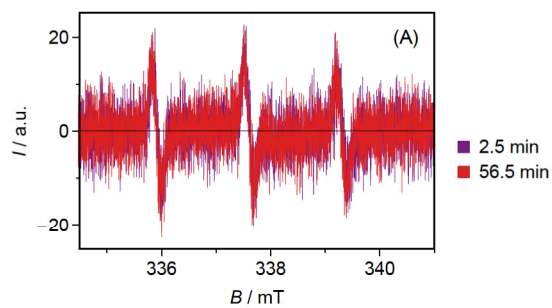


Figure 10.62: EPR spectra of 50 mM TMP + 100 mg/ml polysorbate 20SR recorded at 25 °C, which were used to calculate the DI shown in Fig. 10.58.

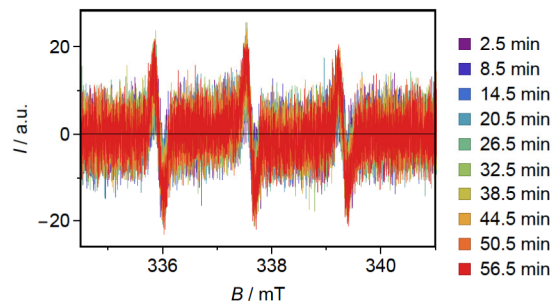


Figure 10.63: EPR spectra of 50 mM TMP + 100 mg/ml polysorbate 80HP recorded at 25 °C during irradiation with blue light, which were used to calculate the DI shown in Fig. 5.6.

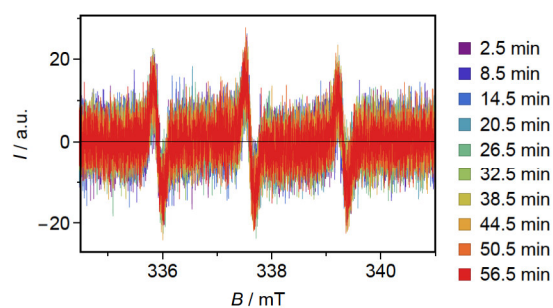


Figure 10.64: EPR spectra of 50 mM TMP + 100 mg/ml polysorbate 80SR recorded at 25 °C during irradiation with blue light, which were used to calculate the DI shown in Fig. 5.6.

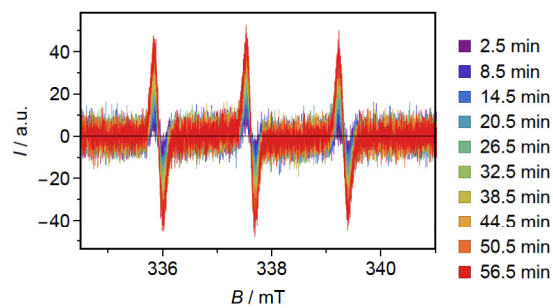


Figure 10.65: EPR spectra of 50 mM TMP + 100 mg/ml polysorbate 20HP recorded at 25 °C during irradiation with blue light, which were used to calculate the DI shown in Fig. 5.6.

10 Appendix

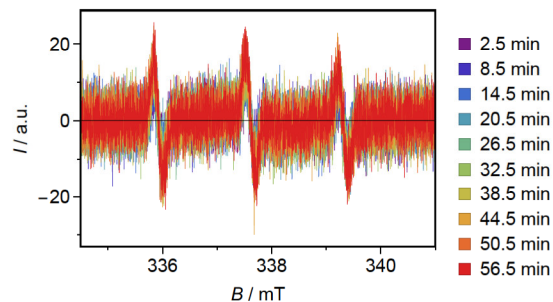


Figure 10.66: EPR spectra of 50 mM TMP + 100 mg/ml polysorbate 20SR recorded at 25 °C during irradiation with blue light, which were used to calculate the DI shown in Fig. 5.6.

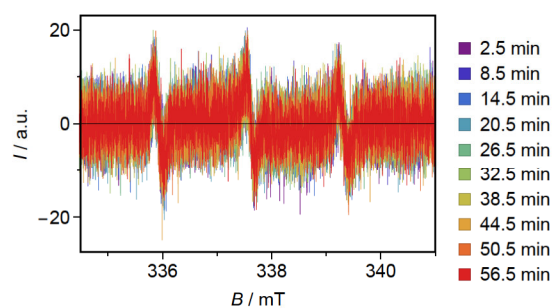


Figure 10.67: EPR spectra of 50 mM TMP + 100 mg/ml polysorbate 80HP + 500 mM sodium azide recorded at 25 °C during irradiation with blue light, which were used to calculate the DI shown in Fig. 5.6.

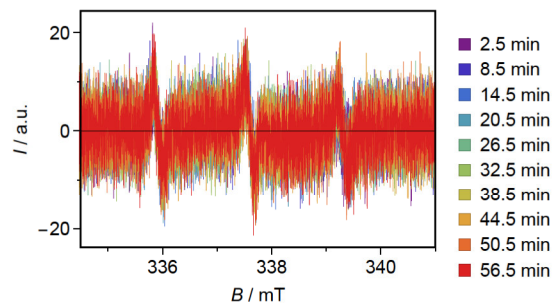


Figure 10.68: EPR spectra of 50 mM TMP + 100 mg/ml polysorbate 80SR + 500 mM sodium azide recorded at 25 °C during irradiation with blue light, which were used to calculate the DI shown in Fig. 5.6.

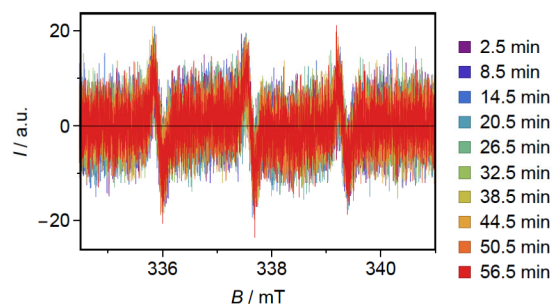


Figure 10.69: EPR spectra of 50mM TMP + 100 mg/ml polysorbate 20HP + 500mM sodium azide recorded at 25 °C during irradiation with blue light, which were used to calculate the DI shown in Fig. 5.6.

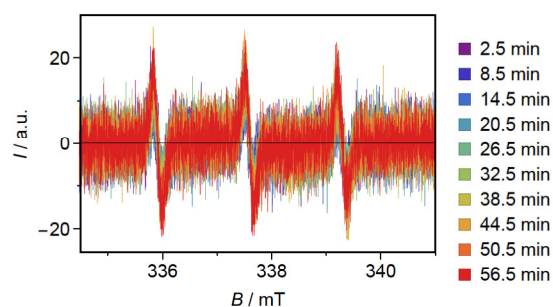


Figure 10.70: EPR spectra of 50mM TMP + 100 mg/ml polysorbate 20SR + 500mM sodium azide recorded at 25 °C during irradiation with blue light, which were used to calculate the DI shown in Fig. 5.6.

10.4 Bergman cyclisation of main-chain enediyne polymers

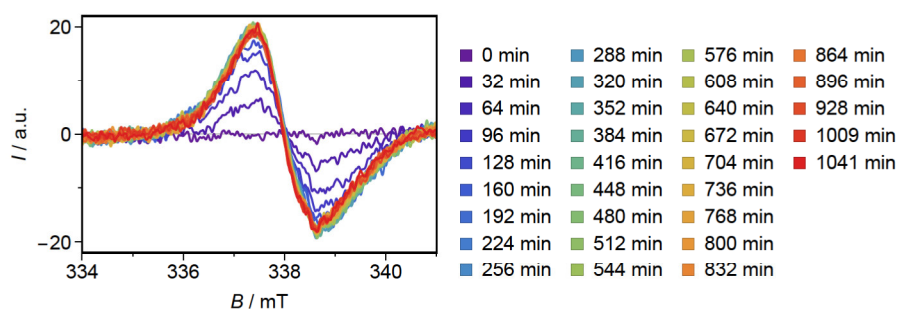


Figure 10.71: EPR spectra recorded at RT, which were used to calculate the DI shown in Fig. 6.6. Due to the low intensity, the spectra were recorded with a filter.

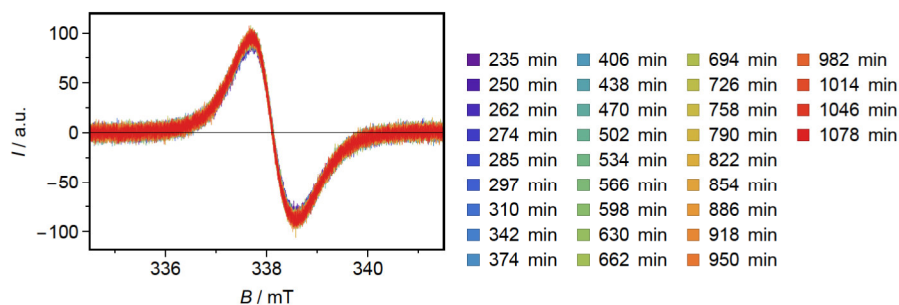


Figure 10.72: EPR spectra recorded at RT, which were used to calculate the DI shown in Fig. 6.7 (A) from $t=235$ min to $t=1078$ min.

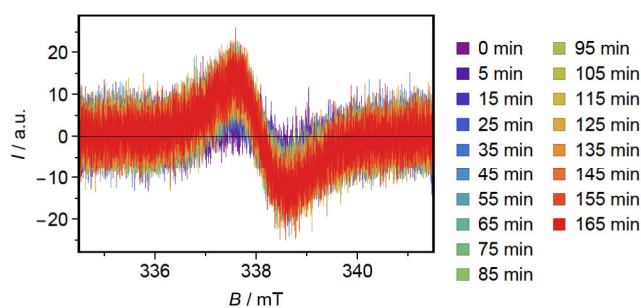


Figure 10.73: EPR spectra of 1.85 mg EDY-A during irradiation with blue light, which were used to calculate the DI shown in Fig. 6.9 (A).

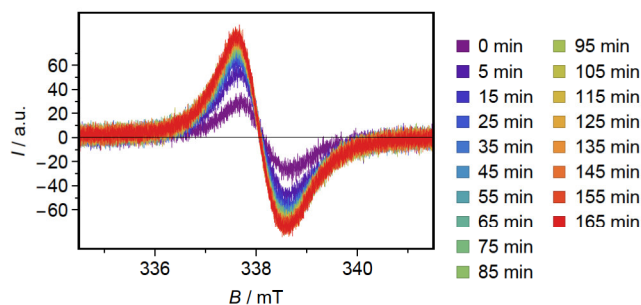


Figure 10.74: EPR spectra of 1.67 mg EDY-B during irradiation with blue light, which were used to calculate the DI shown in Fig. 6.9 (A).

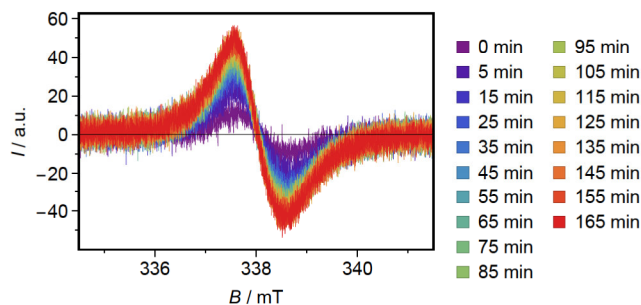


Figure 10.75: EPR spectra of 2.40 mg EDY-C during irradiation with blue light, which were used to calculate the DI shown in Fig. 6.9 (A).

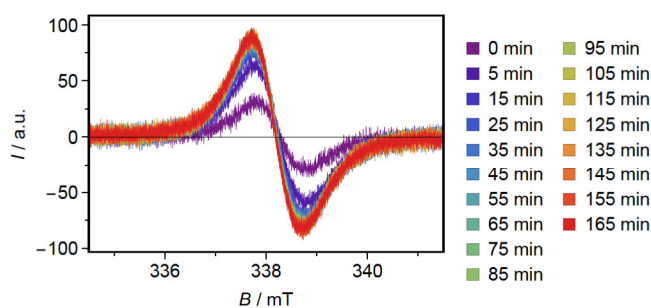


Figure 10.76: EPR spectra of 1.46 mg EDY-D during irradiation with blue light, which were used to calculate the DI shown in Fig. 6.9 (A).

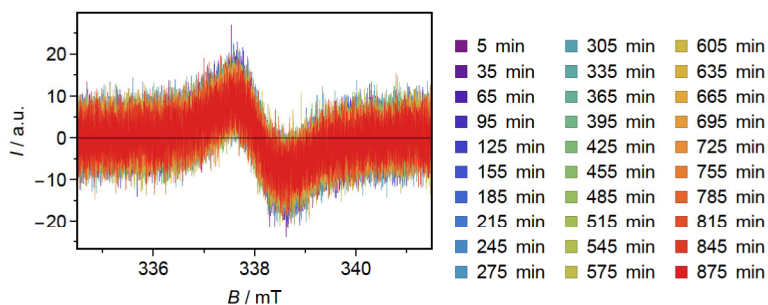


Figure 10.77: EPR spectra of 1.85 mg EDY-A during darkness after irradiation with blue light, which were used to calculate the DI shown in Fig. 6.9 (B).

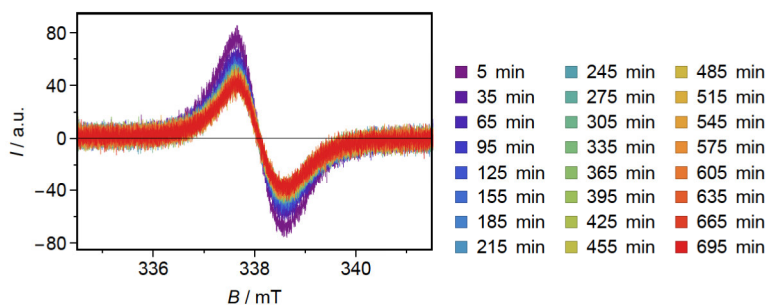


Figure 10.78: EPR spectra of 1.67 mg EDY-B during darkness after irradiation with blue light, which were used to calculate the DI shown in Fig. 6.9 (B).

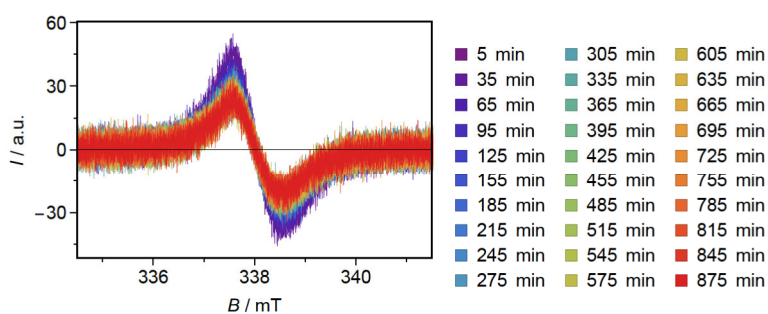


Figure 10.79: EPR spectra of 2.40 mg EDY-C during darkness after irradiation with blue light, which were used to calculate the DI shown in Fig. 6.9 (B).

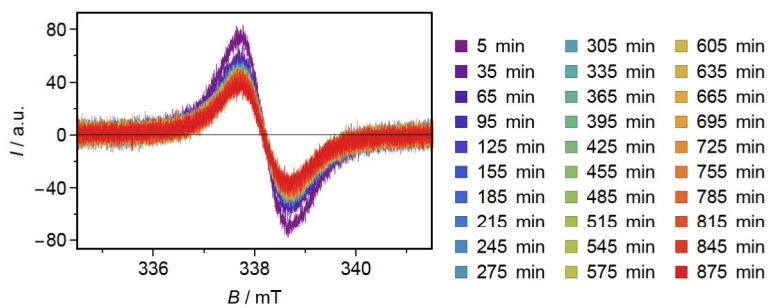


Figure 10.80: EPR spectra of 1.46 mg EDY-D during darkness after irradiation with blue light, which were used to calculate the DI shown in Fig. 6.9 (B).

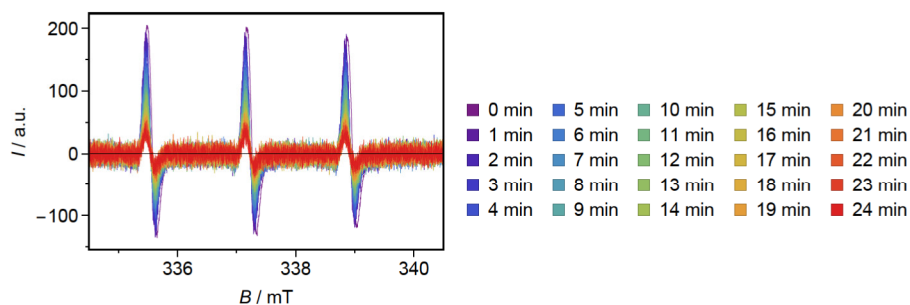


Figure 10.81: EPR spectra of 50 μM TEMPOL + 20 mM Poly EDY-A in TE buffer solution with 6.6 vol% DMSO during irradiation with blue light at 37°C, which were used to calculate the DI shown in Fig. 6.10.

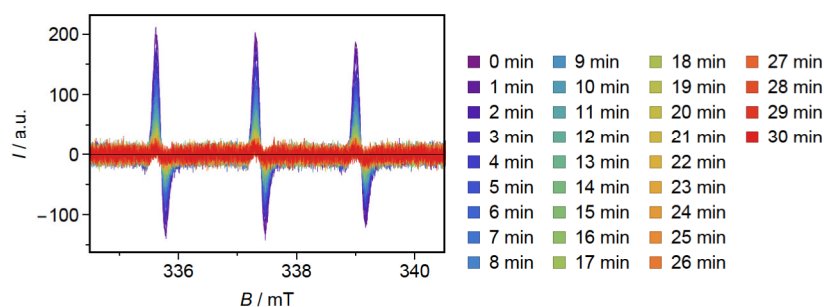


Figure 10.82: EPR spectra of 50 μM TEMPOL + 20 mM Poly EDY-B in TE buffer solution with 6.6 vol% DMSO during irradiation with blue light at 37°C, which were used to calculate the DI shown in Fig. 6.10.

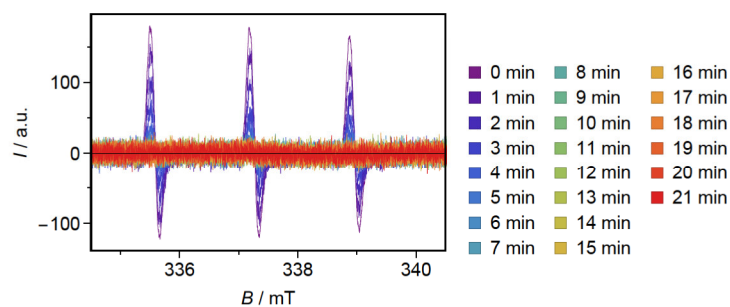


Figure 10.83: EPR spectra of 50 μM TEMPOL + 20 mM Poly EDY-C in TE buffer solution with 6.6 vol% DMSO during irradiation with blue light at 37°C, which were used to calculate the DI shown in Fig. 6.10.

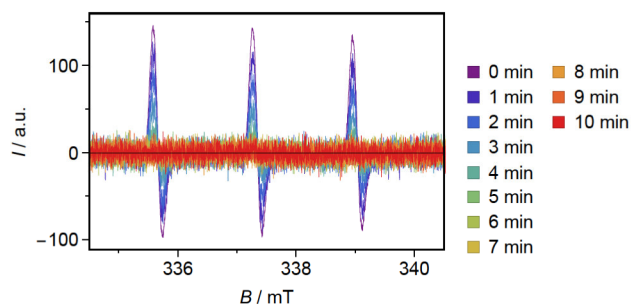


Figure 10.84: EPR spectra of 50 μM TEMPOL + 20 mM Poly EDY-D in TE buffer solution with 6.6 vol% DMSO during irradiation with blue light at 37 °C, which were used to calculate the DI shown in Fig. 6.10.

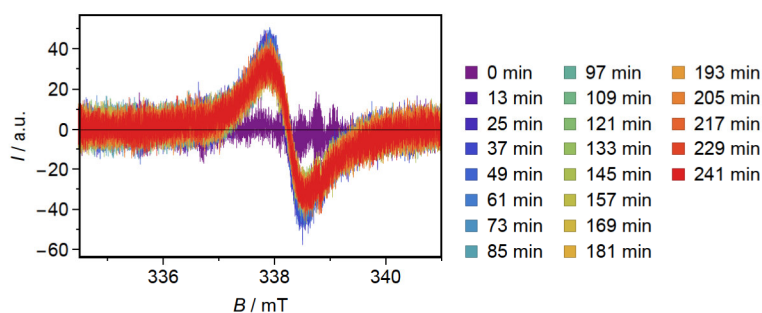


Figure 10.85: EPR spectra of 5.05 mg PIE1, which were used to calculate the DI shown in Fig. 6.11, were recorded after seven days without compression. At $t=0$ min, the temperature was 25 °C. Over the first 8 min, the device heats up to 175 °C and then kept constant at this temperature.

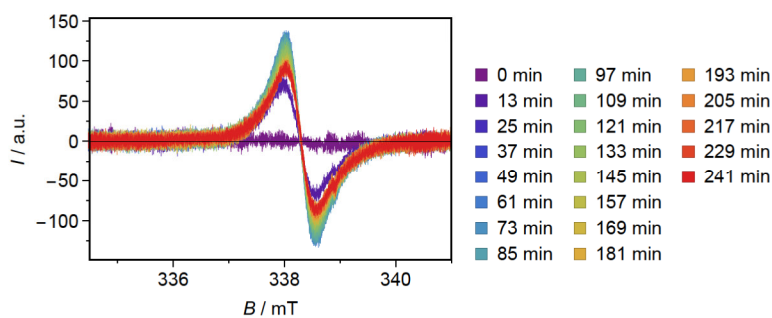


Figure 10.86: EPR spectra of 4.79 mg PIE1, which were used to calculate the DI shown in Fig. 6.11, were recorded after seven days without compression. At $t=0$ min, the temperature was 25 °C. Over the first 8 min, the device heats up to 175 °C and then kept constant at this temperature.

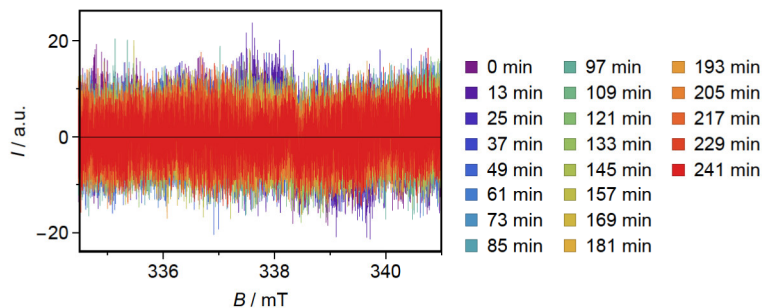


Figure 10.87: EPR spectra of 9.81 mg PIE1, which were used to calculate the DI shown in Fig. 6.11, were recorded after seven days without compression. At $t=0$ min, the temperature was 25 °C. Over the first 8 min, the device heats up to 175 °C and then kept constant at this temperature.

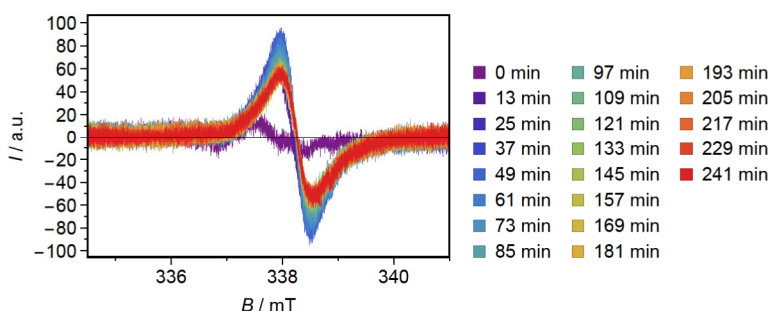


Figure 10.88: EPR spectra of 3.83 mg PIE1, which were used to calculate the DI shown in Fig. 6.11, were recorded after seven days under 10 t of compression. At $t=0$ min, the temperature was 25 °C. Over the first 8 min, the device heats up to 175 °C and then kept constant at this temperature.

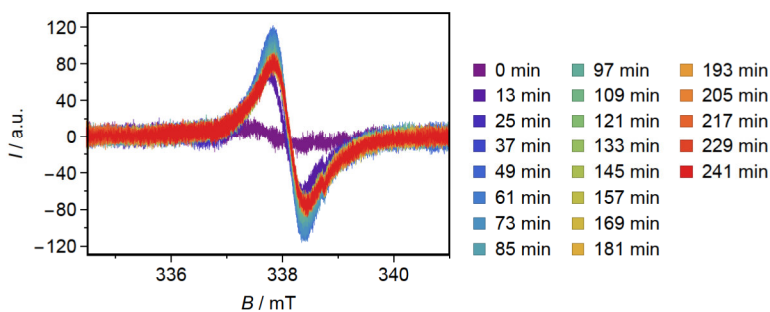


Figure 10.89: EPR spectra of 6.26 mg PIE1, which were used to calculate the DI shown in Fig. 6.11, were recorded after seven days under 10 t of compression. At $t=0$ min, the temperature was 25 °C. Over the first 8 min, the device heats up to 175 °C and then kept constant at this temperature.

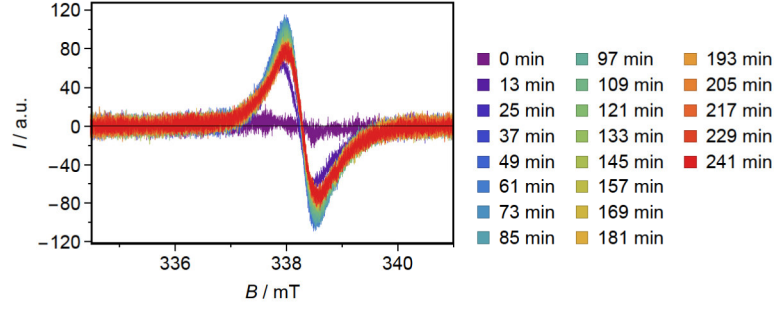


Figure 10.90: EPR spectra of 7.32 mg PIE1, which were used to calculate the DI shown in Fig. 6.11, were recorded after seven days under 10 t of compression. At $t=0$ min, the temperature was 25 °C. Over the first 8 min, the device heats up to 175 °C and then kept constant at this temperature.

Table 10.1: *Easyspin* simulation parameters of the simulated systems shown in Fig. 6.12. The 'freely rotating' and 'slow-motion' simulation are combined to yield the simulated spectrum in Fig. 6.12 (A) and are depicted in Fig. 6.12 (B). The simulated spectrum in 6.12 (C) arises from simulating the 'inhibited motion' parameter.

	freely rotating	slow-motion	inhibited motion
S	1/2	1/2	1/2
$Nucs$	14N	14N	14N
g_{xx}	2.0161041	2.0105764	2.0052606
g_{yy}	1.9993105	2.0018328	2.0069155
g_{zz}	1.9992624	2.0009434	2.0016625
A_{xx}	15.1378790	17.1898764	13.5620290
A_{yy}	13.9692119	5.7892749	19.8817495
A_{zz}	101.6743341	104.7262106	90.5360257
$lwpp$	0.000	0.000	[0.3,0.3]
$logtcorr$	-9.048	-8.279	-6.043

10.5 Investigation of photoresponsive LCST-polymers

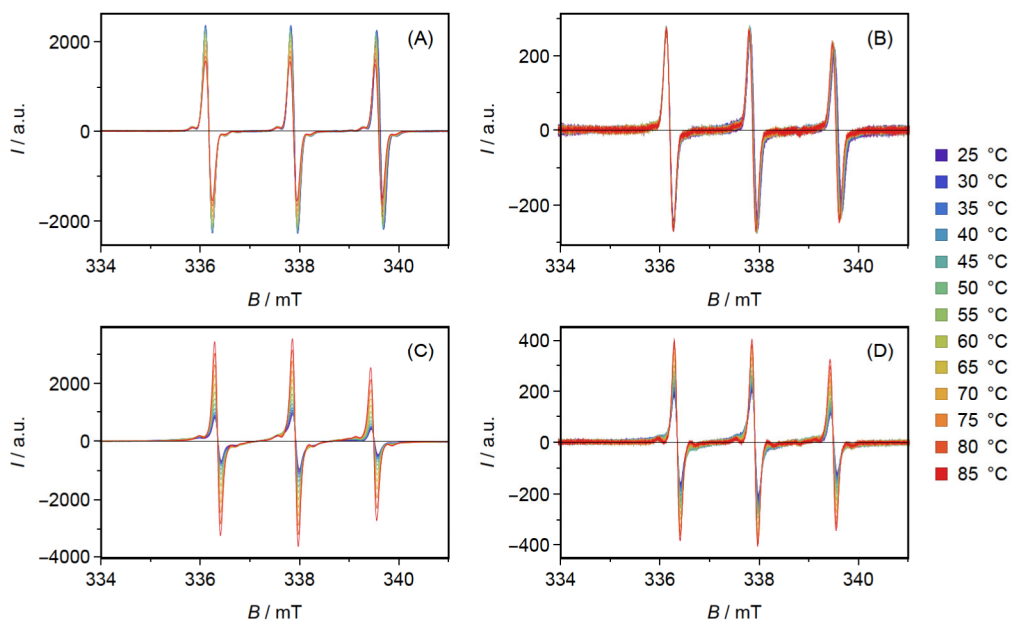


Figure 10.91: Raw EPR spectra of 100 μM TEMPO (A)/TEMPOL-benzoate (B)/5-DSA (C)/16-DSA (D) in 10 mg/ml DMAm-AAPEAm₇ solution while gradually heating from 25 °C to 85 °C in steps of 5 °C.

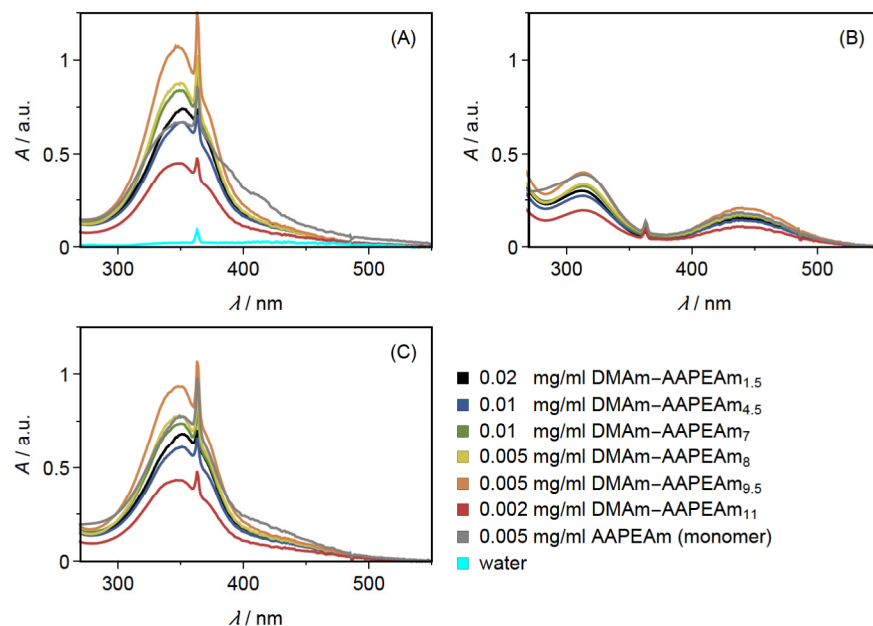


Figure 10.92: UV/vis spectra of DMAM-AAPEAm_x polymers, the AAPEAm monomer and water measured dark (A), after 20 seconds of UV (365 nm) irradiation (B) and, subsequently, after 180 seconds of green light (535 nm) irradiation (C). Water was used as a background and measured again to verify, that the spike at 360 nm is an artifact from the device and not a signal of the samples.

Table 10.2: *Easyspin* simulation parameters of the simulated systems shown in Fig. 7.6. The simulated components ('comp') 'free' and 'bound' are combined according to their proportion χ to yield the final simulated spectrum.

label	comp	$\chi/\%$	g_{iso}	A_{iso}	τ_c/ns
DMAm-AAPEAm _{1.5} (dark)	Free	57.7022	2.00455	44.1904	0.159142
DMAm-AAPEAm _{1.5} (dark)	Bound	42.2978	2.0042	39.9457	1.54232
DMAm-AAPEAm _{1.5} (365 nm)	Free	59.5218	2.00464	44.0729	0.11493
DMAm-AAPEAm _{1.5} (365 nm)	Bound	40.4782	2.00455	38.2784	1.53194
DMAm-AAPEAm _{1.5} (535 nm)	Free	57.7022	2.00466	44.1904	0.159142
DMAm-AAPEAm _{1.5} (535 nm)	Bound	42.2978	2.0042	39.9457	1.54232
DMAm-AAPEAm _{4.5} (dark)	Free	24.0039	2.00462	44.0554	0.133812
DMAm-AAPEAm _{4.5} (dark)	Bound	75.9961	2.00461	37.9728	2.24462
DMAm-AAPEAm _{4.5} (365 nm)	Free	69.4309	2.00462	44.0554	0.125893
DMAm-AAPEAm _{4.5} (365 nm)	Bound	30.5691	2.00461	37.9728	2.24462
DMAm-AAPEAm _{4.5} (535 nm)	Free	24.0039	2.00462	44.0554	0.133812
DMAm-AAPEAm _{4.5} (535 nm)	Bound	75.9961	2.00461	37.9728	2.24462
DMAm-AAPEAm ₇ (dark)	Free	17.9199	2.00466	44.11	0.158718
DMAm-AAPEAm ₇ (dark)	Bound	82.0801	2.00464	42.721	2.98414
DMAm-AAPEAm ₇ (365 nm)	Free	66.6667	2.00463	44.1939	0.158489
DMAm-AAPEAm ₇ (365 nm)	Bound	33.3333	2.00474	41.0565	2.51189
DMAm-AAPEAm ₇ (535 nm)	Free	23.5102	2.00466	44.11	0.158718
DMAm-AAPEAm ₇ (535 nm)	Bound	76.4898	2.00464	42.721	2.98414
DMAm-AAPEAm ₈ (dark)	Free	11.2936	2.00438	44.0597	0.245471
DMAm-AAPEAm ₈ (dark)	Bound	88.7064	2.00438	42.8438	4.43295
DMAm-AAPEAm ₈ (365 nm)	Free	71.8015	2.00438	44.0597	0.199526
DMAm-AAPEAm ₈ (365 nm)	Bound	28.1985	2.00438	42.8438	4.43295
DMAm-AAPEAm ₈ (535 nm)	Free	11.2936	2.00438	44.0597	0.245471
DMAm-AAPEAm ₈ (535 nm)	Bound	88.7064	2.00438	42.8438	4.43295
DMAm-AAPEAm _{9.5} (dark)	Free	12.3929	2.00438	44.0597	0.209371
DMAm-AAPEAm _{9.5} (dark)	Bound	87.6071	2.00438	42.8438	4.43295
DMAm-AAPEAm _{9.5} (365 nm)	Free	67.9683	2.00438	44.0597	0.209371
DMAm-AAPEAm _{9.5} (365 nm)	Bound	32.0317	2.00438	42.8438	4.43295
DMAm-AAPEAm _{9.5} (535 nm)	Free	12.3929	2.00438	44.0597	0.209371
DMAm-AAPEAm _{9.5} (535 nm)	Bound	87.6071	2.00438	42.8438	4.43295
DMAm-AAPEAm ₁₁ (dark)	Free	17.0363	2.00438	44.0597	0.204174
DMAm-AAPEAm ₁₁ (dark)	Bound	82.9637	2.00438	42.8438	4.43295
DMAm-AAPEAm ₁₁ (365 nm)	Free	72.6206	2.00438	44.0597	0.165959
DMAm-AAPEAm ₁₁ (365 nm)	Bound	27.3794	2.00438	42.8438	4.43295
DMAm-AAPEAm ₁₁ (535 nm)	Free	19.0786	2.00438	44.0597	0.204174
DMAm-AAPEAm ₁₁ (535 nm)	Bound	80.9214	2.00438	42.8438	4.43295

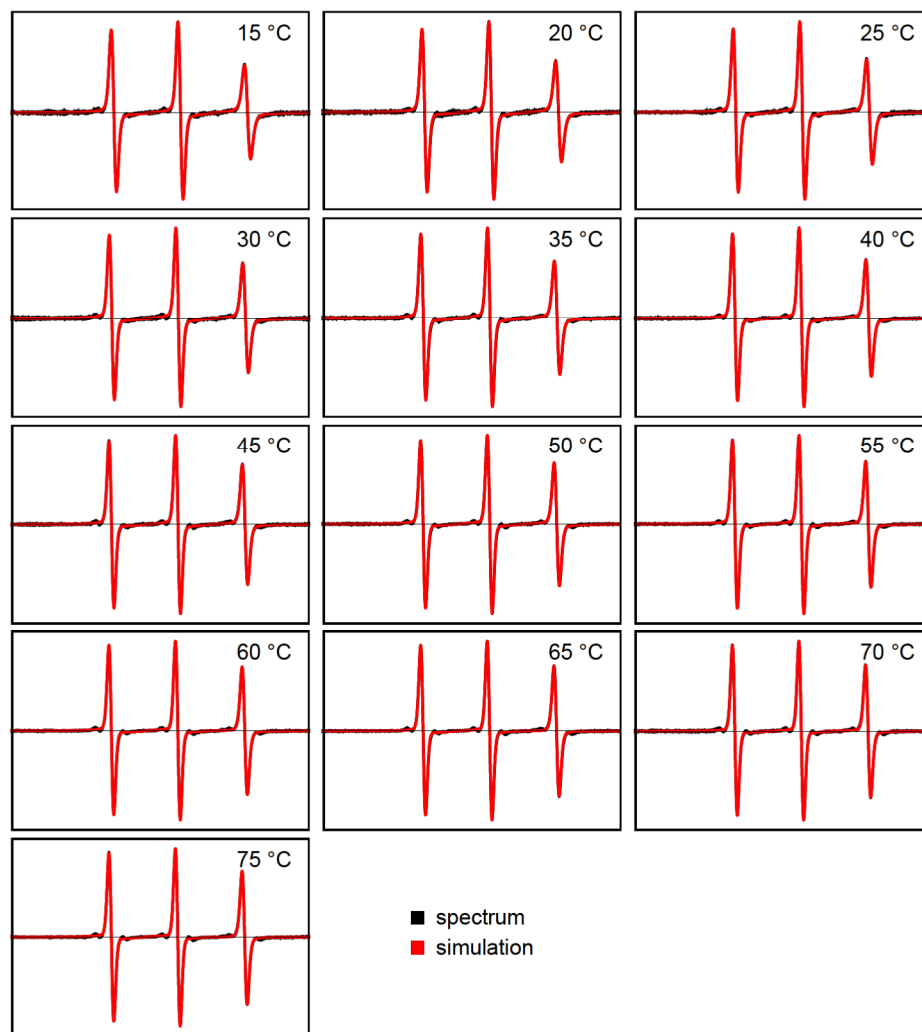


Figure 10.93: EPR spectra (black) and the *easyspin* EPR spectrum simulations (red) of 10 mg/ml DMAM-AAPEAm_{1.5} with 100 μ M 5-DSA recorded in darkness and at different temperatures. Each simulated spectrum is a combination of two spin systems; one fast rotating nitroxide radical and one slower rotating nitroxide radical, which is considered to be polymer-bound. The simulation parameters are listed in Tab. 10.3.

Table 10.3: *Easyspin* simulation parameters of the simulated systems shown in Fig. 10.93. The 'free' and 'bound' simulations at one temperature are combined to yield the final simulated spectrum.

$T/^{\circ}\text{C}$	component	proportion/%	g_{iso}	A_{iso}	τ_c/ns
15	Free	56.6384	2.0045	44.1732	0.229174
15	Bound	43.3616	2.00401	40.1251	1.82039
20	Free	54.5598	2.00446	44.2152	0.133652
20	Bound	45.4402	2.00417	39.3736	2.32012
25	Free	54.6908	2.00455	44.1904	0.159142
25	Bound	45.3092	2.0042	39.9457	1.54232
30	Free	55.4221	2.0046	44.1105	0.15195
30	Bound	44.5779	2.00431	39.2122	2.1813
35	Free	55.7009	2.00461	44.1108	0.113823
35	Bound	44.2991	2.00447	39.2073	2.24195
40	Free	55.3685	2.00461	44.061	0.121378
40	Bound	44.6315	2.0043	39.7096	1.4972
45	Free	57.4817	2.00464	44.0703	0.132337
45	Bound	42.5183	2.00433	40.4893	1.62205
50	Free	56.8454	2.00461	44.0137	0.0946991
50	Bound	43.1546	2.00441	39.6177	1.93487
55	Free	57.3473	2.00464	44.0104	0.0884371
55	Bound	42.6527	2.00453	38.4606	1.98619
60	Free	54.1732	2.00465	44.0241	0.0735744
60	Bound	45.8268	2.00489	36.2142	1.76433
65	Free	66.3647	2.00465	43.9462	0.110936
65	Bound	33.6353	2.00441	39.6889	2.57187
70	Free	60.5015	2.00468	43.9361	0.0985793
70	Bound	39.4985	2.00451	39.2597	1.28593
75	Free	58.0941	2.00464	43.9246	0.0726897
75	Bound	41.9059	2.00464	38.4425	2.65703

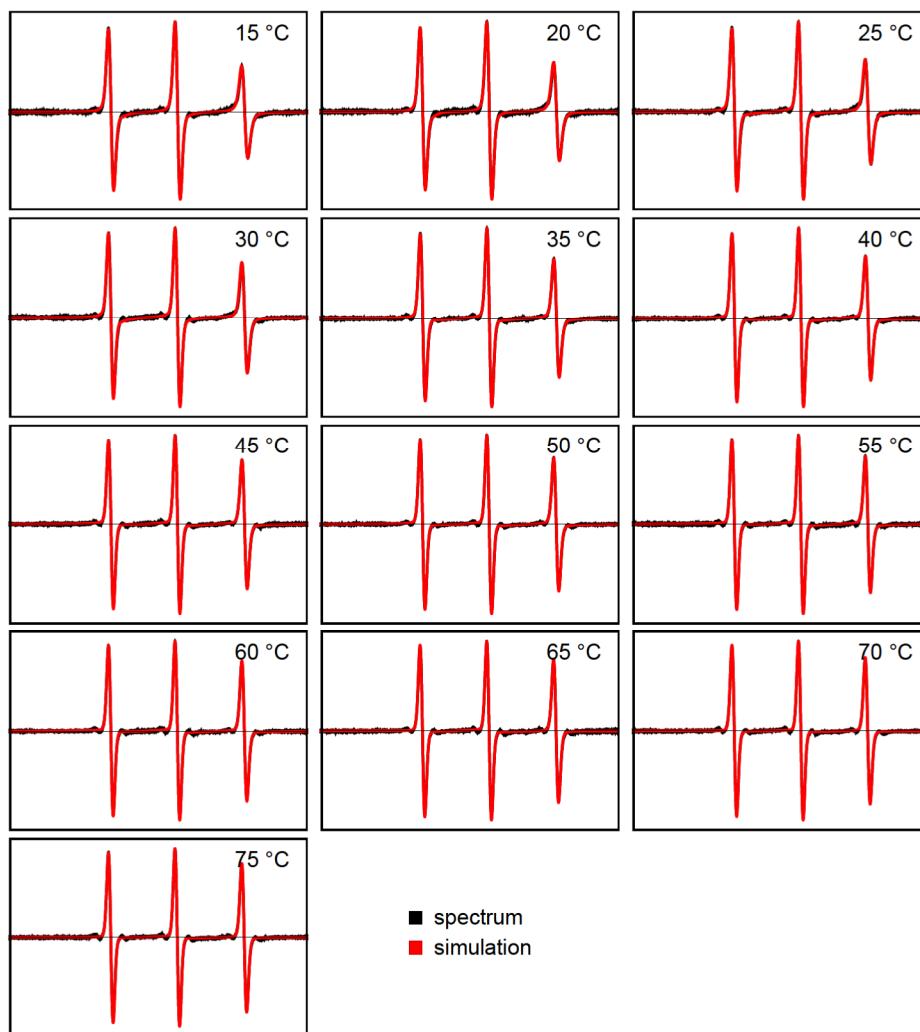


Figure 10.94: EPR spectra (black) and the *easyspin* EPR spectrum simulations (red) of 10 mg/ml DMAM-AAPEAm_{1.5} with 100 μ M 5-DSA recorded during UV irradiation (365 nm) and at different temperatures. Each simulated spectrum is a combination of two spin systems; one fast rotating nitroxide radical and one slower rotating nitroxide radical, which is considered to be polymer-bound. The simulation parameters are listed in Tab. 10.4.

Table 10.4: *Easyspin* simulation parameters of the simulated systems shown in Fig. 10.94. The 'free' and 'bound' simulations at one temperature are combined to yield the final simulated spectrum.

$T/^{\circ}\text{C}$	component	proportion/%	g_{iso}	A_{iso}	τ_c/ns
15	Free	70.0888	2.0046	44.0657	0.171095
15	Bound	29.9112	2.00418	41.5017	1.46384
20	Free	74.4602	2.00461	44.091	0.151762
20	Bound	25.5398	2.00447	41.063	0.858067
25	Free	59.5218	2.00464	44.0729	0.11493
25	Bound	40.4782	2.00455	38.2784	1.53194
30	Free	64.4528	2.00462	44.0554	0.11224
30	Bound	35.5472	2.00456	40.3465	1.09727
35	Free	59.0199	2.00464	44.1009	0.121382
35	Bound	40.9801	2.00413	38.9512	1.83413
40	Free	55.4652	2.00463	44.0507	0.135218
40	Bound	44.5348	2.0039	38.6847	1.727
45	Free	50.6164	2.00464	44.0455	0.11704
45	Bound	49.3836	2.00428	35.2511	3.08204
50	Free	50.4531	2.00465	44.0408	0.0840817
50	Bound	49.5469	2.00399	35.8717	2.79197
55	Free	49.223	2.00465	44.0333	0.0976834
55	Bound	50.777	2.00413	34.9088	2.90963
60	Free	45.6868	2.00467	44.003	0.087803
60	Bound	54.3132	2.00439	36.072	2.4094
65	Free	52.1828	2.00466	44.0181	0.0564152
65	Bound	47.8172	2.00442	43.7196	4.03001
70	Free	58.709	2.00467	43.9799	0.072204
70	Bound	41.291	2.00432	40.0308	3.88215
75	Free	56.5083	2.00466	43.9951	0.0656154
75	Bound	43.4917	2.00422	45.6193	3.7902

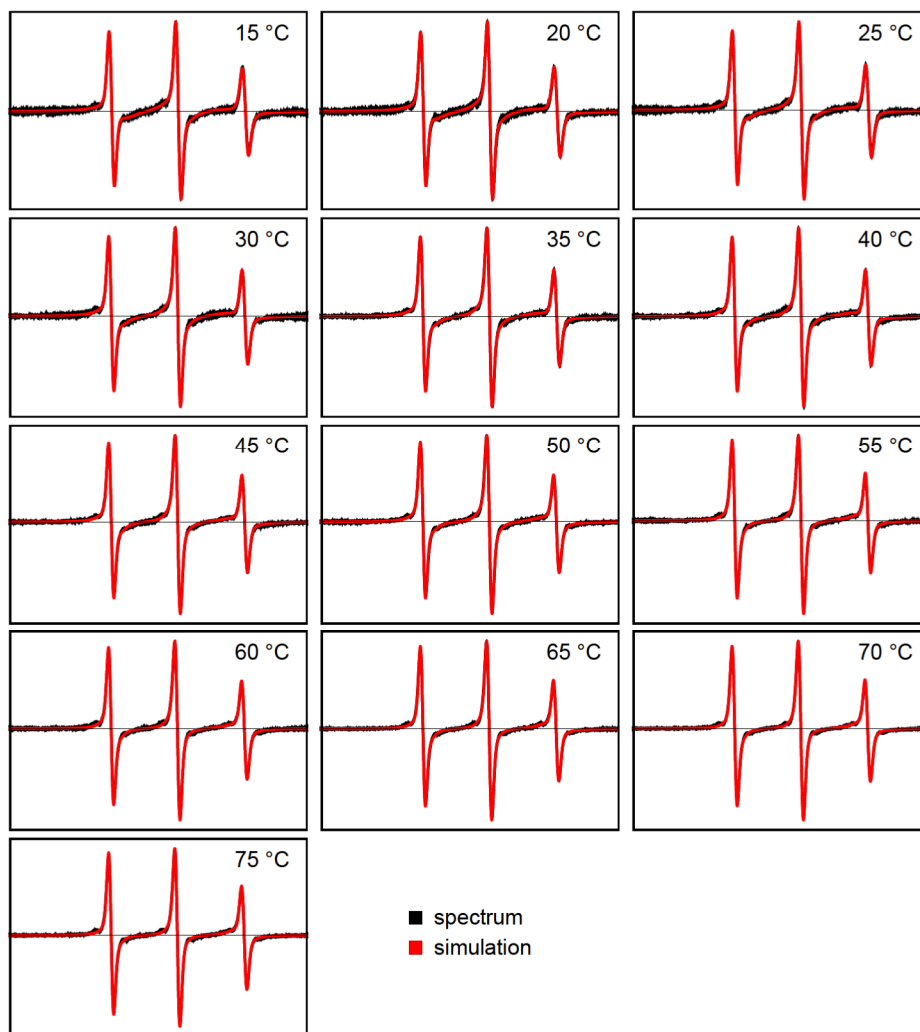


Figure 10.95: EPR spectra (black) and the *easyspin* EPR spectrum simulations (red) of 10 mg/ml DMAM-AAPEAm_{4,5} with 100 μ M 5-DSA recorded in darkness and at different temperatures. Each simulated spectrum is a combination of two spin systems; one fast rotating nitroxide radical and one slower rotating nitroxide radical, which is considered to be polymer-bound. The simulation parameters are listed in Tab. 10.5.

Table 10.5: *Easyspin* simulation parameters of the simulated systems shown in Fig. 10.95. The 'free' and 'bound' simulations at one temperature are combined to yield the final simulated spectrum.

$T/^{\circ}\text{C}$	component	proportion/%	g_{iso}	A_{iso}	τ_c/ns
15	Free	30.7994	2.00462	44.1988	0.145676
15	Bound	69.2006	2.00455	42.3238	2.16577
20	Free	30.5133	2.00449	44.1584	0.17575
20	Bound	69.4867	2.00438	42.9413	2.07191
25	Free	31.1181	2.00453	44.1009	0.119322
25	Bound	68.8819	2.00451	42.7384	1.99896
30	Free	30.68	2.00455	44.0504	0.145754
30	Bound	69.32	2.00455	42.8992	1.944
35	Free	31.4925	2.00456	44.1137	0.126017
35	Bound	68.5075	2.00458	42.6933	2.46884
40	Free	32.1078	2.00456	44.0881	0.130444
40	Bound	67.8922	2.00455	42.7468	2.3583
45	Free	32.718	2.00457	44.0352	0.107932
45	Bound	67.282	2.00459	43.084	1.51902
50	Free	33.5607	2.00457	44.0389	0.118009
50	Bound	66.4393	2.00463	42.4739	1.45599
55	Free	32.3593	2.00458	44.053	0.0811171
55	Bound	67.6407	2.00468	42.9774	1.50652
60	Free	38.2635	2.00459	43.9616	0.121268
60	Bound	61.7365	2.00466	42.8793	1.31181
65	Free	35.8133	2.00459	43.9261	0.086288
65	Bound	64.1867	2.00466	42.7653	1.29273
70	Free	37.7316	2.00461	43.898	0.0804596
70	Bound	62.2684	2.0047	42.6094	1.13263
75	Free	39.3296	2.00463	43.8824	0.0979464
75	Bound	60.6704	2.00469	42.6232	1.23488

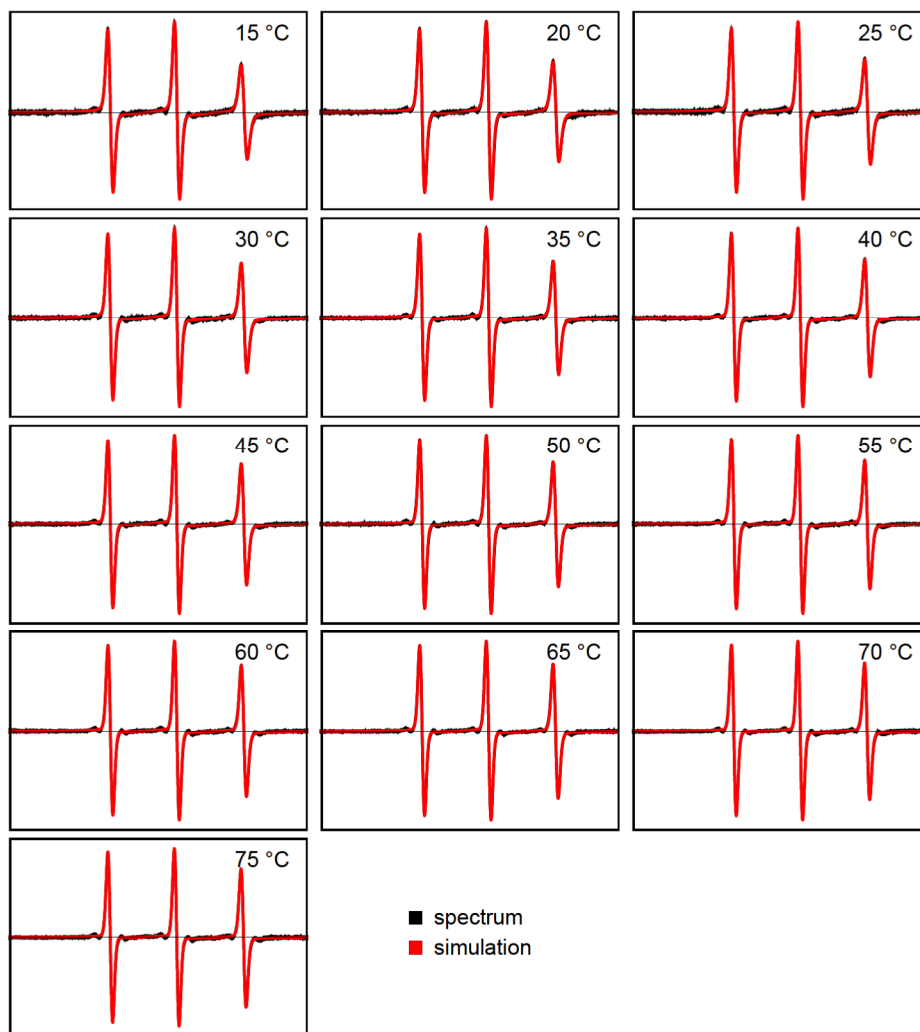


Figure 10.96: EPR spectra (black) and the *easyspin* EPR spectrum simulations (red) of 10 mg/ml DMAM-AAPEAm_{4,5} with 100 μ M 5-DSA recorded during UV irradiation (365 nm) and at different temperatures. Each simulated spectrum is a combination of two spin systems; one fast rotating nitroxide radical and one slower rotating nitroxide radical, which is considered to be polymer-bound. The simulation parameters are listed in Tab. 10.6.

Table 10.6: *Easyspin* simulation parameters of the simulated systems shown in Fig. 10.96. The 'free' and 'bound' simulations at one temperature are combined to yield the final simulated spectrum.

$T/^{\circ}\text{C}$	component	proportion/%	g_{iso}	A_{iso}	τ_c/ns
15	Free	40.9732	2.00454	44.1391	0.135144
15	Bound	59.0268	2.00393	37.7976	2.18456
20	Free	42.0401	2.00457	44.0813	0.181892
20	Bound	57.9599	2.00412	37.5949	2.68494
25	Free	39.4274	2.00456	44.0924	0.13629
25	Bound	60.5726	2.00427	33.8421	3.10694
30	Free	39.954	2.00456	44.1022	0.109055
30	Bound	60.046	2.00448	33.6621	3.02769
35	Free	40.508	2.00456	44.0509	0.11462
35	Bound	59.492	2.00434	33.5931	3.11473
40	Free	41.8003	2.00456	44.0458	0.0918573
40	Bound	58.1997	2.00419	35.6889	2.43877
45	Free	40.6316	2.00459	44.0286	0.145565
45	Bound	59.3684	2.00433	33.6091	2.69312
50	Free	42.8173	2.00456	44.0278	0.0967608
50	Bound	57.1827	2.00416	34.4103	2.72395
55	Free	42.8526	2.00458	43.9721	0.062622
55	Bound	57.1474	2.00435	33.5009	2.71468
60	Free	42.3166	2.00459	44.0069	0.109532
60	Bound	57.6834	2.00432	33.7808	2.76716
65	Free	44.1292	2.00459	43.9805	0.0586667
65	Bound	55.8708	2.00417	34.3601	2.46807
70	Free	42.646	2.0046	43.9276	0.0768426
70	Bound	57.354	2.00429	31.6905	2.78655
75	Free	42.2824	2.00461	43.9023	0.0786175
75	Bound	57.7176	2.00448	31.9832	3.09549

Table 10.7: *Easyspin* simulation parameters of the simulated systems shown in Fig. 7.9. The 'free' and 'bound' simulations at one temperature are combined to yield the final simulated spectrum.

$T/^{\circ}\text{C}$	component	proportion/%	g_{iso}	A_{iso}	τ_c/ns
15	Free	15.2383	2.00463	44.1484	0.155451
15	Bound	84.7617	2.00463	42.2149	2.95221
20	Free	15.3829	2.00468	44.0829	0.258759
20	Bound	84.6171	2.00464	42.5924	3.09737
25	Free	15.0033	2.00468	44.0723	0.16908
25	Bound	84.9967	2.00466	42.7628	2.93354
30	Free	14.8993	2.00468	44.0571	0.159546
30	Bound	85.1007	2.00469	42.7251	2.81391
35	Free	14.9979	2.0047	44.041	0.214093
35	Bound	85.0021	2.00471	42.9834	2.70162
40	Free	15.6275	2.00471	44.0728	0.174859
40	Bound	84.3725	2.00472	43.0956	2.81536
45	Free	16.4069	2.00469	43.9908	0.163031
45	Bound	83.5931	2.00472	42.6806	2.54962
50	Free	17.8325	2.0047	43.9979	0.141254
50	Bound	82.1675	2.00478	42.6702	2.20222
55	Free	20.0734	2.00469	44.0175	0.0830192
55	Bound	79.9266	2.00474	42.2404	2.32541
60	Free	23.1946	2.0047	44.0081	0.0799121
60	Bound	76.8054	2.00479	42.1632	2.25804
65	Free	25.7565	2.00472	44.0014	0.0938898
65	Bound	74.2435	2.00483	42.4542	1.52894
70	Free	29.2612	2.00472	43.9553	0.123674
70	Bound	70.7388	2.00476	41.7591	1.7629
75	Free	33.2013	2.00473	43.9387	0.105005
75	Bound	66.7987	2.00482	41.7568	1.76632

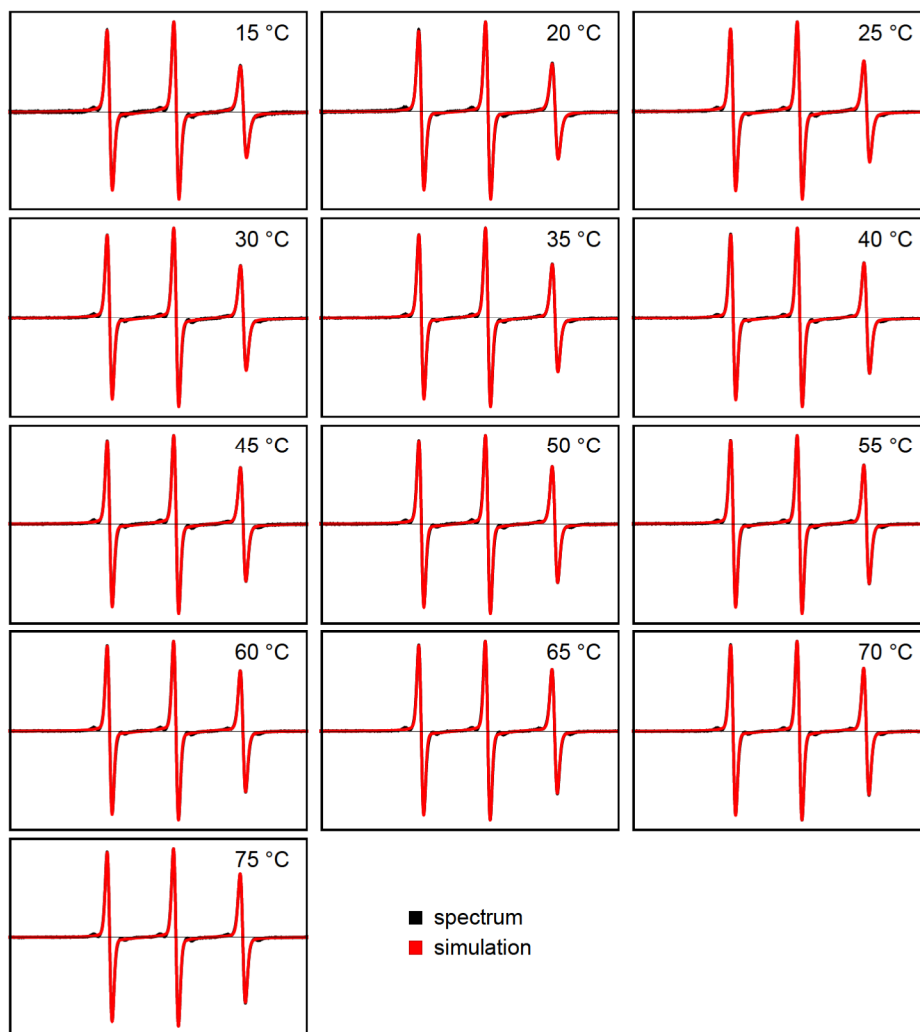


Figure 10.97: EPR spectra (black) and the *easyspin* EPR spectrum simulations (red) of 10 mg/ml DMAM-AAPEAm₇ with 100 μ M 5-DSA recorded during UV irradiation (365 nm) and at different temperatures. Each simulated spectrum is a combination of two spin systems; one fast rotating nitroxide radical and one slower rotating nitroxide radical, which is considered to be polymer-bound. The simulation parameters are listed in Tab. 10.8.

Table 10.8: *Easyspin* simulation parameters of the simulated systems shown in Fig. 10.97. The 'free' and 'bound' simulations at one temperature are combined to yield the final simulated spectrum.

$T/^{\circ}\text{C}$	component	proportion/%	g_{iso}	A_{iso}	τ_c/ns
15	Free	40.0777	2.00464	44.0693	0.220342
15	Bound	59.9223	2.00449	35.8612	2.7283
20	Free	53.011	2.00465	44.054	0.168784
20	Bound	46.989	2.00449	35.8612	2.7283
25	Free	39.1924	2.00466	44.0988	0.117442
25	Bound	60.8076	2.00478	35.7353	2.70585
30	Free	40.3497	2.00469	44.0651	0.204971
30	Bound	59.6503	2.00459	37.9632	1.89471
35	Free	39.4978	2.00468	44.0589	0.145693
35	Bound	60.5022	2.0046	37.8868	1.71536
40	Free	44.7664	2.00468	44.0279	0.144794
40	Bound	55.2336	2.00454	39.429	1.88878
45	Free	44.7671	2.00468	44.01	0.0924839
45	Bound	55.2329	2.00469	37.8619	2.30539
50	Free	45.5664	2.00468	43.9819	0.095647
50	Bound	54.4336	2.00464	38.8836	1.68167
55	Free	46.4994	2.0047	43.9889	0.101489
55	Bound	53.5006	2.00475	38.8053	1.6803
60	Free	49.4155	2.00469	43.9153	0.0748079
60	Bound	50.5845	2.0047	38.9989	1.72242
65	Free	50.2746	2.00472	43.9125	0.116937
65	Bound	49.7254	2.00467	39.9646	1.23348
70	Free	51.8886	2.00471	43.9276	0.0903553
70	Bound	48.1114	2.00463	39.5545	1.51068
75	Free	57.4298	2.00471	43.95	0.0611608
75	Bound	42.5702	2.0047	40.0677	1.3327

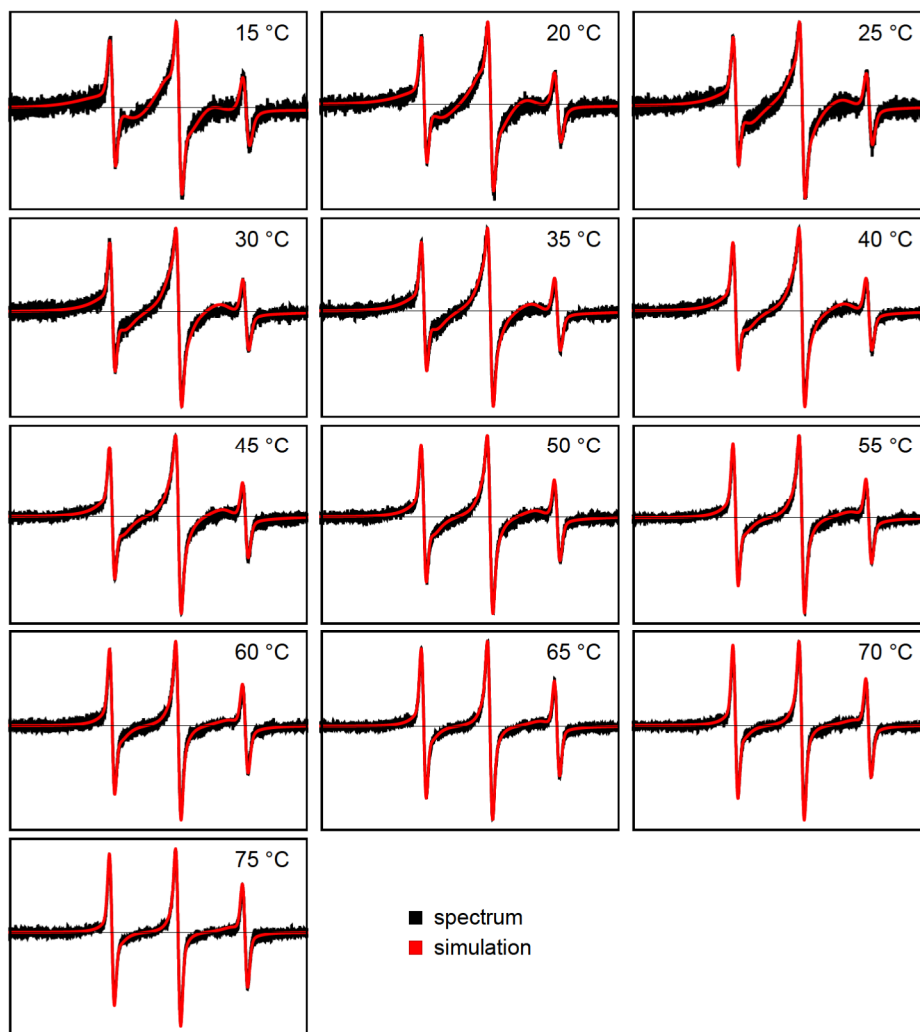


Figure 10.98: EPR spectra (black) and the *easyspin* EPR spectrum simulations (red) of 10 mg/ml DMAM-AAPEAm₈ with 100 μ M 5-DSA recorded in darkness and at different temperatures. Each simulated spectrum is a combination of two spin systems; one fast rotating nitroxide radical and one slower rotating nitroxide radical, which is considered to be polymer-bound. The simulation parameters are listed in Tab. 10.9.

Table 10.9: *Easyspin* simulation parameters of the simulated systems shown in Fig. 10.98. The 'free' and 'bound' simulations at one temperature are combined to yield the final simulated spectrum.

$T/^{\circ}\text{C}$	component	proportion/%	g_{iso}	A_{iso}	τ_c/ns
15	Free	10.1513	2.00452	44.051	0.269672
15	Bound	89.8487	2.00445	39.1195	3.29945
20	Free	11.7397	2.00453	44.0345	0.213294
20	Bound	88.2603	2.00451	40.8412	3.37203
25	Free	11.3721	2.00455	44.0721	0.25802
25	Bound	88.6279	2.00454	42.8746	2.96563
30	Free	11.7075	2.00452	44.0042	0.156575
30	Bound	88.2925	2.00457	42.9736	3.42201
35	Free	12.0255	2.00455	44.0247	0.139316
35	Bound	87.9745	2.00461	42.8713	3.61303
40	Free	12.8306	2.00454	43.9969	0.129064
40	Bound	87.1694	2.00462	42.7857	3.40414
45	Free	13.6377	2.00455	43.9514	0.131983
45	Bound	86.3623	2.00464	42.7031	3.24432
50	Free	16.1413	2.00457	43.9335	0.174216
50	Bound	83.8587	2.00466	42.5477	3.11282
55	Free	18.3599	2.00456	43.9553	0.14973
55	Bound	81.6401	2.00465	42.6396	2.09101
60	Free	22.0442	2.00455	43.9454	0.143685
60	Bound	77.9558	2.00465	42.3583	1.8925
65	Free	23.4479	2.00458	43.9496	0.0678209
65	Bound	76.5521	2.00467	42.889	2.85554
70	Free	25.5026	2.00459	43.8833	0.0977534
70	Bound	74.4974	2.00472	42.3277	1.45599
75	Free	28.465	2.00458	43.9135	0.0742677
75	Bound	71.535	2.00472	42.383	1.24736

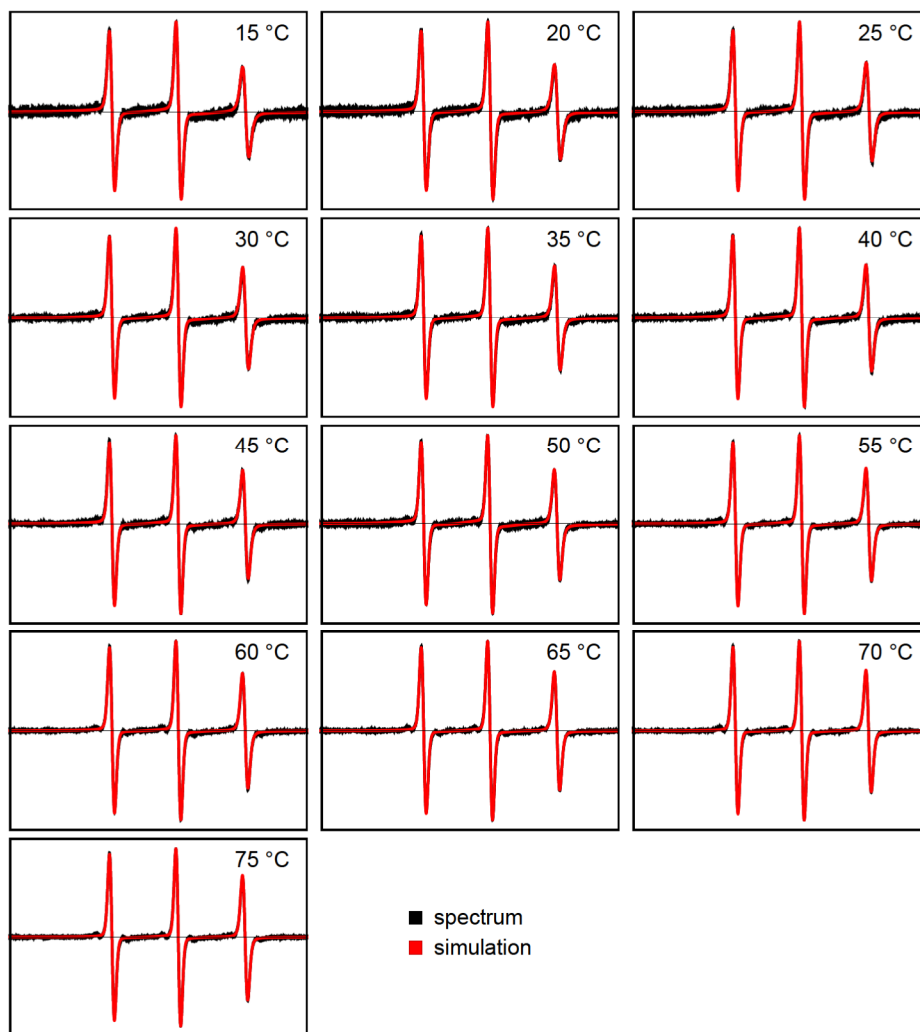


Figure 10.99: EPR spectra (black) and the *easyspin* EPR spectrum simulations (red) of 10 mg/ml DMAM-AAPEAm₈ with 100 μ M 5-DSA recorded during UV irradiation (365 nm) and at different temperatures. Each simulated spectrum is a combination of two spin systems; one fast rotating nitroxide radical and one slower rotating nitroxide radical, which is considered to be polymer-bound. The simulation parameters are listed in Tab. 10.10.

Table 10.10: *Easyspin* simulation parameters of the simulated systems shown in Fig. 10.99. The 'free' and 'bound' simulations at one temperature are combined to yield the final simulated spectrum.

$T/^{\circ}\text{C}$	component	proportion/%	g_{iso}	A_{iso}	τ_c/ns
15	Free	35.468	2.00446	44.0736	0.160365
15	Bound	64.532	2.00421	33.8184	3.5478
20	Free	36.699	2.00448	44.0695	0.240507
20	Bound	63.301	2.00431	33.334	3.30307
25	Free	37.421	2.0045	44.0488	0.190198
25	Bound	62.579	2.00437	33.3334	3.19532
30	Free	38.882	2.00449	44.0843	0.161095
30	Bound	61.118	2.00441	33.3334	3.0302
35	Free	39.715	2.00449	44.0306	0.131702
35	Bound	60.285	2.00451	33.3423	3.00643
40	Free	41.022	2.00451	43.9728	0.110632
40	Bound	58.978	2.00452	33.3374	2.97855
45	Free	42.898	2.00451	44.0248	0.111814
45	Bound	57.102	2.00457	33.6131	2.67071
50	Free	44.774	2.00452	43.9971	0.131491
50	Bound	55.226	2.00455	33.3333	2.57136
55	Free	47.48	2.00452	43.9591	0.0939575
55	Bound	52.52	2.00451	33.7653	2.73042
60	Free	49.374	2.00453	43.911	0.11144
60	Bound	50.626	2.00471	33.959	2.57134
65	Free	52.695	2.00452	43.8948	0.0849815
65	Bound	47.305	2.00462	35.792	2.29044
70	Free	56.022	2.00455	43.8836	0.103353
70	Bound	43.978	2.00462	35.3037	2.12255
75	Free	58.208	2.00455	43.9016	0.101629
75	Bound	41.792	2.00464	36.1898	1.98075

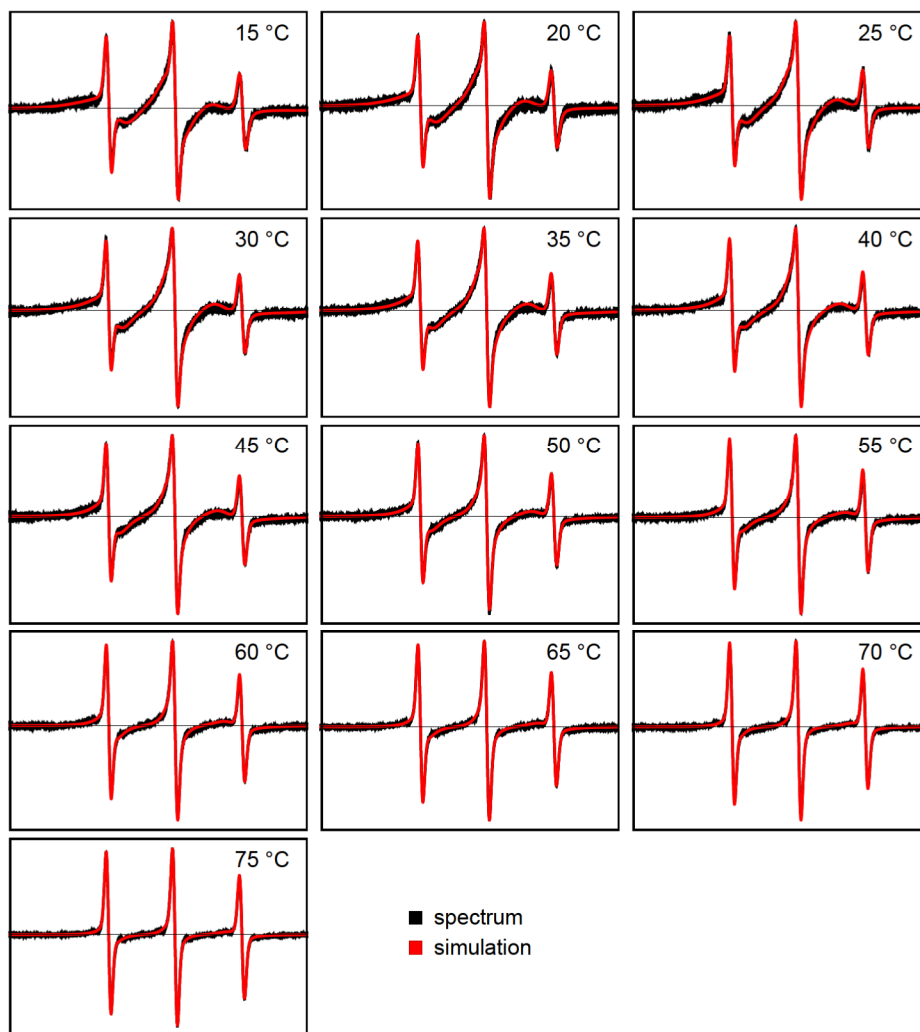


Figure 10.100: EPR spectra (black) and the *easyspin* EPR spectrum simulations (red) of 10 mg/ml DMAM-AAPEAm_{9.5} with 100 μ M 5-DSA recorded in darkness and at different temperatures. Each simulated spectrum is a combination of two spin systems; one fast rotating nitroxide radical and one slower rotating nitroxide radical, which is considered to be polymer-bound. The simulation parameters are listed in Tab. 10.11.

Table 10.11: *Easyspin* simulation parameters of the simulated systems shown in Fig. 10.100. The 'free' and 'bound' simulations at one temperature are combined to yield the final simulated spectrum.

$T/^{\circ}\text{C}$	component	proportion/%	g_{iso}	A_{iso}	τ_c/ns
15	Free	11.8347	2.00461	44.1506	0.167428
15	Bound	88.1653	2.00456	42.8579	3.65453
20	Free	11.2565	2.0046	44.1074	0.163291
20	Bound	88.7435	2.00462	42.5138	3.65966
25	Free	11.1914	2.0046	44.0877	0.130943
25	Bound	88.8086	2.00463	42.734	3.70919
30	Free	11.0644	2.0046	44.0603	0.133328
30	Bound	88.9356	2.00467	42.5995	3.70829
35	Free	11.277	2.00459	44.0136	0.145209
35	Bound	88.723	2.00465	42.5394	3.50317
40	Free	12.3196	2.00458	44.0309	0.111391
40	Bound	87.6804	2.00467	42.5217	3.44165
45	Free	14.3287	2.00458	44.0287	0.1328
45	Bound	85.6713	2.00467	42.268	3.05056
50	Free	16.59	2.00458	44.0367	0.137064
50	Bound	83.41	2.00464	42.6144	2.78561
55	Free	19.4137	2.00459	44.0565	0.0750316
55	Bound	80.5863	2.00472	42.1862	2.2829
60	Free	23.9227	2.00457	44.0227	0.0797244
60	Bound	76.0773	2.00469	42.2628	2.34013
65	Free	28.9055	2.00458	43.9655	0.108969
65	Bound	71.0945	2.00468	42.1881	1.70117
70	Free	36.1522	2.0046	43.9908	0.0550695
70	Bound	63.8478	2.00474	42.2336	1.29012
75	Free	41.4974	2.00461	43.991	0.0810935
75	Bound	58.5026	2.00474	41.4204	2.09446

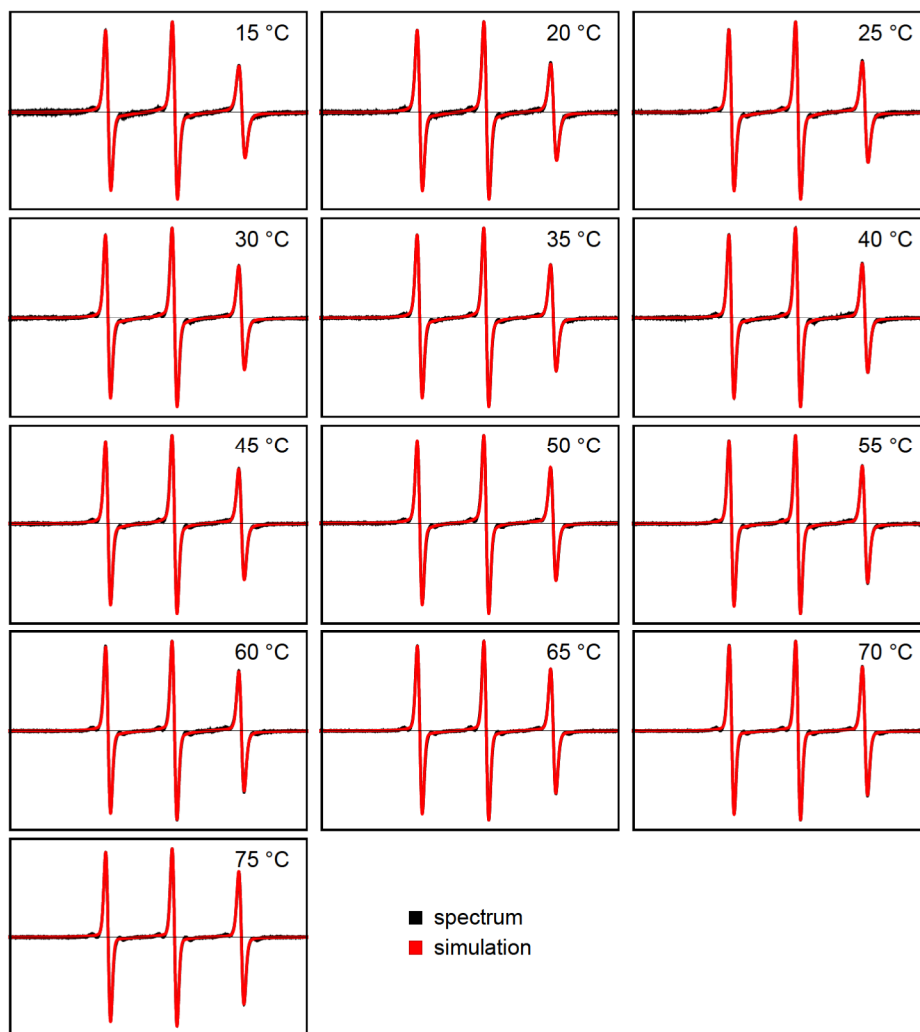


Figure 10.101: EPR spectra (black) and the *easyspin* EPR spectrum simulations (red) of 10 mg/ml DMAM-AAPEAm_{9.5} with 100 μ M 5-DSA recorded during UV irradiation (365 nm) and at different temperatures. Each simulated spectrum is a combination of two spin systems; one fast rotating nitroxide radical and one slower rotating nitroxide radical, which is considered to be polymer-bound. The simulation parameters are listed in Tab. 10.12.

Table 10.12: *Easyspin* simulation parameters of the simulated systems shown in Fig. 10.101. The 'free' and 'bound' simulations at one temperature are combined to yield the final simulated spectrum.

$T/^{\circ}\text{C}$	component	proportion/%	g_{iso}	A_{iso}	τ_c/ns
15	Free	47.5942	2.00461	44.1532	0.170939
15	Bound	52.4058	2.00443	40.9102	1.87007
20	Free	47.7499	2.00461	44.1166	0.246328
20	Bound	52.2501	2.00437	40.7545	1.83651
25	Free	47.1878	2.00461	44.0944	0.174317
25	Bound	52.8122	2.00444	40.6277	1.94362
30	Free	49.2641	2.00459	44.0873	0.109655
30	Bound	50.7359	2.00461	40.4659	2.30233
35	Free	51.1599	2.00462	44.0592	0.1509
35	Bound	48.8401	2.0046	41.0887	1.56021
40	Free	49.1826	2.00463	44.057	0.141019
40	Bound	50.8174	2.00457	40.7876	1.55632
45	Free	51.2434	2.0046	43.9819	0.0986455
45	Bound	48.7566	2.00463	40.5846	1.36949
50	Free	53.8626	2.00462	44.0142	0.123383
50	Bound	46.1374	2.00476	40.7534	1.80971
55	Free	50.7093	2.00461	43.9963	0.121528
55	Bound	49.2907	2.00468	40.2788	1.65723
60	Free	51.2363	2.00462	43.9814	0.139965
60	Bound	48.7637	2.00456	40.5426	1.48326
65	Free	54.6199	2.0046	43.9822	0.0789647
65	Bound	45.3801	2.00463	40.393	1.26482
70	Free	53.9401	2.00461	43.9757	0.0823955
70	Bound	46.0599	2.00461	39.9608	1.28478
75	Free	54.0286	2.00462	43.9006	0.0634733
75	Bound	45.9714	2.00475	38.6623	1.78317

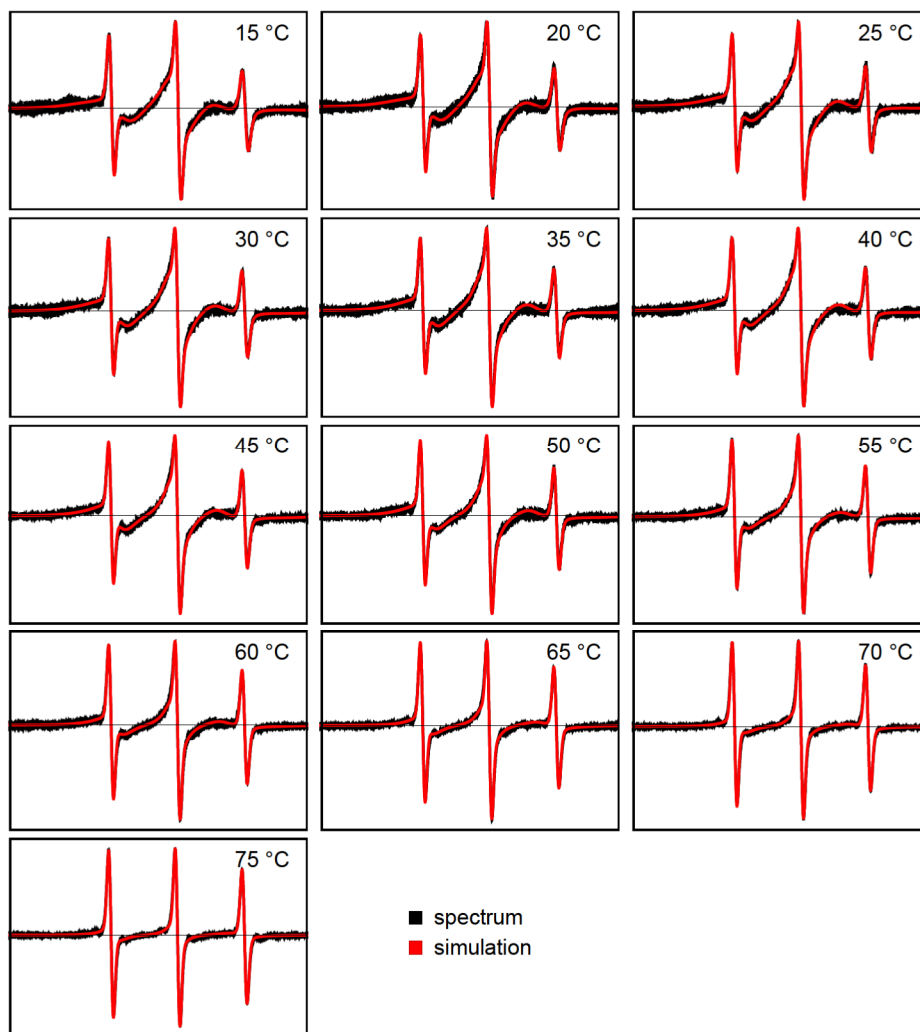


Figure 10.102: EPR spectra (black) and the *easyspin* EPR spectrum simulations (red) of 10 mg/ml DMAM-AAPEAm₁₁ with 100 μ M 5-DSA recorded in darkness and at different temperatures. Each simulated spectrum is a combination of two spin systems; one fast rotating nitroxide radical and one slower rotating nitroxide radical, which is considered to be polymer-bound. The simulation parameters are listed in Tab. 10.13.

Table 10.13: *Easyspin* simulation parameters of the simulated systems shown in Fig. 10.102. The 'free' and 'bound' simulations at one temperature are combined to yield the final simulated spectrum.

$T/^{\circ}\text{C}$	component	proportion/%	g_{iso}	A_{iso}	τ_c/ns
15	Free	13.1484	2.00451	44.0784	0.156537
15	Bound	86.8516	2.00446	43.023	4.10685
20	Free	12.0082	2.00455	44.1149	0.131469
20	Bound	87.9918	2.00453	42.9872	4.21926
25	Free	11.5595	2.00456	44.099	0.186585
25	Bound	88.4405	2.00456	42.9181	4.1647
30	Free	11.2776	2.00458	44.0878	0.124203
30	Bound	88.7224	2.00467	42.2651	4.1508
35	Free	11.4817	2.00457	44.0748	0.104185
35	Bound	88.5183	2.00466	42.3629	4.23009
40	Free	11.9024	2.00457	44.0785	0.113537
40	Bound	88.0976	2.00465	42.3186	4.25283
45	Free	12.8636	2.00457	44.0801	0.0836612
45	Bound	87.1364	2.00468	42.3298	4.00423
50	Free	14.8763	2.00456	44.0686	0.0662425
50	Bound	85.1237	2.00471	42.1303	4.33646
55	Free	17.634	2.0046	44.0466	0.0663859
55	Bound	82.366	2.00475	42.0563	4.18928
60	Free	20.1212	2.00459	44.0014	0.0746922
60	Bound	79.8788	2.00471	42.1646	3.31089
65	Free	23.8625	2.0046	44.0281	0.0664012
65	Bound	76.1375	2.00474	42.0081	2.07845
70	Free	30.9378	2.0046	44.0281	0.0664012
70	Bound	69.0622	2.00474	42.0081	2.07845
75	Free	40.9214	2.00462	44.0216	0.0437268
75	Bound	59.0786	2.00479	41.9126	1.69687

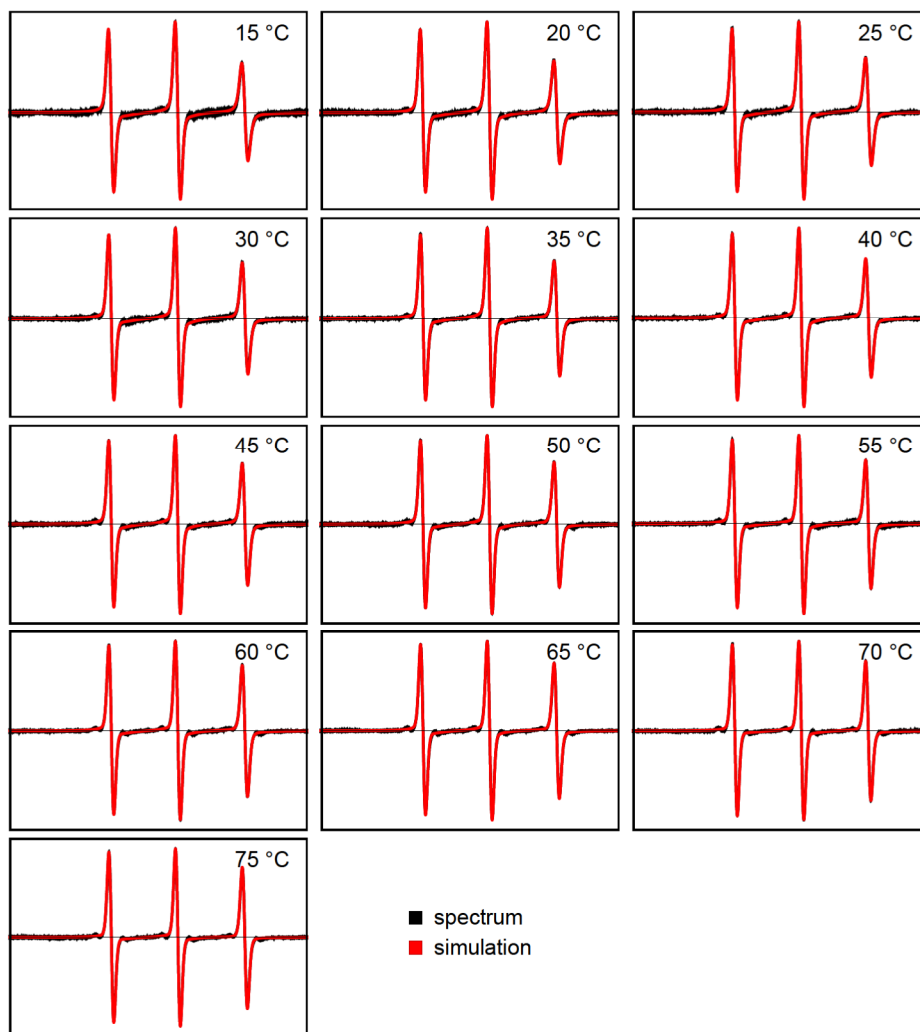


Figure 10.103: EPR spectra (black) and the *easyspin* EPR spectrum simulations (red) of 10 mg/ml DMAM-AAPEAm_{9.5} with 100 μ M 5-DSA recorded during UV irradiation (365 nm) and at different temperatures. Each simulated spectrum is a combination of two spin systems; one fast rotating nitroxide radical and one slower rotating nitroxide radical, which is considered to be polymer-bound. The simulation parameters are listed in Tab. 10.14.

Table 10.14: *Easyspin* simulation parameters of the simulated systems shown in Fig. 10.103. The 'free' and 'bound' simulations at one temperature are combined to yield the final simulated spectrum.

$T/^{\circ}\text{C}$	component	proportion/%	g_{iso}	A_{iso}	τ_c/ns
15	Free	51.1175	2.00455	44.0984	0.159535
15	Bound	48.8825	2.00431	40.0808	2.21571
20	Free	49.9153	2.00456	44.0821	0.221884
20	Bound	50.0847	2.00422	41.6963	1.49076
25	Free	47.5166	2.00456	44.0898	0.128171
25	Bound	52.4834	2.00448	40.6572	1.77025
30	Free	47.8786	2.00457	44.1093	0.128571
30	Bound	52.1214	2.00441	40.8483	2.09631
35	Free	52.4212	2.00455	44.129	0.0893388
35	Bound	47.5788	2.00427	42.4753	1.7223
40	Free	47.7379	2.00458	44.0696	0.0810454
40	Bound	52.2621	2.00453	40.8706	1.64335
45	Free	49.5133	2.0046	44.067	0.0914184
45	Bound	50.4867	2.00457	41.2723	1.44139
50	Free	49.8799	2.00461	44.0758	0.102164
50	Bound	50.1201	2.00451	40.8269	1.5597
55	Free	51.1409	2.00462	44.0516	0.0801678
55	Bound	48.8591	2.0047	39.7574	1.93624
60	Free	52.0103	2.00461	44.056	0.0598504
60	Bound	47.9897	2.00456	40.7703	1.12429
65	Free	54.1863	2.00463	44.0456	0.0584707
65	Bound	45.8137	2.00476	39.7079	1.67356
70	Free	52.7363	2.00461	44.0111	0.0558439
70	Bound	47.2637	2.00453	40.5271	1.28323
75	Free	61.2468	2.00463	44.0201	0.0450868
75	Bound	38.7532	2.00449	41.6826	1.97326

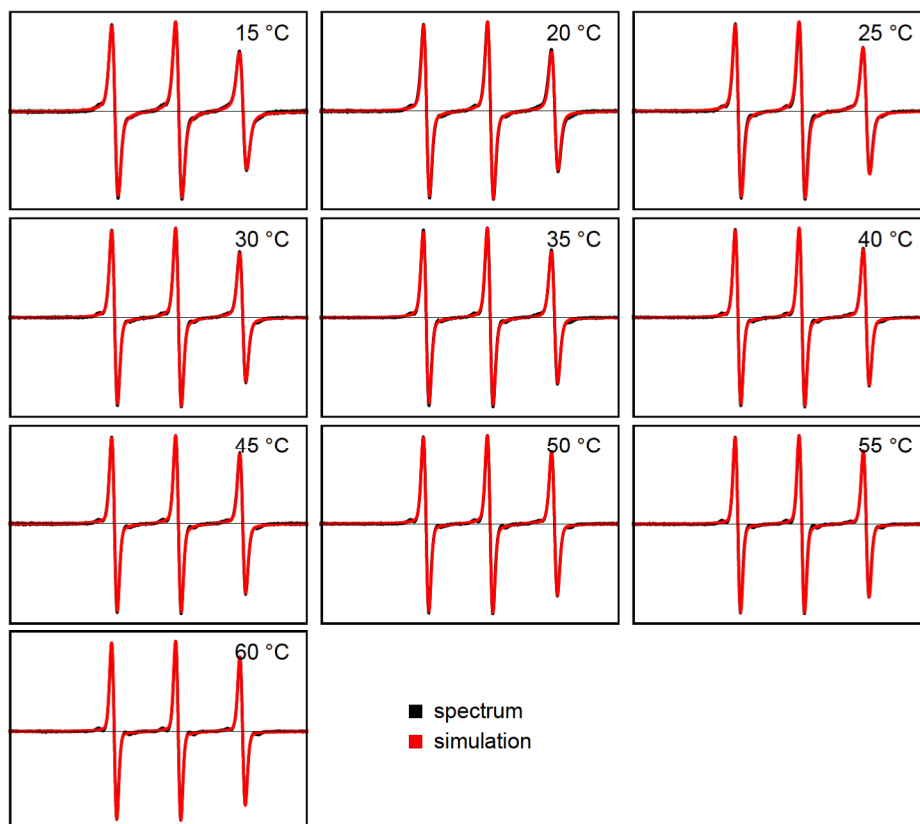


Figure 10.104: EPR spectra (black) and the *easyspin* EPR spectrum simulations (red) of 10 mg/ml AAPEAm with 100 μ M 5-DSA in 50 vol% MeOH recorded in darkness and at different temperatures. Each simulated spectrum is a combination of two spin systems; one fast rotating nitroxide radical and one slower rotating nitroxide radical, which is considered to be polymer-bound. The simulation parameters are listed in Tab. 10.15.

Table 10.15: *Easyspin* simulation parameters of the simulated systems shown in Fig. 10.104. The 'free' and 'bound' simulations at one temperature are combined to yield the final simulated spectrum.

$T/^{\circ}\text{C}$	component	proportion/%	g_{iso}	A_{iso}	τ_c/ns
15	Free	51.8877	2.00463	42.1881	0.141631
15	Bound	48.1123	2.0045	41.0226	1.1617
20	Free	56.6679	2.00461	42.1939	0.148617
20	Bound	43.3321	2.00457	40.7027	1.33835
25	Free	55.2702	2.00462	42.2488	0.10462
25	Bound	44.7298	2.00453	41.0739	1.14858
30	Free	53.4528	2.00463	42.2692	0.0908046
30	Bound	46.5472	2.00457	40.4259	1.30987
35	Free	60.9851	2.00463	42.291	0.121685
35	Bound	39.0149	2.00422	41.7109	1.92278
40	Free	56.0121	2.00461	42.3067	0.0793115
40	Bound	43.9879	2.00451	40.6113	1.4576
45	Free	55.4659	2.00463	42.28	0.0559077
45	Bound	44.5341	2.00444	41.0888	1.13009
50	Free	57.0241	2.00463	42.2796	0.076346
50	Bound	42.9759	2.00443	40.4709	1.23618
55	Free	61.9598	2.00463	42.2975	0.0654534
55	Bound	38.0402	2.00433	41.1808	1.54466
60	Free	61.2667	2.00465	42.3089	0.0575325
60	Bound	38.7333	2.0044	39.2382	1.42922

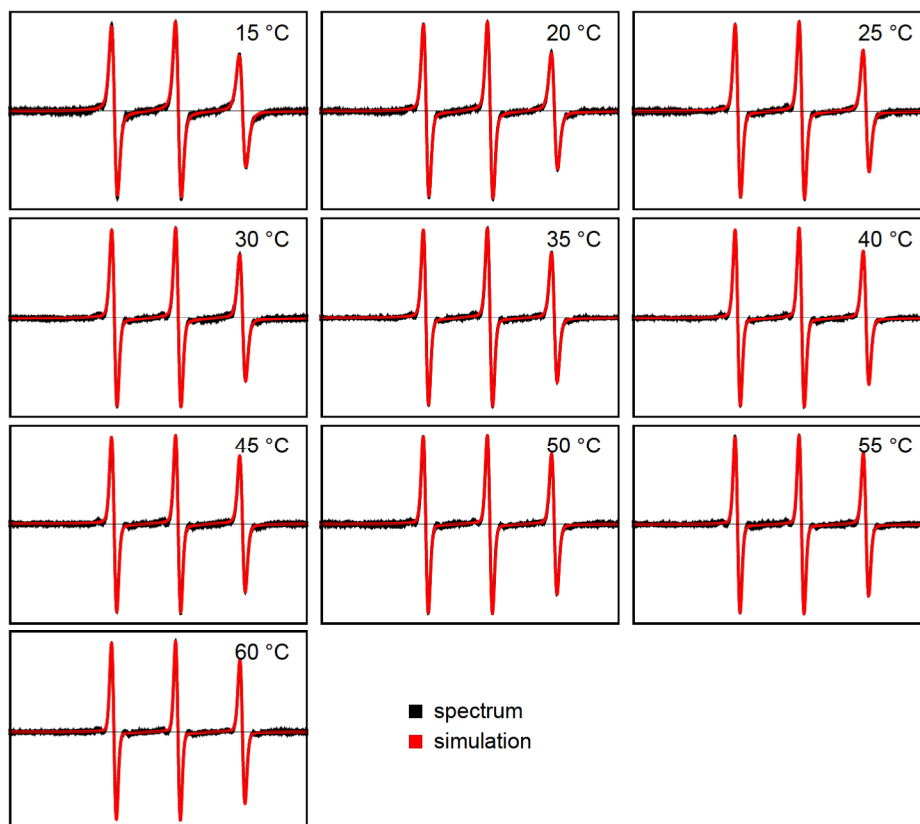


Figure 10.105: EPR spectra (black) and the *easyspin* EPR spectrum simulations (red) of 10 mg/ml AAPEAm with 100 μ M 5-DSA in 50 vol% MeOH recorded during UV irradiation (365 nm) and at different temperatures. Each simulated spectrum is a combination of two spin systems; one fast rotating nitroxide radical and one slower rotating nitroxide radical, which is considered to be polymer-bound. The simulation parameters are listed in Tab. 10.16.

Table 10.16: *Easyspin* simulation parameters of the simulated systems shown in Fig. 10.105. The 'free' and 'bound' simulations at one temperature are combined to yield the final simulated spectrum.

$T/^{\circ}\text{C}$	component	proportion/%	g_{iso}	A_{iso}	τ_c/ns
15	Free	65.5316	2.00468	42.2073	0.190295
15	Bound	34.4684	2.00395	43.9782	2.81894
20	Free	56.9858	2.00466	42.2704	0.0965363
20	Bound	43.0142	2.00454	39.046	1.57991
25	Free	56.7125	2.00468	42.2643	0.0979025
25	Bound	43.2875	2.00453	39.2635	1.55883
30	Free	56.9937	2.00468	42.2902	0.118168
30	Bound	43.0063	2.00438	39.0651	1.66005
35	Free	59.7212	2.00469	42.2912	0.100556
35	Bound	40.2788	2.00436	38.3791	2.04804
40	Free	61.7354	2.00469	42.263	0.0999304
40	Bound	38.2646	2.00433	39.2337	1.5573
45	Free	63.3341	2.00469	42.2981	0.0742275
45	Bound	36.6659	2.00424	39.9594	1.49107
50	Free	64.2815	2.0047	42.3443	0.0560851
50	Bound	35.7185	2.00442	39.0093	1.68526
55	Free	68.5922	2.00471	42.3805	0.0757281
55	Bound	31.4078	2.00418	41.0533	1.61706
60	Free	69.5787	2.00472	42.3486	0.0676532
60	Bound	30.4213	2.00387	40.9942	2.06659

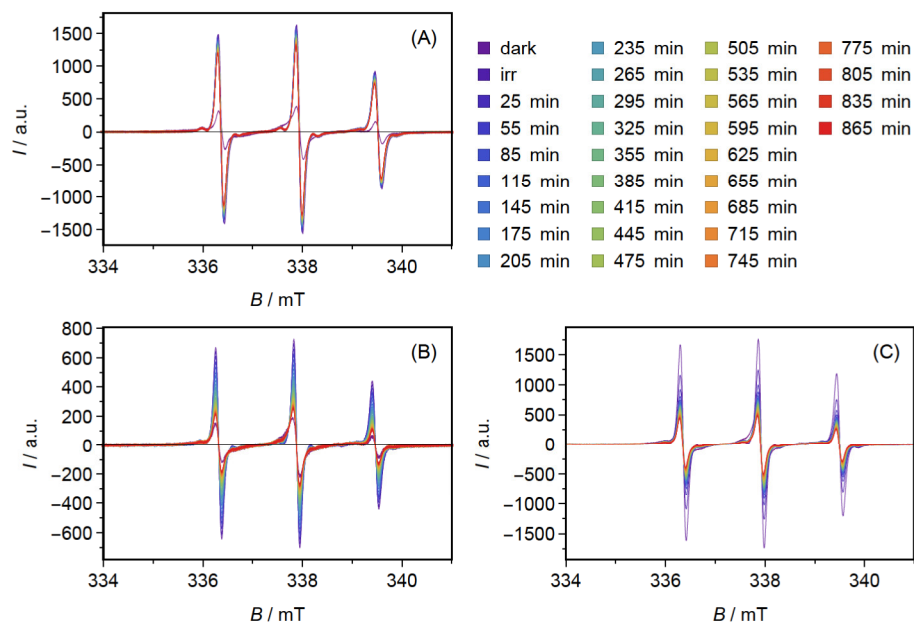


Figure 10.106: EPR spectra of 1 mg/ml DMAM-AAPEAm₇ with 100 μ M 5-DSA at 25 °C (A), 45 °C (B) and 65 °C (C). The first and broadest EPR spectrum was recorded in the dark. Afterwards, the sample was irradiated (365 nm) during the acquisition of the second spectrum 'irr'. To monitor possible *cis-trans*-relaxation, spectra were collected during 865 min of darkness after irradiation (see legend). The normalized EPR spectra are shown in Fig. 7.13.

11 Acknowledgements

First and foremost, praises and thanks to Prof. Dr. Dariusz Hinderberger for giving me the opportunity to research and work in his laboratories. His knowledge, vision and highly respectful treatment of fellow students and colleagues have deeply inspired me.

I want to express my profound and sincere gratitude to my research colleagues, members and fellow labmates of the Hinderberger group and the BEAM GRK for stimulating discussions, delicious cakes and barbecues.

Lastly, I am extremely grateful to my family and my wife Jenny for their love, understanding and continuing support to complete this research work. They were behind me throughout all of my academic career.

11 Acknowledgements

12 Scientific Contributions

E. Hipper, **F. Lehmann**, W. Kaiser, G. Hübner, J. Buske, M. Blech, D. Hinderberger and P. Garidel (2022): Protein photodegradation in the visible range? Insights into protein photooxidation with respect to protein concentration. *International Journal of Pharmaceutics: X*, 100155.

Y. Cai, **F. Lehmann**, E. Peiter, S. Chen, J. Zhu, D. Hinderberger and W. H. Binder (2022): Bergman Cyclization of Main Chain Enediyne Polymers for Enhanced DNA Cleavage. *Polymer Chemistry*, 13, 3412–3421.

The following manuscripts are in preparation (data available on request):

E. Hipper, T. Diederichs, W. Kaiser, **F. Lehmann**, J. Buske, D. Hinderberger and P. Garidel (2024): Visible Light triggers the Formation of Reactive Oxygen Species in Polysorbate containing Formulations.

F. Lehmann, E. Hipper, P. Garidel and D. Hinderberger (2024): The ongoing search for protein-bound photosensitizers in monoclonal antibody solutions causing photodegradation under visible light.

R. Steinbrecher, **F. Lehmann**, P. Zhang, C. M. Papadakis, P. Müller-Buschbaum, A. Taubert, H. Möller, M. L. Kellner, D. Hinderberger and A. Laschewsky (2024): Fully Photo-responsive Amphiphilic Polymers via Azo Dye Functionalization of Polyacrylamides.

Y. Cai, **F. Lehmann**, D. Hinderberger and W. H. Binder (2024): Initiator-free synthesis of interpenetrating polymer networks via Bergman Cyclization.

The following publications are not included in this thesis:

M. Alqaisi, J. F. Thümmeler, **F. Lehmann**, F.-J. Schmitt, L. Lentz, F. Rieder, D. Hinderberger and W. H. Binder (2024): Tuning the nanoparticles internal structure: fluorinated single-chain nanoparticles (SCNPs) generated by chain collapse of random copolymers. *Polymer Chemistry* (submitted).

Z. Durmus, R. Köferstein, T. Lindenberg, **F. Lehmann**, D. Hinderberger and A. W. Maijenburg (2023): Preparation and characterization of Ce-MOF/g-C₃N₄ composites and evaluation of their photocatalytic performance. *Ceramics International*, 49, 24428–24441

N. Heise, **F. Lehmann**, R. Csuk, T. Mueller (2023): Targeted theranostics - near-infrared triterpenoic acid-rhodamine conjugates as prerequisites for precise cancer diagnosis and therapy. *European journal of medicinal chemistry*, Elsevier Science, Bd. 259

R. Naumann, **F. Lehmann**, M. Goetz (2018): Micellized Tris(bipyridine)ruthenium Catalysts Affording Preparative Amounts of Hydrated Electrons with a Green Light-Emitting Diode. *Chemistry*, 6;24(50):13259-13269.

R. Naumann, **F. Lehmann**, M. Goetz (2018): Generating Hydrated Electrons for Chemical Syntheses by Using a Green Light-Emitting Diode (LED). *Angewandte Chemie International Edition*, 57(4), 1078-1081.

Halle (Saale), May 6, 2024

13 Curriculum Vitae

Personal Data

Name Florian Lehmann

Academic Career

2020-2024	Promotion, AG Prof. D. Hinderberger, Martin-Luther-Universität Halle-Wittenberg
2017-2019	Master of Science, Martin-Luther-Universität Halle-Wittenberg
2014-2017	Bachelor of Science, Martin-Luther-Universität Halle-Wittenberg
2006-2014	Allgemeine Hochschulreife, Ludwigsgymnasium Köthen
2003-2006	Grundschule Edderitz

14 Declaration of Authorship

I hereby declare that I am the sole author of this PhD-thesis and that I have not used any sources other than those listed in the bibliography and identified as references. I further declare that I have not submitted this thesis to any other institution in order to obtain a degree.

.....

Florian Lehmann

Halle (Saale), May 6, 2024